Stony Brook University

Assembly, Structure and Properties of DNA Programmable Nanoclusters

A Dissertation Presented

by

Cheng Chi

to

The Graduate School

in Partial Fulfillment of the

Requirements

for the Degree of

Doctor of Philosophy

in

Chemistry

Stony Brook University

May 2014

Stony Brook University

The Graduate School

Cheng Chi

We, the dissertation committee for the above candidate for the
Doctor of Philosophy degree, hereby recommend
acceptance of this dissertation.

Oleg Gang
Dissertation Advisor
Group Leader of Soft and Bio Nanomaterials, Center for Functional Nanomaterials, Brookhaven National Lab

R.B.(Barney) Grubbs
Professor
Chemistry Department, Stony Brook University

Peter Khalifah
Professor
Chemistry Department, Stony Brook University

George John
Professor
Chemistry Department, City College of New York-CUNY

This dissertation is accepted by the Graduate School

Charles Taber
Dean of the Graduate School

Abstract of the Dissertation

Assembly, Structure and Properties of DNA Programmed Nanoclusters

by

Cheng Chi

Doctor of Philosophy

in

Chemistry

Stony Brook University

2014

Finite size nanoclusters can be viewed as a nanoscale analogue of molecules. Just as molecules, synthesized from atoms, give access to new properties, clusters composed of nanoparticles modulate of their functional properties of nanoparticles. In contrast to synthetic chemistry which is a mature field, the creation of nanoscale clusters with well-defined architectures is a new and challenging area of research. My work explores how to assemble model systems of nanoclusters using DNA-programmable interparticle linkages. The simplest clusters of two particles, dimers, allow one to investigate fundamental effects in these systems. Such clusters serve as a versatile platform to understand DNA-mediated interactions, especially in the non-trivial regime where the nanoparticle and DNA chains are comparable in size. I systematically studied a few fundamental questions as follows:

Firstly, we examined the structure of nanoparticle dimers in detail by a combination of X-ray scattering experiments and molecular simulations. We found that, for a given DNA length, the interparticle separation within the dimer is controlled primarily by the number of linking DNA. We summarized our findings in a simple model that captures the interplay of the number of DNA bridges, their length, the particle's curvature and the excluded volume effects. We demonstrated the applicability of the model to our results, without any free parameters. As a consequence, the increase of dimer separation with increasing temperature can be understood as a result of changing the number of connecting DNA.

Later, we investigated the self-assembly process of DNA-functionalized particles in the presence of various lengths of the DNA linkage strands using 3 different pathways. We observed a high

yield of dimer formation when significantly long linkers were applied. Small Angle X-ray Scattering revealed two configurations of the small clusters by different pathways. In one case, the interparticle distance increases as the function of linker length. In the other case, the interparticle distance of the cluster decreases with the linker length until the DNA shell thickness of the particles. This result suggests a configuration in which nanoparticles are confined due to the hybridization of flexible linkers from opposite particles' hemispheres. The effect is accompanied by inhibited growth of nanoclusters, resulting in a self-limited cluster assembly.

Secondly, we investigated several types of system including spherical particles and simplest asymmetric structures, Janus particles and dimers interacting with DNA functionalized surface, in which the single stranded DNAs immobilized on surfaces are complementary to DNA grafted on one of cluster particles or on a side of Janus particle, We observed an interesting surface binding behavior: kinetics of surface recognition strongly depends on the design of nanoclusters, the surface oligonucleotide density and a salt concentration. Based on these studies, a new method was developed for a separation of single particles and nanoclusters. Dimers were also applied as basic units to build hierarchical structures.

Thirdly, dimers were applied as a sensor for single-stranded DNA detection. The detection is based on dimer disassembly triggered by binding of target nucleic acid strands. Target detection and disassembly kinetics were followed in real time using dynamic light scattering. The observed disassembly process is in agreement with a two-step kinetic model. The DNA sensing was found to be selective down to the level of a single base mismatch, even in the presence of a high concentration of interference DNA. The method further provides label-free detection of DNA in minutes, and demonstrates the use of this new class of nanoclusters as a powerful platform for nucleic acid sensing.

Lastly, we explored the diffusion properties of nanoclusters in polymer solution. Classical diffusion theory well explains a large number of transport phenomena for molecular, nano and micro-scale systems in simple liquids. However, the question about the diffusion of nano-constructs in complex liquids, particularly when the size of those constructs is comparable to the structural units (polymers) existed in liquid is not well explored. As a model system, the diffusion of dimers of 10nm gold nanoparticles covered with symmetric and asymmetric shells in

various concentrations of polyethylene glycol (PEG) solutions was studied by particle tracking method and dynamic light scattering. In the experimental time regime, both dimers with symmetric and asymmetric soft-matter shell exhibit a typical Brownian motion. However, we observed a significant enhancement of diffusion for asymmetric structures compared to the symmetric ones. We systematically studied the effect of cluster structure, solution viscosity and composition on the discovered phenomenon.

For My Family.

Table of Contents

List of Figures

ZS instrument analysis software (b) Dependence of D_h on $\boldsymbol{L}$ at room temperature; the error bars are estimated from multiple measurements.

Figure 2.5. Simulation protocol for dimer formation of two DNA-coated NPs connected by four linkers. (a) Two DNA-coated NPs and four linkers (pink strands) are located at random positions. (b) Four strands of one hemisphere of each NP are randomly selected. (c) Hybridization occurs between the linkers and strands of the left NP. (d) Hybridization with second NP followed by equilibration.

Figure 2.6. Left panel (a and b). Representative 2D small-angle x-ray scattering patterns of dimers for L=0 (a) and L=75 (b). (c) Relative SAXS intensity, $I(q)$, of dimer systems, as labeled in the inset. (d) The structure factors $S(q)$, obtained as discussed in the method, for systems with corresponding colors shown in (c)**.**

Figure 2.7. Surface-to-surface distance $\boldsymbol{r}$ as a function of linker length $\boldsymbol{L}$. Red, blue and black respectively correspond to dimers linked by dsDNA, dimers linked by ssDNA, and crystals linked by ssDNA. The symbols are data from the SAXS experiments. For dsDNA linked dimers, there is a linear relation between $\boldsymbol{r}$ and $\boldsymbol{L}$. For the ssDNA linked systems, the curves are from fits to the worm-chain model (Eq. 2), which yields for the crystal $\boldsymbol{l_p}$=2.1 nm, and for the dimer $\boldsymbol{l_p}$=0.33nm.

Figure 2.8. The computed distribution of the surface-to-surface distance $\boldsymbol{r}$ for a dimer linked by either one or four chains for linker length $\boldsymbol{L}$ = 10 bases. The NP-NP separation is smaller when more than one linker connects the dimer. The insets show representative dimer configurations at corresponding linker numbers.

Figure 2.9. Comparison of the computed end-to-end distance of free ssDNA (blue) with the ssDNA connecting the dimer via one linker (black) or four linkers (red). The curves are fits to the worm-chain model (eq. 2), which show that the effective persistence length relative to a free chain is larger for NP connected by one linker and smaller for NP connected by four linkers.

Figure 2.10. (a) The surface-to-surface separation $\boldsymbol{r}$ as a function of $\boldsymbol{L}$ for the dimer connected via one linker (black) or four linkers (red). The symbols represent the simulation data and the curves the theoretical model proposed in Eq (5). (b) The dependence of $\boldsymbol{r}$ on $\boldsymbol{L}$ from experiments at room temperature (26^{O}C) and before melting (35^{O}C); solid curves represent the function of $\boldsymbol{r}$ over $\boldsymbol{L}$ estimated from the analytical model with 1 (blue) and 4 (red) linkers in a dimer.

Figure 2.11. (a) Design of two studied systems: (system 1) dimers fabricated using a single stranded linker, and (system II) dimers fabricated using a combined linker. (b) Surface-to-surface distance $\boldsymbol{r}$ as a function of linker length $\boldsymbol{L}$. For the system II, $\boldsymbol{L}$=$\boldsymbol{M}$+$\boldsymbol{N}$**.** Red curves represent the function of $\boldsymbol{r}$ over $\boldsymbol{L}$ for corresponding systems estimated from theoretical model at n=4, $\boldsymbol{l_p}$=2.2nm.

Figure 2.12. The change of the DLS measured hydrodynamic diameter (D_h) before (T=26 ^{o}C) and after a DNA melting (T=40^{o}C) indicate a dimer disassembly for experimental systems.

Figure 2.13. Temperature dependent D_h for corresponding linkers as shown; the data were obtained from DLS measurements. The number-averaged size of clusters depends on change of: a population of dimers (decreases during melting of dimers) and interparticle distances (increase with temperature). Overall, the first factor plays a more significant role in D_h change with temperature.

Figure 5.2. DLS based measurements of dimer disassembly. a) DLS based time-dependent dimer dissociation profiles for 2 nM of dimer at target concentrations 5 nM, 20 nM and 105 nM. b) The measured dependence of τ on target concentrations (points). The fit using the shown kinetic model for the disassembly (line) yields $K=1.38\times10^4$ $M^{-1}s^{-1}$. Measurements were performed in triplicate for each target concentration.

Figure 5.3. Investigation of the effect of mismatch position and number. a) DLS measurements display dimer dissociation in the presence of perfect matched strand, mismatched targets: T-1mid and T-3mid and b) the comparison of kinetic rate constant K for different mismatched targets list in Table 1 obtained from fitting curves. The inset graph shows corresponding τ values.

Figure 5.4. Dimer disassembly in the presence of interfering ssDNA a) τ values from interference experiments at different ratios between interference T-3mid strands and perfect matched strand as indicated at the constant target concentration (20 nM) ; b) the dependence of measured (points) τ on the same total concentration of target and T-3mid strands (50 nM) with different concentration of target, Fit (line) yields $K=1.48\times10^4$ $M^{-1}s^{-1}$, the result is consistent with the magnitude of K obtained without T-3mid mismatched single-stranded DNA.

Figure 5.5. DLS-measured number averaged hydrodynamic radius of Au nanoparticles (green), and Au-QD Janus cluster before (black) and after (red) adding DNA_T.

Figure 5.6. Schematic design of experiments for the disassembly of Au~QD Janus clusters.

Figure 5.7. Measured PL intensity and lifetime of Au~QD Janus cluster disassembly (a) and proposed disassembly mechanism (b).

Figure 6.1. Schematic illustration of the studied systems: a) control dimer b) dimer with DNA tails grafted on one of the particles and c) dimer with DNA tails grafted on both particles. d) These three structures were dispersed in the various polymer solutions respectively, and their diffusion behavior was observed by particle-tracking and DLS.

Figure 6.2. A) Photos of the instrument used in this study. B) A snapshot of 50 nm gold nanoparticle movement captured by microscope. C) Trajectories of each particle extracted by Nanoparticle Tracking software. D, E) Mean square displacement (MSD)~τ curve based on Displacement probity distributions obtained by analyzing all of the trajectories shown in image C.

Figure 6.3. Characterization of the typical diffusion in 9% mass percentage of PEG 35,000 : a)Two-dimensional projection of typical 12 s trajectories (with 0.03s between frames) of asymmetric (shown in blue) and symmetric dimer control sample a (shown in red). b) Linear plots of the mean squared displacement (MSD) as a function of τ for both asymmetric (blue) and symmetric (red) dimers, calculated from more than 500 non-overlapping trajectories. c) Displacement probability distribution with time interval τ =0.6s. d) Logarithmic plot of MSD of three different studied systems as shown below. The black dashed curve is the reference line, estimated by Brownian motion using the macro-viscosity of the solution obtained from viscosity measurements.

Figure 6.4. MSD as a function of τ in various PEG 35K concentrations with the mass percentage equals to 3% (a) 7.5% (b) and 12%(c), the macro-viscosity of which changed to up 30 folds and (d) their diffusion enhancement factor as a function of PEG mass percentage.

List of Tables

Acknowledgments

I would like to begin by thanking my PhD advisor, Dr. Oleg Gang, for his consistent support, mentoring and help during my years in graduate school. His profound knowledge, positive attitude and unbelievable passion for science always keep me highly motivated!

I am grateful to Professor Robert Grubbs, Professor Peter Khalifah and Professor George John for kindly serving as my committee members and for their helpful comments. I would also express my deep acknowledgements to Professor Stanislaus S. Wong, and Professor Benjamin Chu for their helpful suggestions in my first, second and third meetings.

I would like to thank Professor Mathew Maye for helping me get started in the group. I would like to thank all of my group members and colleagues in the Center for Functional Nanomaterials: Dr. Dmytro Nykypanchuk, Dr. Andrea Stadler, Dr. Yugang Zhang, Dr. Fang Lu, Dr. Dazhi Sun, Dr. Miho Tagawa, Dr. Mircea Cotlet, Dr. Kevin Yager, Dr. William Sherman, Dr. Kumara Mudalidge, Tian Ye, Wenxuan Lian and Kelly Neer. All of them have unconditionally given me scientific support and make my research life in CFN very enjoyable! I also want to thank my collaborators throughout this work: Professor Francis W. Starr, Fernando Vargas Lara, Dr. Jonathan Halverson and Dr. Alexei Tkachenko.

I am lucky to be surrounded by a great group of people in BNL and Stony Brook University, who make my life here joyful. Those friends including: Jing Tao, Yan Li, Zhongwei Liu, Liu Li, Ping Cao, Yixiong Yang , Jing Zhou, Lei Huang ,Yin Liu, Yan Zhang, Ran Wang, Ziqi Gao, Pollard Shawn. Diane Zhong, Chloe Wang, Wei-fu Chen.

I would like to dedicate this work to my loving family: my grandparents, my parents, my parents- in-law, my husband and our adorable daughter, YiYi.

Chapter 1

Introduction

1.1 Basics of Self-assembly

One of the most significant and challenging questions in nano-science is how to build complex nanoscale systems which incorporate nano-objects from various shapes, materials, sizes and functionalities.[1] Optimal alignment of nano-objects with novel physical properties such as metallic, semiconductor and magnetic nanoparticles in designed structures is particularly important for diverse applications, such as nanophotonics[2] and nanomedicine. [3, 4] Lithographic approaches are often limited as their ability to grind nanostructure with wet chemistry methods. In this respect, self-assembly is a promising platform to address this challenge to create new nanomaterials. However the approaches for fabrication of such a designed self-assembled system are not well-developed yet.

In nature, atoms and molecules bind with each other by chemical bonds. The directionality of the bonding is determined by their electronic structure. Unlike atoms and molecules, the packing of the nano-object is more likely to be constrained by the geometry of the building block. [5] In order to achieve a programmable binding, the soft matter component, such as polymers, surfactant and biomolecules were applied for functionalize the hard core of the nano-objects. Soft matter serves as the interaction medium offering the flexible spacer and strong binding force between nano-objects. Biological interactions, such as protein-protein recognition and DNA hybridization, provide a convenient and powerful way to program the binding on the nano-

scale.[6] The interaction between nano-objects can be precilsely programmed through interplaying of the specific biological binding and nonspecific physical interaction.

In the past decades, computational studies reveals a broad possibility of creating diverse structures, from finite-sized nanoclusters to 3D super-lattice using soft-matter functionalized nanoparticles. In most cases, the equilibrium state is difficult achieved due to the kinetic barrier related to the metastable states.

1.1.1 Geometry-driven Self-assembly

One of the most straightforward cases of self-assembly one can imagine is to build a structure simply by packing the building blocks of different shapes. In this case, colloidal particles interact through the excluded volume arising from their shape. The thermodynamic behavior of hard (nonoverlapping) particles can be understood through entropy maximization packing efficiency. Dense packings have been employed to model the structure of low-temperature systems, including glasses, crystals, heterogeneous materials, and granular media.[7] A few simulations suggested that the entropy alone was responsible for stabilizing the assemblies formed from various types of building blocks. For example, the simulation results from two dissimilar hard spherical species revealed the complex phase diagram of their assembled structure.[8] For the case of polyhedrals, packing efficiently is usually determined by contact area. Therefore, an effective many-body directional entropic force arises from the increased number of configurations available to the entire system, which causes suitably faceted polyhedral to form order.

Figure 1.1 shows an example of self-assembled polyhedral structures from the computational study. [9] Predication by calculations, Pablo F. Damasceno et al reveal a remarkably interesting

propensity for thermodynamic self-assembly and structural diversity. They reveal the following trends for geometry-driven self-assembly of a polyhedral: 1) Highly spherical polyhedral have no-directional or weakly directional entropic interactions, which leads to FCC (HCP) and BCC crystals. 2) Polyhedrals that form plastic crystals are more aspherical, with fewer faces that are more pronounced, while the polyhedrals assembling into crystals usually have strong directional entropic bonding, much like covalent bonds. 3) Polyhedrals forming liquid crystals typically have an axial shape. It is important to align the most prominent face and long particle dimensions first.

Figure 1.1. Calculated phase diagram of a close-packing structure obtained from corresponding polyhedral. Reprinted with permission from reference 7. Copyright 2012, Science. the American Association For the Advancement of Science.

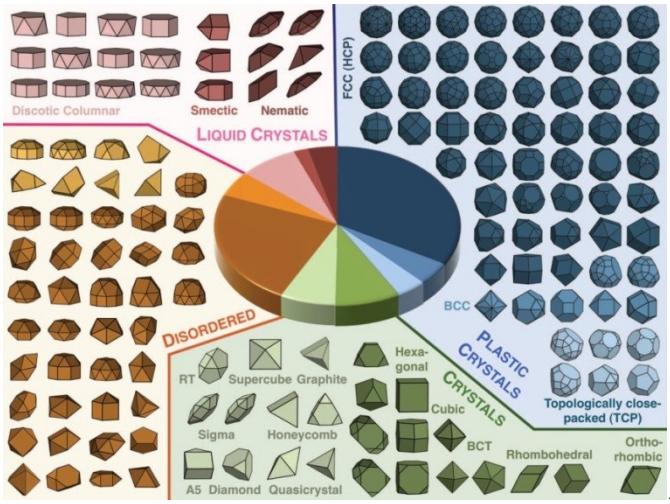

The entropy-driven packing of hard particles can be achieved experimentally. For example, a self-assembled binary nanocrystal superlattice (BNSL) can be obtained by evaporating the carrier solvent. Moreover, the BNSL membrane appears at the liquid-air interface.[10, 11] The co-crystallization of a multicomponent nanocrystal was ascribed to the densest packing of two

different sized spherical particles, although we note here that the crystalline superlattice are not necessary the densest packings of particles. To date, BNSLs that are isostructural with NaCl, NiAs, CuAu,AlB_2, $MgZn_2$, $MgNi_2$, Cu_3Au, Fe_4C,$CaCu_5$, CaB_6, $NaZn_{13}$, and cubic AB_{13} compounds, have been assembled from nanoparticles of different sizes.[11, 12] The observed structural diversity is rather challenging to be understood theoretically. If nanocrystals were simple hard spheres, most of these structures would be unstable relative. The formations of multiple low symmetry BNSLs suggests that nanocrystals interact with each other in a rather complex manner. For example, colloidal nanocrystals can have electric charges, dipole moments, and polarizabilities, and exhibit strong van der Waals and ligand-ligand interactions. Therefore, the next logical step is to consider the interparticle potential of these particles.[12]

1.1.2 Interaction between Particles

In order to quantitatively understand the interaction between particles, we use "pair potential" to describe the pair force acting between atoms and colloids. In the simplest model system, a simple fluid of non-polar atoms or molecules, the pair potentials can be presented by Lennard–Jones 12-6 potential: [13, 14]

$$u(r) = 4\epsilon \left[\left(\frac{\sigma}{r}\right)^{12} - \left(\frac{\sigma}{r}\right)^{6}\right] \quad for\ r > 0 \qquad \textbf{(1.1)}$$

in which the first is the repulsive term described by Pauli repulsion at short range due to overlapping electron orbitals. The r^{-6} term, which is the attractive long-range term, describes attraction at long ranges (van der Waals force, or dispersion force). In this model, two parameters characterize the potential: the collision diameter, where u(r) =0, and the depth of Ɛ which is the energy mimina of the system. The simple Lennard–Jones potential is a good approximation to

describe gases. However, because this model fails to describe the many-body effects and their corresponding bond directionalities, it cannot capture the properties of a more complicated system such as molecules with more than two atoms or a cluster with more than two colloids.

Therefore, when dealing with colloidal systems, a more accurate approximation needs to be taken into account: the pair potential between two colloids can be quantitatively estimated based on the specific forces placed on these particles. For example, the electrostatic repulsion between two colloidal particles can be estimated by the effective number of charges on the colloidal surface. The van der Waals force can be computed based on "microscopic theory," which takes into account the size and geometry of colloidal particles. A well-studied example of charge-stabilized colloidal dispersions is polystyrene latex spheres dispersed in a polar solvent such as water. The latex particles acquire a high surface charge through the dissociation of ionizable surface groups. Each colloidal particle is surrounded by a diffuse layer of oppositely charged counterions, which are monovalent in the simplest case. Overlap of the electric layers of two colloidal macroions leads to an electrostatic repulsion which counteracts the van der Waals attraction and prevents the aggregation of the particles. [15]

In principle, the distance between pairs of particles can be calculated by the interaction force. Moreover, it can be measured indirectly from static scattering experiments. Therefore, the distribution of distances between pairs of particles is an important connection between theoretical estimation and experimental measurement.

In liquid state theory, pair distribution function (PDF), g(r), was used to describe the distribution of distances between pairs of particles contained within a given volume. The PDF can be derived from the reduced distribution function. Its physical meaning corresponds to the probability of finding the second particle with interparticle distance r.

This value is strongly related to the so-called potential of mean force, as represented as (r) , in the following way:

$g\ (r) =: e^{-\beta\omega(r)}$ **(1.2)**

in which $\beta = \frac{1}{kT}$.

The physical meaning of potential of mean force described the potential to hold 2 particles fixed with certain interparticle distance. Likewise, ω(r) can be interpreted as the reversible work for a process in which two particles are moved through the system from infinite separation to a relative separation r. It is important to point out that the function of ω(r) is generally more complicated than the pair potential u(r), since it involves the effects of particles 1 and 2 on the configuration of the other particles. Only in the limit of particle concentration tends to 0, w(r) →u(r).

1.2. DNA Nanotechnology

DNA is a nano-scale biomolecule which carries genetic information in biological system. DNA is also proposed by Seeman in 1982 as structural material in DNA driven assembly for nanotechnology. It a powerful route for organizing matter on a nanometer scale with the great accuracy and control.[16] A double stranded DNA is composed of two complementary anti-parallel single-stranded DNA strands, forming a right-handed double helix molecule. The diameter of DNA helix is about 2nm, and its helical pitch is about 3.4nm. The unique DNA hybridization based upon strand complementarity is programmable and predictable: the outstanding specificity of the A-T and G-C Watson-Crick hydrogen-bonding interaction allows the convenient programming of artificial DNA receptor moieties through the simple four-letter

alphabet. At the same time, its nonspecific interaction can be understood on a basis of polymer concepts.[17]

The DNA motif acts as building blocks to construct pre-designed DNA nanostructures with robust topological or geometrical features through specific structure interactions. In nature, DNA molecules usually retain a linear conformation. In order to achieve the artificial motif with a more complex and diverse structure, a few approaches has been applied.

1.2.1 Self-assembled DNA Objects

One approach to change the linear morphology of DNA is to create the branched DNA. The branched DNA was first demonstrated and constructed in 1983, which was an immobile four-arm junction containing four 16 mer DNA strands (shown as Figure 1.3). This synthetic DNA junction was stable in buffered condition, and could not undergo spontaneous branch migration due to the lack of homologous twofold sequence symmetry flanking the central branch point.

Another mode of DNA connection is called sticky end (Figure 1.2). The sticky ends are complementary single-stranded overhangs protruding from the ends of DNA duplexes, which provide a convenient and efficient cohesion tool for assembling small DNA nano-objects. The combination of branched DNA and sticky ends leads to a diverse range of possible structures, eventually overcoming the disadvantage of the linear properties of DNA. [17]

Figure 1.2. Schematic formation of 2D DNA crystal formed by branched DNA with for arms and sticky ends complementary. Reprinted with permission from Reference 18. Copyright 2003, Nature Publishing Group.

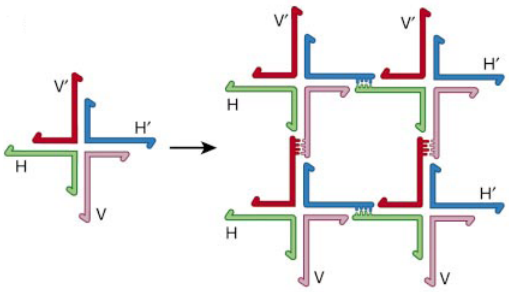

Recently, a variety of DNA motifs have been created using different methods. For example, Seeman and coworkers assembled the first 3D DNA nano-object, which is a DNA cube assembled via stepwise ligation.[18] The second polyhedral molecule is a truncated octahedron made through step-wise solid phase synthesis. [19] A DNA tetrahedron and a DNA bipyramid can be synthesized in a one-step annealing process;[20] Shih and his colleagues created a DNA octahedron by folding a 1.7 kb ssDNA with the help of five short DNA strands.[21] Numerous DNA nano-objects (cube, triangular prisms, pentameric prisms, biprisms, etc.) were fabricated using cyclic single-stranded DNA containing organic vertices as building blocks.[22] The hierarchical assembly of DNA tetrahedra, dodecahedra, and buckyballs from symmetric three-point-star motifs are also achieved by Mao's group in 2008.[23]

It is also worthy to emphasize that an assembly of DNA strands can process data in a similar way to an electronic computer, and such approach has the potential to solve far more complex problems and store a greater amount of information. The algorithm for DNA assembly can also be programmed by computers.[24]

1.2.2 Scaffolded DNA Origami

In 2006, a new approach for building DNA 2D patterns and shapes from DNA has been demonstrated by Rothermund, SOcalled "DNA origami"[25]. In this method, numerous short strands of single-stranded DNA were applied to direct the folding of a long single-stranded DNA, which can achieve the designed 2D pattern with a size of over 200nm and resolution down to 6nm (Figure 1.3a). For example, a long single-stranded M13mp18 genomic (M13) DNA is used as a scaffold molecule, and folded into nearly any desired shape with the help of more than 200 short complementary DNA staple strands in a single-step mixing and annealing (Figure 1.3b). This method opens up a lot of opportunity to create desired 2D nanoparticle patterns by positioning the nanoparticle in a desired location. Afterwards, a lot of efforts have been dedicated to encoding nanoparticles into the DNA origami, and, to generate designed 2D and 3D structures which contain intricate curved surfaces. [26]

Figure1.3. A schematic description of 2D DNA origami array formed by using small DNA tiles as folding staples (a), and DNA origami shapes designed and obtained from experiments (b). Reprinted with permission from Reference 22. Copyright 2006, Science, the American Association For the Advancement of Science.

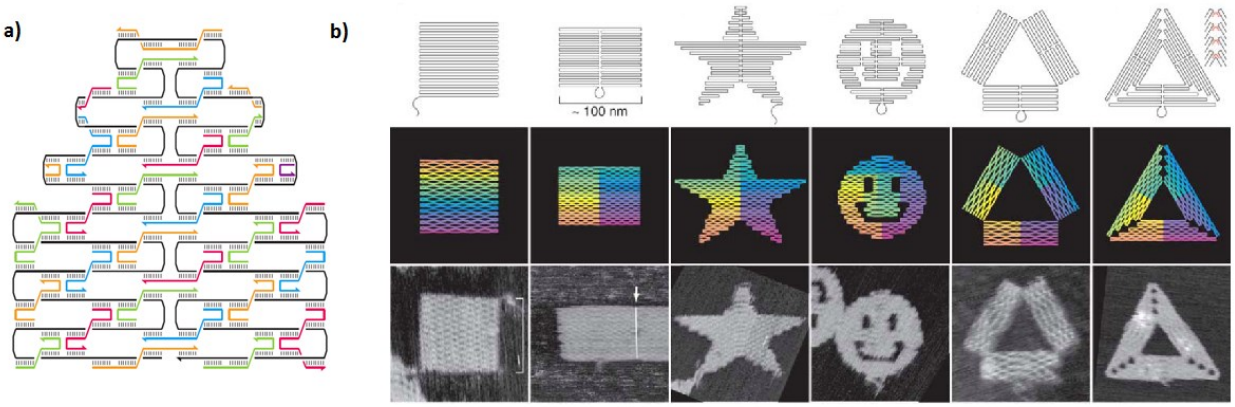

.

1.2.3 Dynamically Assembled Structures

DNA can be also used for the dynamic assemblies of nano-objects. “Dynamic assembly” means the DNA functionalized structure will experience some significant structural changes under certain conditions, and in most cases this structural change is reversible.[27] In general, there are two types of dynamic assembly processes: for the first type, the internal structure will switch reversibly from one state to the other depending on the environmental changes. The core idea of this type of dynamic assembly is that some distinct base paring can be switched by the addition of thermodynamically more favorable binding strand and conformation change. Such environmental changes include the variation of salt concentrations that control supercoiling, the transition between the B and Z conformation of a DNA double helix,[28] the reversible formation of a G quadruplex with K+ ions,[29] as well as the formation of C-quadruplex motifs and triple helical structures by alteration of the pH value. [30] The environment-induced conformation change of DNA leads to the change of internal structure of the DNA-assembled nanoparticle structures, and eventually generates the switch of the physical signals, which allows for various biomedical applications.

The other type of dynamic disassembly process can be initiated, powered and quenched by the DNA reactions. This strategy, called strand-replacement, has been broadly applied. For this process, one of the DNA strands in a double helix can be selectively replaced by another sequence with higher affinity. In a typical design, if one strand of a duplex has a dangling end (in this context often called “toe hold”), the perfect Watson–Crick complement of the strand can hybridize to this toe hold [31]. Since the additional base pairs along the toe hold make the perfect duplex energetically more favorable than the shorter already-existing duplex, and the duplex is also more stable than the intermittent branched three-stranded structure. The perfectly

complementary strand replaces the shorter strand through branch migration. This simple concept opens up a lot of possibility for the dynamic assembly of the nanoparticles. In this case, the DNA is used not only as a structural material, but also as `fuel' to initiate a nanoparticle assembly and catalyze the reaction.

1.2.4 Self-assembly of DNA Functionalized Nanoparticles

1.2.4.1 Functionalization of Nanoparticles with DNA

The first work of DNA-functionalized nanoparticles appeared separately in 1996 by Mirkin and Alivisatos.[32, 33] Both reports demonstrated the successful functionalization of gold nanoparticles (AuNPs) with DNA oligonucleotides. Mirkin and coworkers prepared 13 nm gold nanoparticles and covered the surface with alkane-thiol modified DNA oligonucleotides. Rather than coat the surface with DNA oligonucleotides, Alivisatos and coworkers attached alkane-thiol modified DNA to 1.4 nm AuNPs bearing a single maleimide group. Although each used distinct AuNP surface modification strategies, both were able to demonstrate DNA-directed assembly of functionalized nanoparticles. Since these first reports, a general strategy for the functionalization of gold nanoparticles with DNA has emerged. Typically, spherical AuNPs are stabilized in citrate. The citrate-Au surface interaction is relatively weak, and alkylthiol functionalized DNA can be used to replace surface bound citrate to generate stable particles with surface-bound oligonucleotides. The number of oligonucleotides on the surface can be tuned by varying the ratio of DNA to AuNP, adjusting the salt concentration throughout the functionalization process, and varying the size of the AuNP.

A nanoparticle with one ssDNA strand attached has a single connection, which is suitable for fabrication of small nanoclusters. However, the major disadvantage of this building block is low

fabrication yield, owing to the electrophoresis process.[34-36] Experimentally, the nanoparticles with fully covered DNA allow a much higher yield. The large ratio of the nanoparticle surface area to a footprint of anchored DNA allows for higher DNA packing density, which makes local DNA molecular recognition more effective, but also leads to a deviation of properties of DNAs on particles from their free-state behavior.[37, 38] For example, nanoparticles with fully covered DNA usually exhibit a higher melting temperature and better recognition efficiency compared with free DNA strands.

Recently, quantum dots, carbon nanotubes, and iron oxide nanoparticles have emerged as substrates for DNA functionalization. [3, 39, 40] Similar to gold nanoparticles, these materials demonstrate tunable optical properties. However, they also demonstrate additional electrical and magnetic properties that can be harnessed for molecular diagnostics and therapeutics. Unlike AuNPs, these materials are not readily functionalized with DNA, and require more extensive synthetic manipulations.

1.2.4.2 Theoretical Consideration of DNA Self-assembled Nanoparticles

For the DNA coated colloidal particles, the two contributions to the interaction free energy are: (i) the attraction mediated by the hybridization of complementary strands tethered on different particles, and (ii) the repulsion due to the compression of the DNA brush between the two surfaces[41]. Attraction and repulsion contribution can be quantitatively estimated as follows. The attraction contribution can be estimated by a two-step calculation[42]. First, one needs to calculate the free energy of hybridization for each pair of interacting tethered sticky ends in the system, which differs from the free energy of the hybridization of non-tethered (free in solution) sticky ends. Second, the overall free energy of interaction between two DNA coated colloidal

particles can be determined. The steric repulsion of the DNA shells can be calculated by finding the probability of their connected configuration in a confined environment using a statistical mechanics method. The detailed calculation model can be found in references. [43-48]

The thermodynamic and kinetic process of DNA-assembled structures has been systematically studied and predicted by theoretical and computational work. Those studies reveal the formation of structures of DNA-coated colloidal particles as a function of various physical parameters such as temperature, the design of DNA recognitions, and volume fraction of the forming structure. Since the reaction free energy can be presented by $\Delta G = H - \Delta ST$, the most convenient way to change the reaction free energy, $\Delta G,$, is varying temperature. Indeed, temperature has a very significant impact on the phase behavior of the DNA-assembled colloidal/nanoparticles. Calculated results point out the relationship between the bonding fractions (fraction of bonds over maximum number of possible connections) as a function of the temperature.[44, 47] There is a steep increase of the bonding fraction as one decreases the temperature, which corresponds to the melting temperature of DNA-modified systems, which is due to the multiple binding effects. The target crystal structure can only emerge at a very narrow temperature window, although they are thermodynamically and kinetically accessible. In order to resolve their low-crystal ability, one can introduce the competition of intra-inter particle strand hybridization. This leads to a re-entrant melting which strongly suppresses kinetic trapping of the system in a non-target structure [46]. The length of the DNA shells also contributes to the repulsion between particles. In particular, the phase diagram as a function of volume fractions has also been explored by computational methods and the result shows the coincidence with experimental data. Combining all these effects, the target structures and their interparticle distances can be predicted by pair potential as a function of temperature and volume fractions.

For example, a model system described in the literature is a binary system of hard spheres with the same diameters *d*[49]: species A and B which create the reversible binding energy E. At the same time, the same type of particles repels each other with the soft-core potential U(r). The phase behavior of this model system has been explored as a function of the aspect ratio, and the relative strength of the attraction, $E=U_0$. Let r_k be a distance to the *k*th nearest neighbor of particle in a given structure. Let Z_k be the average number of cohesive contacts per particle and Z is the coordination number. If entropic effects are neglected, the energy of the particles can be described as follows:

$$u = \frac{1}{2}(-ZE + \sum_{k=2}^{\infty} Z_k U(r_k)) \approx \frac{1}{2}[-ZE + Z_2 U(r_2)] \qquad \textbf{(1.3)}$$

The contribution from interaction with particles beyond the second nearest neighbor is neglected. Since the equilibrium structure is likely to possess a high symmetry, only crystalline morphologies have been considered, in which all the sites are equivalent. All plausible morphologies have been identified by changing the coordination numbers. BCC (Z=8), simple cubic (SC, Z=6), honeycomb (HS, Z=5), and diamond (Z=4). The system is shown to exhibit surprisingly diverse and unusual morphologies.

These theoretical studies demonstrate various strategies to control the self-assembly process of DNA-coated colloidal particles by tuning physical parameters of the system and provide an important guidance to experimental design. The experimental details will be described as follows.

1.2.4.3 Challenges for the Self-assembly of DNA Functionalized Particles and Corresponding solutions

Physical intuition borrowed from atomic and molecular physics lead many to think that nanoparticles functionalized with DNA strands would eventually arrange in crystalline phases by minimizing the system's free energy. However, there are two challenges to achieve this equilibrium states. [41]

The first critical aspect is kinetics. The strong interaction of nanoparticles through complementary ssDNA strands will trap the system to a metastable free-energy minima, slowing down equilibration dramatically. One efficient way to reduce interparticle interaction is grafting the inert polymers or inert DNA strands (referred to as neutral strand DNA). The inert polymers or DNA strands occupy grafting sites on the surface, reducing the grafting density of active strands. Meanwhile, it causes the steric repulsion to the surface of two approaching nanoparticles. [50-52].Therefore, the kinetics of an aggregation reaction can be determined by the inert polymer grafting density, as well as their morphological parameters (such as length, shape and rigidity). Another way to reduce the attractive strength between nanoparticles is designing sticky ends, which form hairpins and intra-collodial loops, thereby reducing the number of interparticle bridges.

The second critical aspect is the strength, range and temperature dependence of DNA- mediated interactions. DNA-mediated interactions are very sensitive to temperature. The melting temperature of the aggregation formed from DNA-functionalized particles is significantly higher than what can be expected from the single-stranded DNA, due to the increase in the binding energy between two nanoparticles caused by multiple linkages.[37] Moreover, the transit of the melting temperature is much sharper than it is for free DNAs due to multiple linker effects. The accurate prediction of the DNA melting temperature is essential to get a high-ordered structure, and has drawn a lot of theoretical attention.

1.2.4.4 Fabrication of 3D Nanocrystals

Considering these two aspects, our group has reported the thermally reversible fabrication of discrete 3D DNA-AuNP crystal structures from the binary mixture of nanoparticles with the interspecies attraction produced by sticky ends, which are complementary single-stranded overhangs protruding from the ends of DNA duplexes offering a convenient and efficient cohesion tool. The body-centered-cubic (BCC) lattice structure obtained is temperature-tunable and structurally open, with particles occupying only 4% of the unit cell volume (Figure 1.4). Further work demonstrated that if one type of the nanoparticle was replaced by quantum dots with lower contrast, one will get the single-cubic crystal structure.[51]

In the same issue of Nature, Mirkin and his co-workers investigated the aggregation of nanoparticles in both a binary mixture system and a single-component system, in which the attraction was provided by duplex linkers. In a single-component system, they found that the system crystallized into a closed-packed face-centered cubic (FCC) structure[53, 54].

Compared with direct hybridization, the introduction of linker DNAs, which bind to the end of DNA strings grafted on the particle surface, bring more flexibility to the system, making it easier to tune the number of connections between various particle species[55, 56]. In addition, the morphology of DNA linker can vary from simple flexible ssDNA linkers and rigid dsDNA linkers to more complicated DNA nano-objects, which allows for the diversity of assembled structures. Experimentally, the adjustment of the linker system can be simply achieved by tuning linker parameters such as number, rigidity, and length, without going through tedious steps to functionalize various types of DNA on the nanoparticle surface[57].

Figure 1.4. a,b Schematic of experimental design for the fabrication of 3D crystal. **c.** Representative transmission (top) and scanning (middle, bottom) electron microscopy images of nanoparticles before (top) and after (middle, bottom) assembly at room temperature. **d.** Typical example of experimental measurements that reveal a correlation between the ultraviolet–visible melting profile of the aggregate and its internal structure as probed by in situ SAXS measurements at room temperature, pre-melting temperature, and above the disassembly/melting temperature.[51] Reprinted with permission from Reference 51. Copyright 2008, Nature Publishing Group.

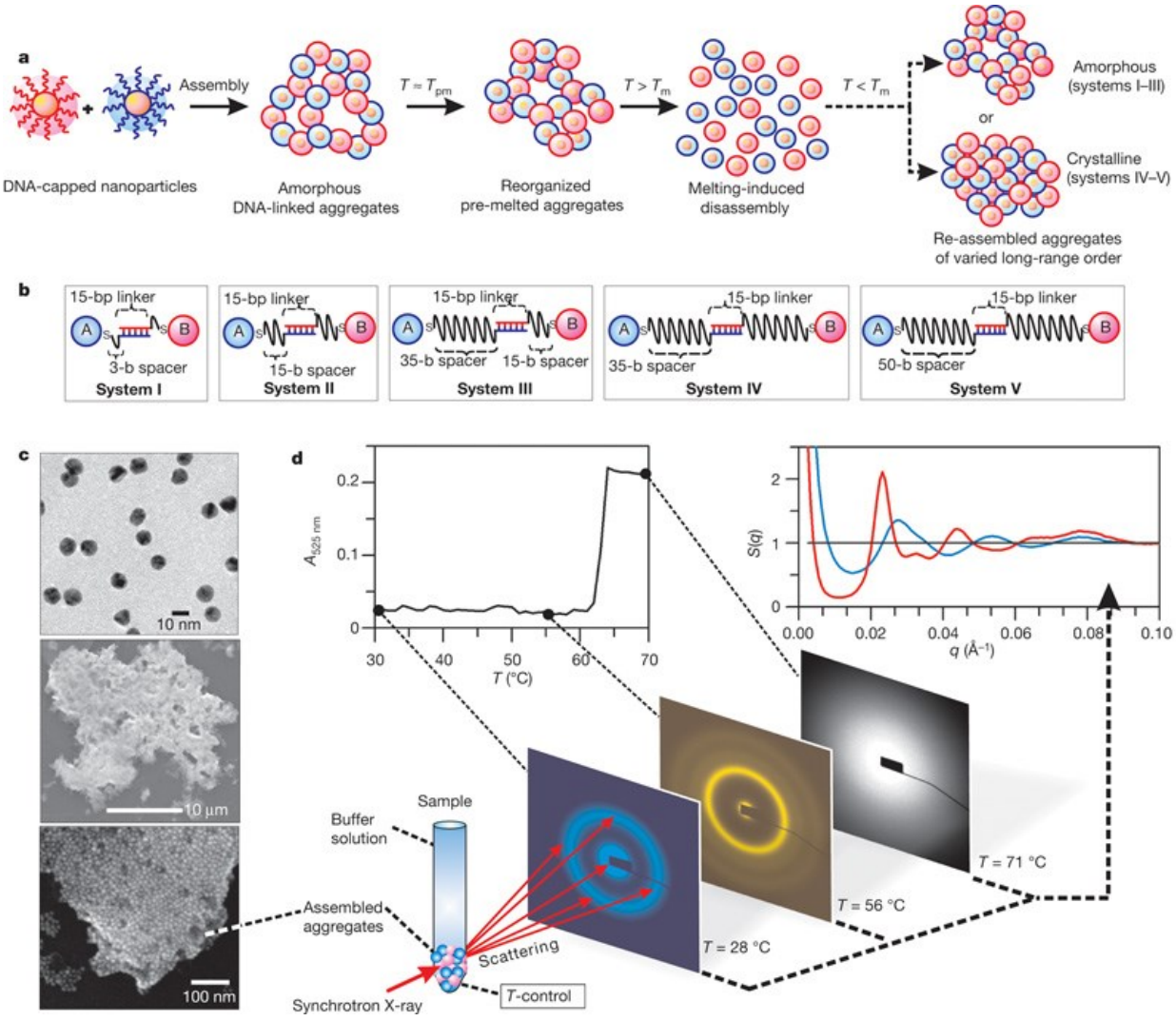

The flexible ssDNA linker also allows for the formation of crystal structure as which we observed in the direct hybridization system.[55, 56] When flexible single-stranded linker DNAs are added to the mixture of two types of dispersions, ssDNAs fully-covered gold nanoparticles which are noncomplementary to each other, but complementary to the respective ends of the linker DNA, a crystalline phase of body-centered cubic unit cell is formed at the premelting temperature of the system. Further studies revealed that the internal structure of these BCC crystals is dependent on the DNA linker length and linker ratios. The formation of a crystalline bcc phase was observed for a broad range of linker lengths, while the number of linkers per particle controlled the onset of system crystallization. Mirkin et al found the similar effect in their system with duplex linkers.[58, 59] They reported that the unit-cell size depends linearly on the length of the DNA bridges. The crystallization of the nanoparticles is only possible at given linker ratio and linker length.

The lattice structure of the assembled nanoparticles is also determined by the size ratio of the nanoparticles, as well as their linker ratios. [60] Mirkin and coworkers reported the results of an accurate study of the crystallization of gold NPs, and worked out a set of six empirical rules to determine the structure and lattice parameters of a crystal as a function of particle size and the length and number of the DNA tethers. They observed the formation of nine distinct crystal structures. Instead of spherical gold nanoparticles, the crystallized 3D structures can also be obtained using anisotropic units such as nano-cubes, nano-rods, and prisms[61].

1.2.4.5 Nanoclusters Built from DNA Functionalized Particles

Compare with the 3D structure, finite size nanoclusters can be viewed as nanoscale analogue of molecules. Analogously to molecules that give access to new properties of atoms, nanoclusters

are attractive for modulation of optical, magnetic, and catalytic properties of nanoparticles (Figure 1.6). For example, if the quantum dot was placed next to a gold nanoparticle, photoluminescence of quantum dot can either be quenched or enhanced up to 20 folds depending on the size of the gold nanoparticles as well as their interparticle distance.[62, 63] Therefore, a nanocluster can be treated as artificial molecule which not only contains the properties of the single particles but also exhibits the properties which does not exist in the bulk materials. This nanocluster might be utilized as a simple building block to build complex hierarchical structures as the molecules would naturally. Moreover, because of their simple structures, nanoclusters lead to a broad range of applications on the scale of single-molecule levels.

Figure 1.6. Schematic illustration of building a finite size nanocluster

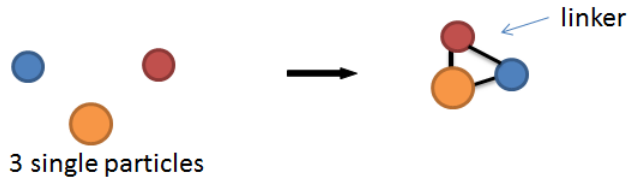

One of the goals of our studies is to develop the fabrication of finite size nanoclusters with precisely controlled number of particles in the clusters which are located in a designed location. Here, DNA plays a dual role: it selectively assembles the clusters in solution and functions as an insulating spacer between the nanoparticles.[64] The challenge for fabrication of DNA functionalized nanoclusters is following: the high concentration of reactant nanoparticles which are fully covered by DNA easily leads to the large aggregations of the nanoparticles. When the concentration of nanoparticles is decreased, nanoclusters with a broad distribution of particle s and nanostructures are obtained. To overcome these challenges, the seveal strategies have been developed.

In the first strategy, one can constrain the connection of nanoparticles by limiting the number of DNA connections. Nanoparticles with only one single-stranded DNA attached have been applied as the building block. For example, a dimer can be obtained by mixing two nanoparticle functionalized with one single-stranded DNA which is complementary to each other, the interparticle distance can be easily adjusted by the length of DNA linkers. The method allows for fabrication of both symmetric homodimer nanoclusters and asymmetric heterdimer with two different types of particles connected together, such as gold/silver nanoclusters, and gold/quantum dot nanoclusters.[33, 35, 62] The optical properties of these nanoclusters as a function of interparticle distance, size of the particles as well as the type of connecting particles have been systematically explored.

A tetrahedral shape of nanoclusters with 4 nanoparticles at the conner of the structure is synthesized by 4 types of DNA functionalized particles with DNA. These 4 DNA sequences are complementary hybridize with each other. Each of them can be segmented into three pieces. Each piece is complementary to a third of each of the other strands. So, each strand of DNA "weaves" through three pyramid sides outlining one face of the pyramid. The perimeter length is determined by the number of complementary base pairs. [65] The chirality in the nanoscale can be achieved by applying various types of the particles from metallic gold and silver nanoparticles and semiconductor QD. The position of CD signals can be varied in a wide range of UV and visible wavelengths, 350−550 nm, with a strong potential to be extended into the near-IR region for narrow-band gap quantum dots.

The second strategy to achieve the three dimensional well-defined anisotropic nanocluster structure is using DNA origami as a template. For example, the bifacial DNA origami-directed self-assembly of 3D Au nano-rod dimer can be generated. The optical chirality can be tailored in

a spatial-configuration dependent manner. [66] Gold nanoparticles (AuNPs) and semiconducting quantum dots (QDs) are integrated on a single DNA origami scaffold. The separation of Gold nanoparticles can be engineered by controlling the connection position of the particles. However, the disadvantage of the first two strategies is their low yield since a lot of samples were sacrificed during the electrophoresis process, which was used to select the nanoparticle with only one DNA strand attached. In order to overcome this disadvantage, nanoparticles which are fully covered with DNA as a building block can be also applied to fabricate nanoclusters, due to their easy fabrication steps and relatively higher purity and concentration of the single particles. [67]

In the third strategy, the aggregation of the nanoparticle can be limited by the entropy effect related to the steric occupation in the given space. In this strategy, particles which are fully functionalized with DNA have been used as building block. For example, Jonathan A. Fan et al fabricated heteropentamer clusters, which consist of a smaller gold sphere surrounded by a ring of four larger spheres, by incubating with two DNA functionalized components. The molar ratio of these two components is 12:1, which leads to the high purification of nanoclusters. Magnetic and Fano-like resonances are observed in individual clusters.[64]

Another example of taking advantage of this strategy to fabricate nanoclusters is demonstrated in our group, which is one can using a surface to block the self-assembly from one direction to fabricate Janus particle, Janus clusters and dimers. In this method nanoparticle dimers were assembled in a sequential manner by a deposition of DNA encoded particles on a layer of either surface-grafted ssDNA, or DNA functionalized particles with complementary recognition. The dimer fabrication procedure is shown in Figure 1.6, in which the first particle, linker DNAs and the second particles were added step-by-step on an DNA grafted surface. The assembled dimers were released from surface by a release strand. The distribution of the dimer nanoclusters can be

proved by both the transmission microscopy and dynamic light scattering (DLS). By counting the number of nanoparticles from the SEM we concluded that more than 75% of dimer nanoclusters in the product. The hydrodynamic radius of the particles increased from 18nm (for single particles) to 34nm, which also suggests the high yield of dimer formation. It is important to notice that several factors led to the success of the dimer formation: 1.Surface block the linkers attachment from one side of the particles, therefore the linker only connect the facing hemisphere of the nanoparticles. 2. Number of linkers is controlled to 4~6 per dimers, which limits the formation of nanoclusters with more than 3 particles. Besides, when one particle was connected to the particle on surface by linkers, this particle will grab the rest of the linkers avoiding the connection from the 3rd particles. Using the similar step-wise method, we can also obtain the high yield of the Janus particles and nanoclusters. This strategy demonstrated higher efficiency to fabricate nanoclusters compared with the previous method. However, the formation directionality and selectivity of this strategy is not as significant as previous two strategies.

As an outlook, it would be highly desirable if one can create the nanoparticle unit analogue of atoms with valence in order to build a complex or low-coordination structures. This type of structure is common in atomic and molecular systems but rare in the nano/colloidal domain. This hypothesis has just been recently proved by experiments in the colloidal domain. Functionalized with DNA with single-stranded sticky ends, patches on different particles can form highly directional bonds through programmable, specific and reversible DNA hybridization. These features allow the particles to self-assemble into 'colloidal molecules' with triangular, tetrahedral and other bonding symmetries. [68] The computational study also suggests that NPs that are directionally functionalized with DNAs allows one to avoid unwanted metastable configurations, which have been shown to lead to slow self-assembly kinetics even in much simpler systems. A

variety of target mesoscopic objects can be designed and self-assembled in near perfect yield using these types of the nanoclusters. [69]Experimentally, it is challenging to fabricate nanoparticles which are directionally functionalized with DNA. However, it has been demonstrated that the nanoparticles with directionally functionalization with DNA may be achieved by put a geometrical template made of DNA on the surface of functionalizing particle surface.[70] More efforts are still need to be attributed to this study.

Figure 1.6. The assembly and encoding steps in fabricating Janus particles (a) and clusters (b and c) using stepwise surface encoding approach. The nanoparticle grafted with two types of ss-stranded DNA (A and B) first interacts with surface grafted with DNA A' by 15 bases DNA complementary strands, in the second step a linker (B'C') was binding to the DNA grafted on upper hemisphere of the nanoparticle through 15 bases DNA complementary due to the block of surface. The dimer (b) and Janus clusters (c) can be fabricated by adding the second type of particle grafted with DNA C on the nanoparticle surface complementary to the overhang part of linker strand (C' end) . The detailed of nanostructure can be tuned by the size and number ratio of second types of nanoparticles. The final products on the surface can be released by DNA A'' which has higher affinity to A' than it does for DNA A on the nanoparticle surface [71] Reprinted with permission from Reference 71. Copyright 2009, Nature Publishing Group.

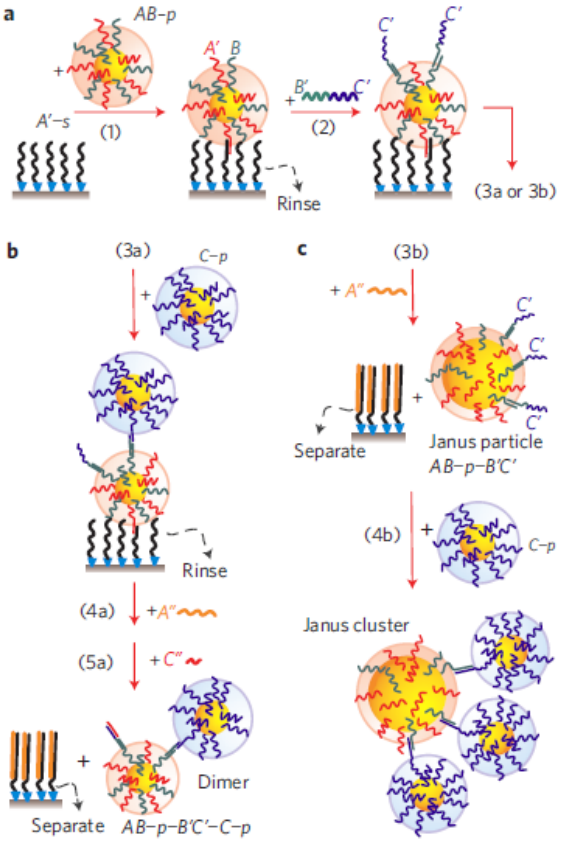

1.3. Characterization Methods

The stabilized, assembled structure can be conveniently characterized by using microscopies such as transmission electron microscopy (TEM), scanning electron microscopy, and atomic force microscopy (AFM). The variation of the optical properties of assembled structures can be detected by a wide range of optical microscopies, such as fluorescence confocal microcopy and total internal reflection microscopy (TIRF). As major experimental tools to study colloidal suspensions and polymers, light scattering-based methods (such as dynamic light scattering and static light scattering) have been widely applied to study the assembly process of DNA-functionalized system. Therefore, in the following part, I will briefly introduce the principles of static scattering and dynamic scattering methods.

1.3.1 Small Angle X-ray Scattering

1.3.1.1 Basics of X-ray Scattering

A static scattering experiment probes the order of particle aggregates and the distances of neighboring particles. [72]When the incident beam (X-ray) encounters a scatterer, two processes are taking place: 1. The incident beam (X-ray) is scattered by the scatterers and 2. The scattered wave is interference with each other. The beam is absorbed by the objects. However, here we only consider the elastic scattering in which the beam has only been scattered by the objects with the invariable wave-length of the X-ray. Strictly speaking, the term “scattering” refers only to phenomenon (1), whereas the term “diffraction” refers to the combination of (1) and (2). In current practice, the term diffraction tends to be used only when the sample is crystalline. When the scattering pattern is diffuse and, especially when the pattern of interest is mainly in the small-

angle regime, the term scattering is almost exclusively used, even when the phenomena involve the combination of (1) and (2).

A schematic description of the scattering experiment is shown below:

Figure 1.7. Typical scattering experiment setup

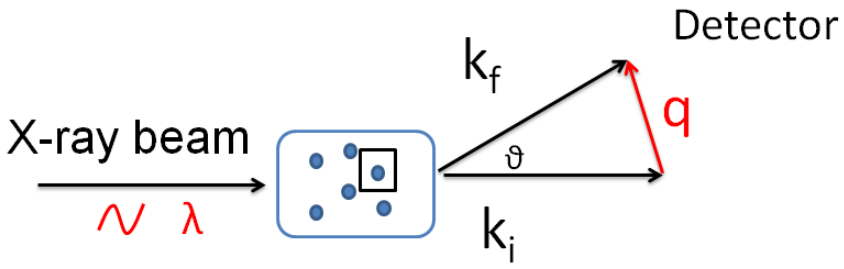

An incident beam with a wavelength (λ) is impringed on the scatterer, the direction of the incident beam changes with a scattering angle ϑ, and then is collected by the detector which measures the intensity of the scattered light, I(q), in which q ($s = \frac{q}{2\pi}$) is the scattering wave vector equal to k_f-k_i, the modulus of which can be described by

$$q \equiv 2\pi s = \left(\frac{4\pi}{\lambda}\right)\sin\left(\frac{\vartheta}{2}\right) \qquad (1.4)$$

The amplititude of a scattering wave can be expressed as

$$A(s) = A_0\, b \int_V n(r) e^{-i2\pi sr} dr \qquad (1.5)$$

Where V in the integration sign denotes that the integration is to be performed over the scattering volume, that is, the entire sample volume when the incident beam cross section is larger than the sample dimension, or over the illuminated volume when the sample volume is larger. n(r)dr represents the number of scatters within a volume element dr=dx dy dz

The equation 1.5 can be rewritten as a function of q

$$A(q) = b \int_V \rho(r) e^{-iqr} dr \qquad (1.6)$$

Here, A(q) stands for the normalized amplitude, i.e., the ratio A(q)/A0, ρ(r) is the scattering length density distribution, in the case of X-ray scattering, density distribution n(r) multipled by b,

$$\rho(r) = \sum_\alpha b_\alpha n_\alpha(r) \qquad (1.7)$$

Where α refers to the different atomic species represent.

1.3.1.2 Auto-correlation Function and Reciprocal Space

If we assumed that the scattering is weak so that the scattering of a photon occurs only once within the sample, this is an approach is kinematic approach. Therefore, the scattered intensity I(q) can be presented as

$$I(q) = |A(q)|^2 = \left| \int_V \rho(r) e^{-i2\pi sr} dr \right|^2 \qquad (1.8)$$

During the measurement, the position of r_j of atoms and the scattering length density distribution $\rho(r)$ may change due to the thermal motion of the atoms. The intensity I(q) actually measures the average scattering over the time.

We now rewrite the formula as

$$I(q) = \langle |A(q)|^2 \rangle = \langle \left| \int_V \rho(r) e^{-iqr} dr \right|^2 \rangle \qquad (1.9)$$

Where <…> denotes the ensemble average. Considering the space difference, we can rewrite I(q) as follows

$$I(q) = \int [\int \rho(u)\rho(u+r)du]e^{-iqr}\, dr = \int \mathrm{T}_\rho(r)\, e^{-iqr}\, dr \qquad (1.10)$$

Where $\mathrm{T}\rho(r)$ is defined as auto-correlation function of $\rho(r)$, where $\mathrm{T}_\rho(r) = \int \rho(u)\, \rho(u+r)$.

The scattering vector s or q has dimension of length $^{-1}$ and spans a three dimentional-recipical space. The information on the structure of the sample is contained in the function $\rho(r)$ in real space, and its Fourier transform gives the amplitude A(s), a function in reciprocal space. If A(s) could be determined over all s, the real space function $\rho(r)$ is recovered by the inverse Fourier transform

$$\rho(r) = \int A(s)e^{i2\pi sr}ds \qquad (1.11)$$

The information contents of $\rho(r)$ and A(s) are therefore entirely equivalent to each other. The intensity I(s) in reciprocal space is given by $\mathrm{T}_\rho(r) = \int I(s)e^{i2\pi sr}ds$.

In summary, the relationship among ρ(r), $\mathrm{T}_\rho(r)$, A(s), and I(s) can be demonstrated in Figure 1.8:

Figure1.8. Relationship among ρ(r), $\mathrm{T}_\rho(r)$, A(s), and I(s). [72]

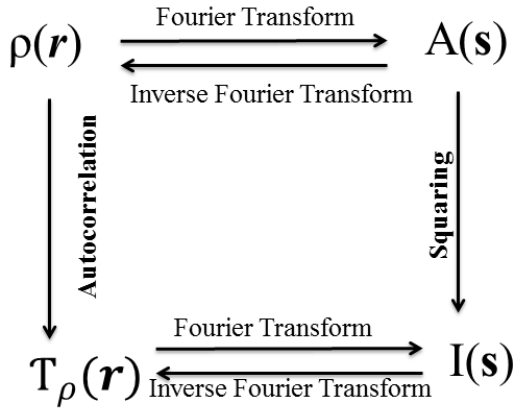

1.3.1.3 Small Angle X-ray Scattering

The technique known as of Small-Angle Scattering (SAXS) is used to study the structures with sizes on the order of 1nm or larger. Information on such relatively large-scale structure is contained in the intensity of the scattering x-rays or neutron at small angles. The reciprocity between r and q means that information on relatively large r is contained in I(q) at relatively small q. Most of models that are adopted in practice for analysis of small-angle data belong to one of the following four: a dilute particle system, a non-particle two-phase system, a periodic system and a soluble blend system.

In my studied system, I applied SAXS to probe dilute systems. Particles (polymer molecules, colloidal particles) of one material are dispersed in a uniform maxtrix of a second material. When the concentration of the particles is sufficiently dilute,the positions of individual particles, far apart from each other, are uncorrelated. Under this circumstance the waves scattered from different particles are incoherent among them, and the observed intensity of simply becomes a sum of the individual scattering. If the shape of particles is known or assumed on the basis of independent information, the intensity of the scattering from individual particles can be calculated and compared with the observation.

For many of particles having well-defined, simple geometric shape it is possible to calculate the intensity curve for the wide range of q without making any approximations. Now the integration is performed over only the particle volume v.

For example, for spherical particles, the solid sphere of radius R with a uniform density ρ_0 is defined by

$$\rho(r) = \begin{cases} \rho_0 & for\ r \le R \\ 0 & for\ r > R \end{cases} \quad (1.12)$$

The amplitude can be represents as follows

$$A(q) = \int_0^\infty \rho(r) 4\pi r^2 \frac{sinqr}{qr} dr = \frac{\rho_0}{q} \int_0^R 4\pi r sin(qr) dr, \quad (1.13)$$

Which,on integration by parts yields

$$A(q) = \rho_0 v \frac{3(sinqR - qRcosqR)}{(qR)^3} \quad (1.14)$$

Where *v* is the volume of the sphere, $(4/3)\pi R^3$. The intensity of scattering from sphere is therefore

$$I(q) = \rho^2 v^2 \frac{9(sinqR - qRconsR)^2}{(qR)^6}$$

1.3.1.4 Diffraction by Crystals

A crystal consists of a large number of unit cells arranged regularly in three dimensional space, which each unit cell having the identical atomic content. The shape and size of the unit cell are defined by the three unit cell vectors *a,b,c***.** The origin of each unit cell is on a lattice point, whose position is specified as

$$r_{uvw} = ua + vb + wc,$$

Where *u,v,w* are positive or negative integers or zero. The lattice consisting of all these lattice points is then represented mathematically as

$$z(r) = \sum_{u=-\infty}^{\infty} \sum_{v=-\infty}^{\infty} \sum_{w=-\infty}^{\infty} \delta(r - r_{uvw}) \quad (1.15)$$

The content of the unit cell is defined by specifying the positions of all the atom it contains. It is more convenient, however, to specify the unit cell content by the distribution ρ_u(r) of the appropriate scattering length density. The convolution product

$$\rho(r) = \rho_u(r) * z(r) \tag{1.16}$$

Then gives the scattering length distribution $\rho(r)$ in the crystal as a whole.

The amplitude A(s) of scattered X-rays is equal to the Fourier transform of $\rho \ \ (r)$, Therefore, the previous equation can be rewriten as

$$A(s) = F(s)Z(s) \tag{1.17}$$

Where F(s) is the structure factor of the unit cell, is the Fourier transform of $\rho_u(r)$ and Z(s) called the lattice factor, is the Fourier transform of $z(r)$. Z(s) is in the recipical space, and its lattice points are :

$$r^*_{hkl} = ha^* + kb^* + lc^* \tag{1.18}$$

Where *h,k,l* are integers. The three vectors a^*, b^* and c^* in reciprocal space define the reciprocal lattice and are related to the unit cell vectors a,b, and c in real space.

While *F(s)* is a continuously varying function of s, its magnitude is experimentally observable and therefore is meaningful only at discrete values of s corresponding to the reciprocal lattice points. Therefore the structure factor *F(q)* can in fact be replaced without loss of information, by triply infinite series $F_{hkl}(h, k, l = -\infty \cdots \infty)$ with

$$F_{hkl} \equiv F(r^*_{hkl}) = \int \rho_u\,(r) \exp(-i2\pi r^*_{hkl} r)\, dr \tag{1.19}$$

Therefore, if F_{hkl} is known for a large number of hkl refractions, one can obtain $\rho_u(r)$ and hence the positions of all the atoms in the unit cell.

1.3.2 Dynamic Light Scattering

Dynamic light scattering is the most common approach to probe the diffusion of particles in a solution. The result contains the information of the particle size and the solution conditions such as the viscosity of the environment. [73]

In dynamic light scattering, a detector at a certain angle collects the scattering signal from the ensemble of point individual scatters. However, during the Brownian motion of the particle, the center of mass and the orientation of the particles changes correspondingly, the scattered intensity fluctuates with time, which can be probed by dynamic light scattering.

The fluctuation of light can be quantitatively described by an intensity auto-correlation-functions, which can be presented by

$$gI(q,t) \equiv \langle I(q,t_0)I(q,t+t_0)\rangle \qquad (1.20)$$

The <…….>here represents the ensemble average of the intensity, I(q,t) is the instantaneous intensity which is related to the scattered electric field strength. One can image that when t_0 is very small compared to time typifying the fluctuation, I(q,t+t_0) is very close to I (q,t_0). As t_0 increase the deviation of I(q,t+t_0) is likely to be nonzero. Therefore, we can say that I($q,\ t$+t_0) is correlated with I (q,t_0) at small t_0 but this correlation is lost as t_0 become large compared with the period of the fluctuation.

Equation 1.20 exhibits the intensity correlation function measured the change of scattering light, which is the second auto-correlation function. Equation 1.21 can be rewrite as:

$$G_2(\tau) = \frac{1}{T}\int_0^T I(t)I(T+\tau)d\tau \quad (1.21)$$

The first auto-correlation function is the electric field correlation function, which describes correlated particle movement.

$$G_1(\tau) = \frac{1}{T}\int_0^T E(t)E(T+\tau)d\tau \quad (1.22)$$

The relationship between the second auto-correlation function and first auto-correlation function can be represent by Siegert equation:

$$G_2(\tau) = B[1+\beta G_1(\tau)^2] \quad (1.23)$$

where B is the baseline and β is an instrumental response, which is a correction factor that depends on the geometry and alignment of the laser beam in the light scattering setup, both of which are constants.

In the simplest case, the decay of first auto-correlation can be fitted as an exponential decay:

$$gi(\mathrm{T}) = \sum_i G_i(\mathrm{T})e^{-\mathrm{T}i\tau} \quad (1.24)$$

Where, $\sum_i G_i(\mathrm{T})$ is the intensity weighted coefficient associated with the contribution of each particle; $\mathrm{T} = -\mathrm{Dq}^2$, D is the diffusion coefficient of the particles, which is often used to calculate the hydrodynamic radius of a sphere through the Stokes–Einstein equation:

$$D = \frac{kT}{6\pi\eta r} \quad (1.25)$$

For the anisotropic particle, diffusion coefficient D can be represented as $D = kT/f$, f is a shape factor, which is a hydrodynamic term that depends on the paricle shape.

1.4. Outline of the Thesis

The successful formation of dimers with a high yield allows the application in various fields from biosensing to nanooptics. As far as my thesis is concerned, I will to discuss the four following directions:

1) As the simplest nanoclusters, dimer of nanoparticles provides an excellent platform to study fundamental soft matter problems, especially in a non-trivial regime when the linker size is comparable to the size of the nanoparticles. In Chapter 2, we report how the internal structure dependence on the linkage properties, such as the number, flexibility and length of linkers. Combining with our experimental, computational studies and theoretical model, we reveal a major effect in this type of systems.

In chapter 3, we extended the study to a more general case when there is no restriction to the connection position of ss-DNA linkers. In this case, the single-stranded linker exhibits more freedom on the connection morphologies, and allows for the assembly of more diverse structures. Moreover, we discover the new regime for the formation of self-limited nanoclusters.

2) Dimer is the most basic unit to build a hierarchical structure. Meanwhile, since the two particles in dimers were grafted with different types of DNA, its asymmetric properties leads to various interesting recognition behavior during the self-assembly process. Therefore, in the 2nd part, I will discuss in detail how to use dimers in self-assembly schemes. In chapter 4,

dimers' interaction with the recognizable surface will be demonstrated as a model system for understanding the fundamental mechanism of nano-object interacting with the surface. Using this knowledge, we develop a method to separate dimers from single particles. The preliminary results of how to use dimers for building a hierarchical structure will be discussed in details.

3) In the 3rd part, I am going to discuss the application of the dimer nanoclusters: In chapter 5, I will demonstrate an example of how we use dimer nanoclusters as nucleic acid detectors based on the disassembly of the nanoclusters. The detailed kinetic study provides insight into disassembly mechanism and kinetics of DNA interactions.

4) In order to fulfill various *in vivo* tasks, an efficient diffusion in a crowded environment is essential for the designed active nanostructure materials and devices. In the chapter 6, I will demonstrate our diffusion study on Janus particle and dimer in polymer solutions. In certain viscosity regimes, we observed a significant enhancement of diffusion for the asymmetric nanostructures as compared with symmetric ones.

Chapter 2

The Internal Structure of Nanoparticle Dimers Linked by DNA

2.1 Introduction

The use of DNA to link nanoparticles (NPs) into complex self-assembled structures is an increasingly popular approach to the bottom-up design of nanoclusters and materials.[32, 33, 74-76] The selectivity and reversibility of DNA base-pair recognition, coupled with the relative stiffness of double-stranded DNA (dsDNA) [77-79]and a tunable assembly kinetics[80] makes DNA an ideal choice to create programmable interactions between NPs . This is accomplished by tethering multiple strands of DNA to a core NP (gold, silver or CdSe core).[38, 81, 82] The outer-most part of tethered strands is single-stranded DNA (ssDNA) with a specific sequence that will either link directly to another NP, or connect to another NP *via* an additional linking strand. [59, 83] The hybridization of ssDNA in linking regions directs the self-assembly of nanoparticles into larger-scale structures. Their organization is controlled by the DNA sequences and linker architecture,[45, 84-87] as well as by the NP geometry.[61] Using this approach, the precise fabrication of small nanoclusters and the formation of two- and three-dimensional superlattices has been achieved.[60, 61, 63, 71, 88-91]

While the approach of single-step, direct assembly is promising, many biological materials – such as bone, hair, skin, and spider silk[92] – take advantage of a more complex hierarchical scheme. In such a scenario, assembly at each scale results in units or structures that enable assembly at a larger scale. These processes have been evolved over aeons, so the development of synthetic multiscale self-assembly will prove challenging. In the context of DNA-tethered NPs, the most basic unit in such a hierarchical approach is a dimer of two NPs. As a first step toward a synthetic multiscale assembly, here we examine in detail the structure of dimer units. The structure of these dimers is complicated by the fact that the surface curvature of the NP is on a scale comparable to the length of the connecting DNA. In such a regime, the behavior of polymer chains (such as DNA) attached to the surface is known to deviate significantly from the free-chain behavior. [52, 93]

In this paper, we examine the structure of DNA-linked NP dimers by a combination of *in-situ* dynamic light scattering (DLS) and small-angle X-ray scattering (SAXS), complemented by molecular simulations and theory. The DLS method probes a hydrodynamic measure of an angular-averaged dimer size. The *in-situ* SAXS experiments reveal more detailed information on the interparticle distances within the dimer. The numerical modeling provides a detailed molecular picture that helps to interpret the experimental findings and develop a theoretical description.

When the NPs are linked by dsDNA with a separation less than the persistence length, the interparticle distance is a linear function of the DNA length, due to the rigidity of dsDNA. For longer ssDNA linkers, the deviations from linear dependence are well described by the worm-like chain (WLC) model. When the linkage includes a section of ssDNA – which has an order of magnitude smaller persistence length than dsDNA[94-98]– the flexibility of ssDNA introduces

significant complications to understand the dimer separation, especially if the NPs are linked by strands formed by a combination of ssDNA and dsDNA regions. Previous work on NP superlattices with ssDNA linkage[83] has shown that the interparticle distance can be used to estimate the end-to-end distance of the DNA chains using the WLC model, and assuming the persistence length of ssDNA. As we show below, the interparticle distances of the dimer units are significantly smaller than in the NP superlattice for the same length ssDNA linkers, and the use of a naive WLC description would require an unreasonable persistence length. The molecular simulations reveal the origin of this discrepancy is in the geometry of NP links. We use this information to construct a simple analytical model that captures the observed behavior. Our findings demonstrate that interparticle separation is dictated by end-to-end distance of DNA bridges as well as by the interplay of a particle's curvature and the excluded volume effects.

2.2 Experimental Design

The systems of dimers were prepared using a stepwise surface assembly method (Fig. 2.1), [71]in which nanoparticle dimers were assembled in a sequential manner by a deposition of DNA encoded particles on a layer of either surface-grafted ssDNA, or DNA functionalized particles with complementary recognition, as described below. The micrometer-sized (1–4 μm) streptavidin-coated magnetic-beads[71, 99] were used as surfaces for particle bindings and dimer assembly. The fabricated dimers were composed of nanoparticles with an 11 nm gold core (AuNP) covered by a shell of ssDNA. The particles within a dimer were connected by ssDNA linkers with ends that are complimentary to the ssDNA on the particle shells. The dimers fabrication procedure is schematically illustrated in Figure 2.1: the first particle(Au_1), linker

DNAs (DNA_L) and the second particles(Au_2) were added step-by-step to a DNA grafted surface. The assembled dimers were released from surface by adding strands with a higher affinity to the surface DNAs, as described in the method part.

Figure 2.1. Schematic of the experimental dimer fabrication process using a stepwise surface encoded method as described in the text and illustration of NPs connected by multiple DNA linkers with length *L*.

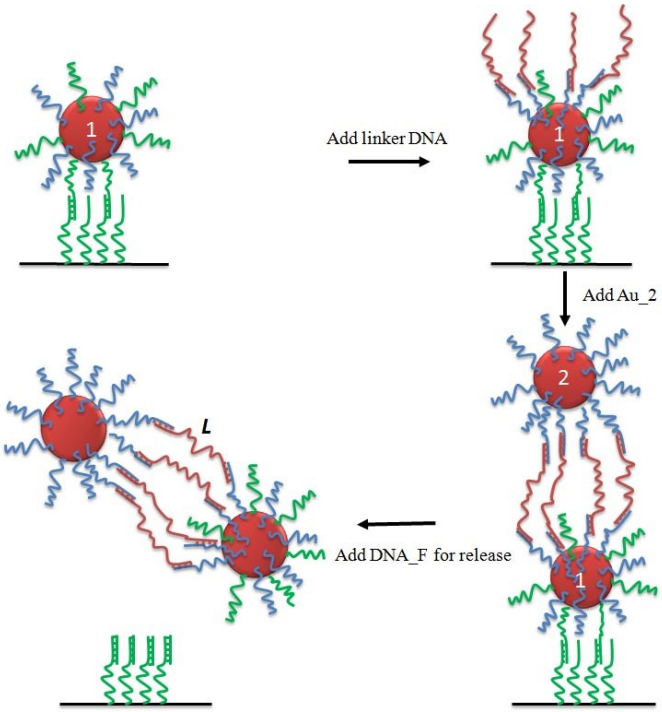

To study the dependence of the particle-particle separation within the dimer as a function of linker length ***L***, we used a series of single-stranded linkers DNA_L (Fig. 2.1, pink strand) as interparticle connectors, where ***L*** denotes a number of polythymine bases (T) in a single-stranded linker, not counting recognition ends. We considered ***L*** = 0, 24, 42, 60 or 75 bases. The ratio of pairs-to-DNA linkers corresponds to the average number of linkages within a dimer, equal to four in this study. Our previous work demonstrated that, at this ratio, a surface efficiently blocks

an attachment of linkers to a particle's hemisphere that faces a surface.[71] Therefore, most of the interparticle connections are established on the top hemisphere of Au_1, opposite to the surface, allowing for hybridization with DNA_2 located on a lower hemisphere of Au_2. The rigidity of interparticle linkers can be controlled by adding the corresponding complementary strand. In this case, a flexible single stranded linker becomes a rigid double strand connector due to the large increase in persistence length of dsDNA relative to ssDNA. The product has been characterized by TEM and UV-vis as shown in Figure 2.2 and Figure 2.3.

The DLS measurements conducted during the dimer fabrication process indicated a considerable increase of a number-averaged hydrodynamic diameter (D_h) of nanoclusters, from 20 nm for the isolated DNA-coated nanoparticle to about 29 nm and to 37 nm for dimers with $\boldsymbol{L}$ increasing from 0 to 75 bases, respectively (Fig. 2.4 (a)). The detailed studies, discussed in the results section, relate the D_h increase with a linker length change. We also examined the population of the fabricated clusters, as dried from the solution, by transmission electron microscopy (TEM). We observed that for the shortest linker $\boldsymbol{L}$=0, the assembled population consists of about 70% dimers, about 25% of unreacted particles, and 5% multimers (n≥3), which is in agreement with our previous studies. For the longest linker, $\boldsymbol{L}$=75, the dimer assembly yield decreased to about 50% due to the reduction of DNA binding efficiency for longer linkers (Figure 2.2 and 2.3). We further applied synchrotron-based SAXS methods to investigate the dependence of the interparticle distance in dimers on L, as well as on temperature, by probing a structure factor $S(q)$ of assembled clusters in a solution.

Figure 2.2. Representative Transmission Electron Microscopy of dimers linked by ***L=0 (a)*** and ***L=75(b).*** The scale bar is 30nm for both TEM images. The statistics histograms based on counting number of particle in TEM images indicate dimer yields of about 75% for ***L=0(c)*** and around 60% **for *L=75(d)***, based on about few hundred particles

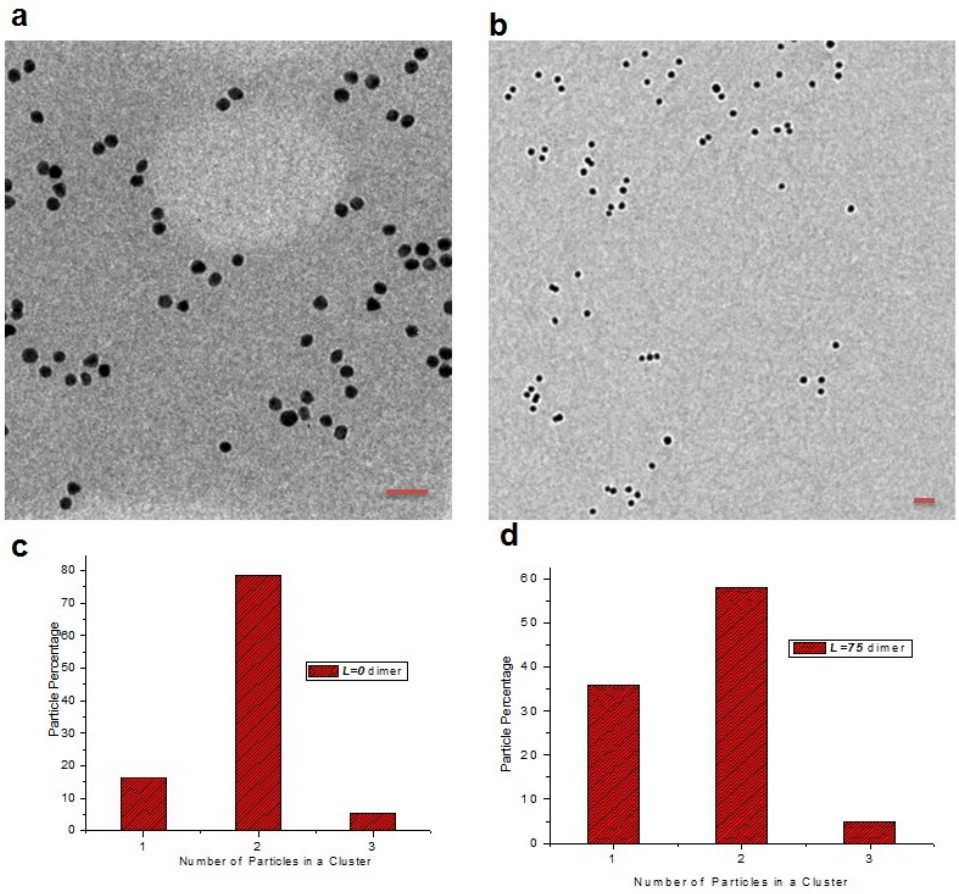

Figure 2.3. Representative UV-vis curves of dimers linked by *L=0* (a), *L=24*(b), *L=42*(c), *L=60*(d), *L=75*(e) and not-reacted single particles at the room temperature (T=26 ^{o}C). The observed surface plasmon resonance bandshift ($\Delta\lambda/\lambda_0$, λ_0=521 nm) is estimated using plasmonic ruler equation as $\frac{\Delta\lambda}{\lambda 0} = 0.06 \times \exp\left(-\frac{\frac{d}{D}}{0.14}\right)$, where the ratio of interparticle distance to particle diameter (d/D) is calculated based on d obtained from SAXS at T=26 ^{o}C and D=11 nm, the coefficients are as in our previous study. For the experimental d/D ratios, calculated $\Delta\lambda$ is less than 0.1nm, i.e. below the resolution of UV-Vis detection; no bandshift is observed in the experiments due to assembly of single particles in dimers.

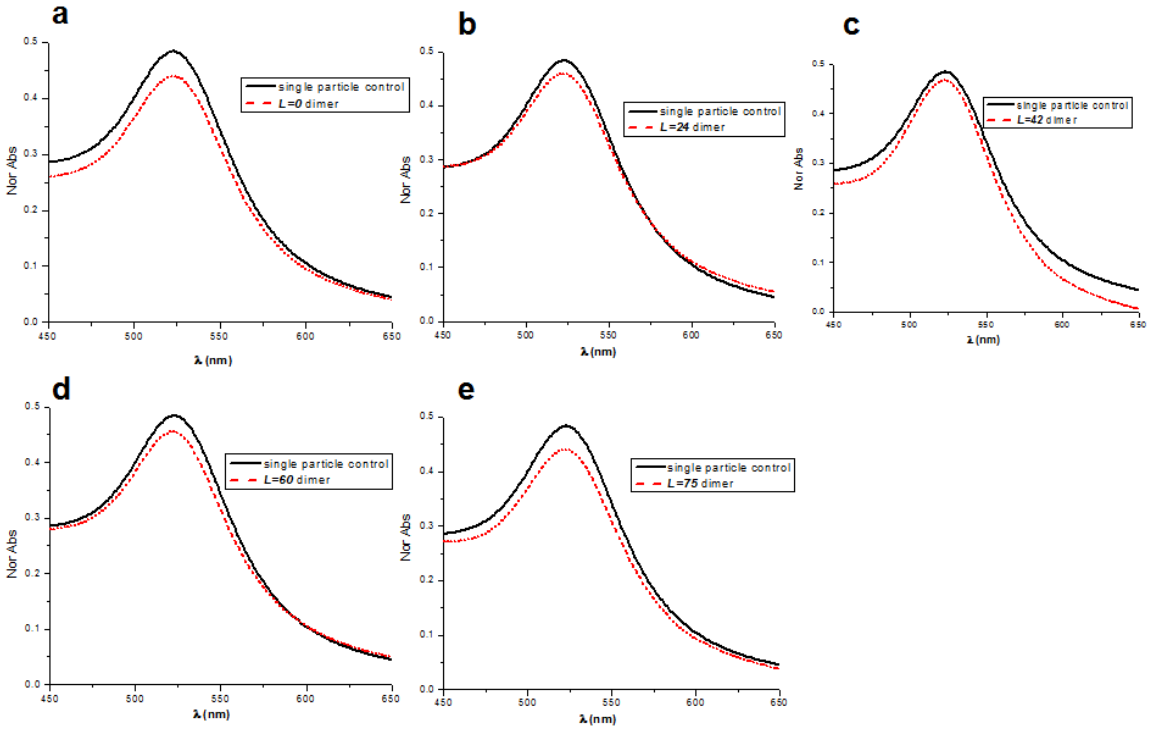

Figure 2.4. (a) Representative DLS profiles for the solutions of dimers linked by ***L***=0 and ***L***=75 bases. The number averaged hydrodynamic diameter, D_h, is obtained using a Malvern Zetasizer ZS instrument analysis software (b) Dependence of D_h on ***L*** at room temperature; the error bars are estimated from multiple measurements.

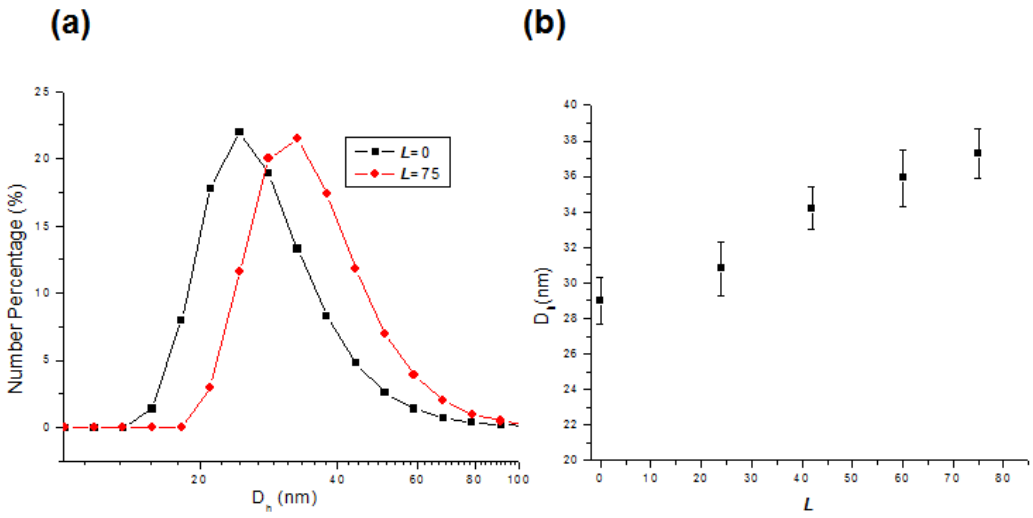

2.3 Computational Modeling

To aid in interpreting the experimental findings, we use a coarse-grained molecular model that mimics the experimental system. The model enables us to examine the molecular detail of the NPs connected by a various numbers of DNA strands as a function of the temperature. In this coarse-grained model, each DNA nucleotide consists of two force sites: one represents the sugar-phosphate backbone of a DNA nucleotide, and one carries the A/C/G/T identity of the nitrogenous base (sticky site) (Fig. 2.5). The model has been studied for a variety of systems, and details of the DNA potential can be found in Refs.,[45, 87, 100, 101] where it has been shown that the model captures the salient features of DNA driven-assembly. The core NP is represented by a single spherically-symmetric particle (red spheres in Fig.2.5). Here, each NP has a diameter ***d*** = 14.80 σ, where σ is the size of one nucleotide; distance can be mapped to

real units by $\sigma \approx 0.65$ nm (the typical spacing of ssDNA), yielding a NP diameter $d \approx 10$ nm, comparable to the experiments. However, we do not consider the model quantitatively predictive. Each NP has 30 ssDNA attached on its surface. Each ssDNA attached to the NP surface is formed by 16 bases. The outer 6 bases of each chain can hybridize with the linking ssDNA, which is of variable length.

In order to connect the dimers, we add free ssDNA (pink strands of Fig. 2.5) which, like in the experiments, consist of two regions: (i) a central region of variable length L, and (ii) ends that are complementary to the ssDNA attached to the NP. The linking region is 6 bases on each end, just like in the ssDNA attached to the NP. To mimic the experimental protocol in which only one hemisphere of the NP has linkers attached, we follow the procedure described in Fig. 3.3. This process can be summarized as follows: two DNA-coated NPs and four linkers (pink strands of Fig.2.5 (a)) are located at random positions. We randomly select four strands of each facing NP-NP hemisphere (Fig. 2.5 (b)), and hybridize the linkers with the chosen strands (Fig. 2.5 (c) and (d)). Once the hybridized dimer has formed, we allow the system to equilibrate and evolve without interference. We consider an ensemble of 50 choices for the linkages to evaluate average separations and end-to-end distances.

Figure 2.5. Simulation protocol for dimer formation of two DNA-coated NPs connected by four linkers. (a) Two DNA-coated NPs and four linkers (pink strands) are located at random positions. (b) Four strands of one hemisphere of each NP are randomly selected. (c) Hybridization occurs between the linkers and strands of the left NP. (d) Hybridization with second NP followed by equilibration.

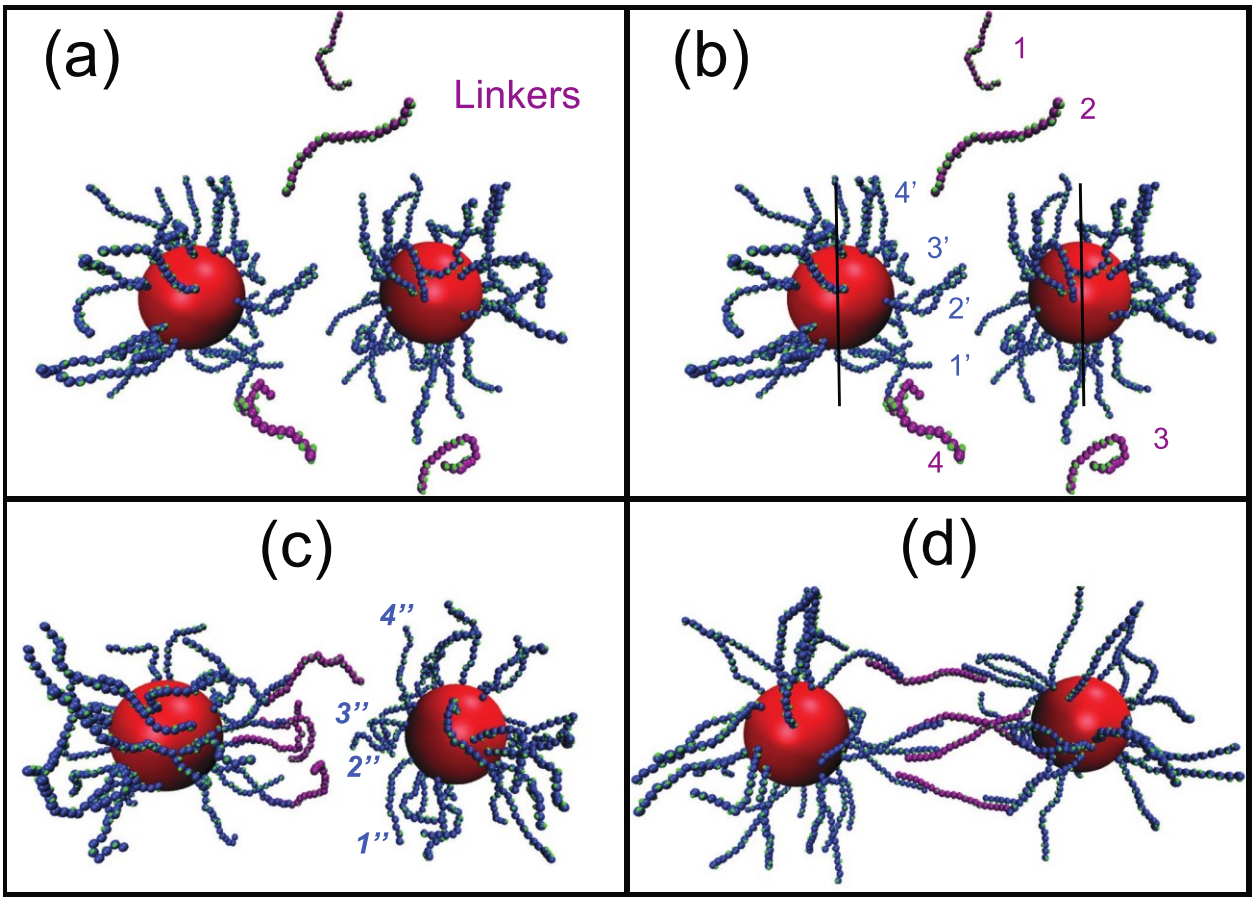

2.4 Results

2.4.1 Fully Bonded Dimers

We first examine the dependence of the dimer separation on the length ***L*** of the DNA linker using the DLS method at 26 ^{0}C, where DNA strands should be fully linked. The number-

averaged hydrodynamic diameter (D_h) corresponds to an average cluster size in the population, and, for the given particle system, it is indicative of the interparticle distances. We show the distributions of D_h for representative lengths $\boldsymbol{L}$=0 and $\boldsymbol{L}$=75 bases in Fig. 2.6 (a), which demonstrates a relatively homogeneous cluster population without the presence of large-scale aggregates. From the mean of these distributions, we probe the relationship between the average D_h and $\boldsymbol{L}$, as shown in Fig. 2.6 (b). We observe a monotonic, nearly linear growth, of D_h from 29 nm to 37 nm with increasing $\boldsymbol{L}$ from 0 to 75 bases. The DLS measurement probes an average hydrodynamic diameter of a dimer, which we can relate to the interparticle distance within a dimer using a model in which a dimer is approximated by an ellipsoidal object.[71] In this model, the shortest axis of the ellipsoid corresponds to the diameter of the particle combined with the ssDNA shell; the DLS measurements show this axis has a value of 20nm, independent of L. The longest axis relates to the sum of the particle diameters and the DNA linker. The model relates the observed change of D_h, from 29 nm to 37 nm, with an increase of interparticle distance (along the longer axis of the ellipsoid) from about 17 nm to 23 nm for Au particles with core of 11 nm and DNA shell thickness of about 7 nm. We obtain further internal structural details from SAXS measurements.

The *in-situ* SAXS method provides a direct probe of the internal cluster structure and allows for the determination of interparticle distances of dimers with sub-nanometer precision. The typical 2D scattering patterns from the dimer samples exhibit a faded ring (Fig. 2.6 (a) and (b)). We show the 1D scattering intensity profiles $\boldsymbol{I(q)}$, obtained from circularly averaging the 2D scattering patterns and the corresponding structure factors $\boldsymbol{S(q)}$ for studied systems in Fig. 2.6 (c) and 2.6 (d) respectively. The first $\boldsymbol{S(q)}$ peak monotonically shifts towards smaller wavevector values, $\boldsymbol{q}$, from 0.0276 $Å^{-1}$ to 0.0232 $Å^{-1}$ for a corresponding increase of $\boldsymbol{L}$ from 0 to 75 bases, as

determined from a Lorentzian fit. This clearly indicates an increase of the interparticle separation with increasing ***L***. The ***S(q)*** profiles of dimer clusters in the dilute solution can be described by a dumbbell model,[102]

$$S(q,D) = \frac{\sin(qD)}{2qD} + \frac{1}{2}, \qquad (2.1)$$

where ***D*** is the center-to-center nanoparticle distance. The surface-to-surface distance ***r*** ≈ ***D-d***, where ***d***=11nm is the diameter of the NP gold core.

Figure 2.6. Left panel (a and b). Representative 2D small-angle x-ray scattering patterns of dimers for ***L***=0 (a) and ***L***=75 (b). (c) Relative SAXS intensity, ***I(q)***, of dimer systems, as labeled in the inset. (d) The structure factors ***S(q)***, obtained as discussed in the method, for systems with corresponding colors shown in (c)**.**

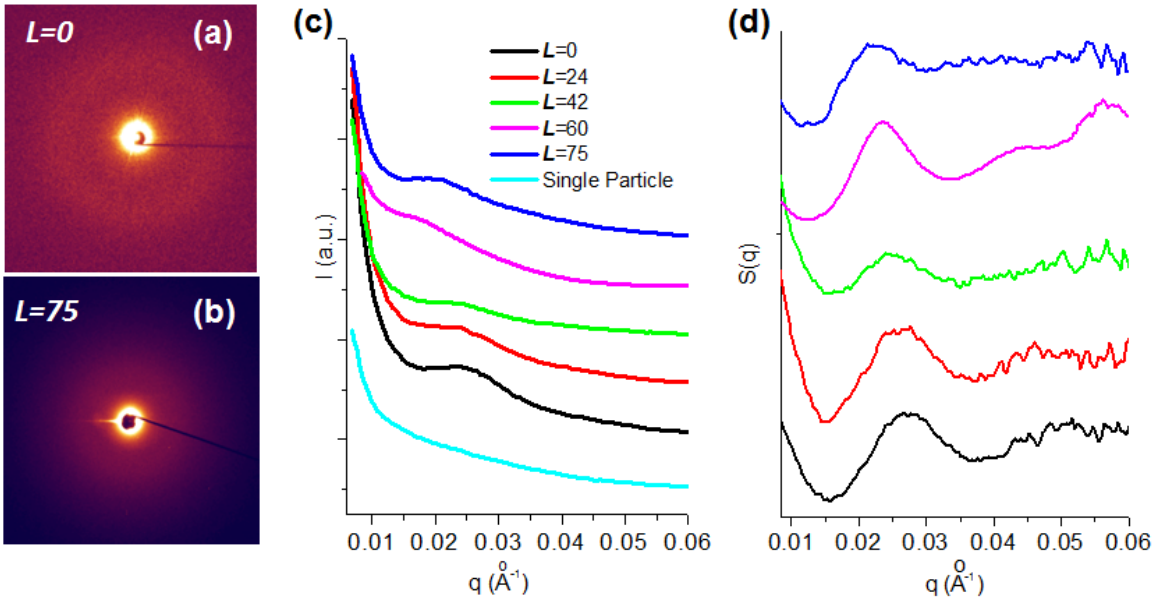

Fig. 2.7 shows the dependence of $\boldsymbol{r}$ on $\boldsymbol{L}$ for dimers linked with flexible ssDNA or rigid dsDNA connectors and compares the $\boldsymbol{r}$ values with those measured for ordered superlattices in which nanoparticles were linked with ssDNA motifs. For dsDNA connectors, we see an approximately linear growth of the interparticle separation $\boldsymbol{r}$ with increasing $\boldsymbol{L}$**.** While this behavior is expected when the dsDNA length is sufficiently less than the persistence length of dsDNA ($\boldsymbol{l_p} \approx 50$ nm),[103] our results indicates a linear regime even when the two lengths are comparable. This can be attributed to the DNA alignment due to multi-linker interactions. The observed slope corresponds to 0.24 nm per base pair which is consistent with the previously reported SAXS measurements of nanoclusters and 3D systems.[59] In contrast, the dimers assembled with ssDNA show much weaker dependence of the interparticle separation on the linker length due the greater linker flexibility. More puzzling is the observation that $\boldsymbol{r}$ is smaller (for the same $\boldsymbol{L}$) for the case of the dimers connected by ssDNA than for the superlattice system. We note that this deviation cannot be attributed to the difference in the salt concentration between those systems: 0.3M for superlattice and 0.1 M for dimers. In fact, the reduced salt concentration for dimer systems relative to 3D assemblies should *increase* (rather than decrease) the persistence length of ssDNA, and, correspondingly, increase the NP separations.

Figure 2.7. Surface-to-surface distance ***r*** as a function of linker length ***L***. Red, blue and black respectively correspond to dimers linked by dsDNA, dimers linked by ssDNA, and crystals linked by ssDNA. The symbols are data from the SAXS experiments. For dsDNA linked dimers, there is a linear relation between ***r*** and ***L***. For the ssDNA linked systems, the curves are from fits to the worm-chain model (Eq. 2), which yields for the crystal l_p=2.1 nm, and for the dimer l_p=0.33nm.

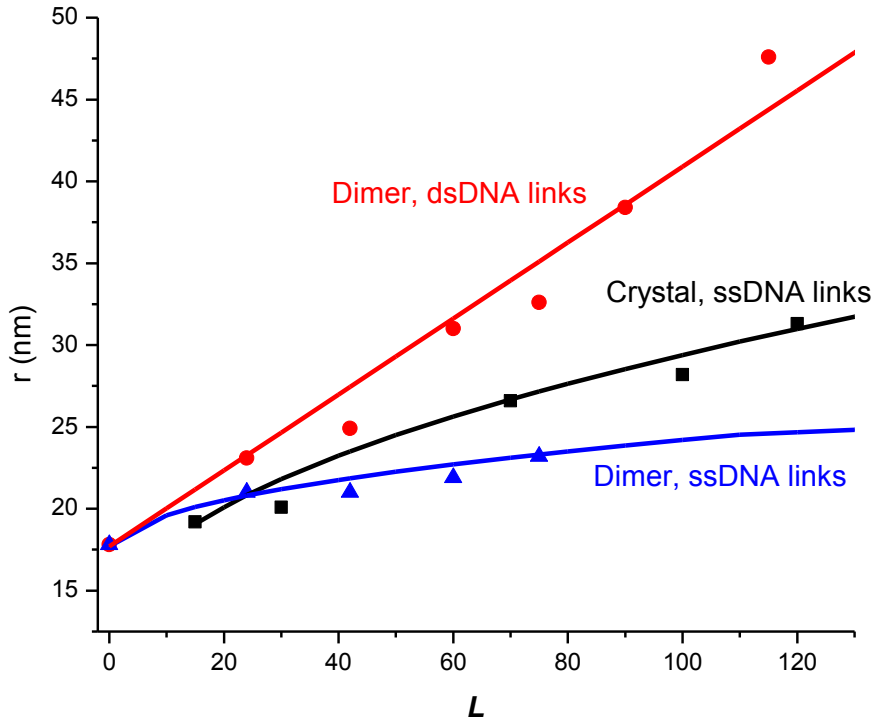

To understand the origin of the difference in separation of the dimers as compared to the superlattices, we consider the possibility that the geometry of linkages between NP may differ between the dimers and the superlattice. To do so, we utilize our simulations to study how the

interparticle distance changes when the NPs are connected by exactly one or four linkers. Fig. 2.8 shows the probability distribution function (PDF) of the surface-to-surface distance ***r*** of a dimer linked by one or four chains with ***L*** = 10 bases for the linker. The PDF (Fig. 2.8) shows that ***r*** is smaller (on average) when the NPs are connected by more than one linker. If all links were parallel to the dimer axis, we would expect little difference between the separation of 1 versus 4 linkers. That ***r*** is typically smaller with 4 linkers indicates that the geometry of links is more complex. If links cross each other, or occur closer to the poles, this will constrain the overall separation. The illustration of Fig. 2.8 compares typical geometries for 1 or 4 links, and contrasts short versus long separation for 4 links, demonstrating that separation is constrained by non-axial links.

Figure 2.8. The computed distribution of the surface-to-surface distance ***r*** for a dimer linked by either one or four chains for linker length ***L*** = 10 bases. The NP-NP separation is smaller when more than one linker connects the dimer. The insets show representative dimer configurations at corresponding linker numbers.

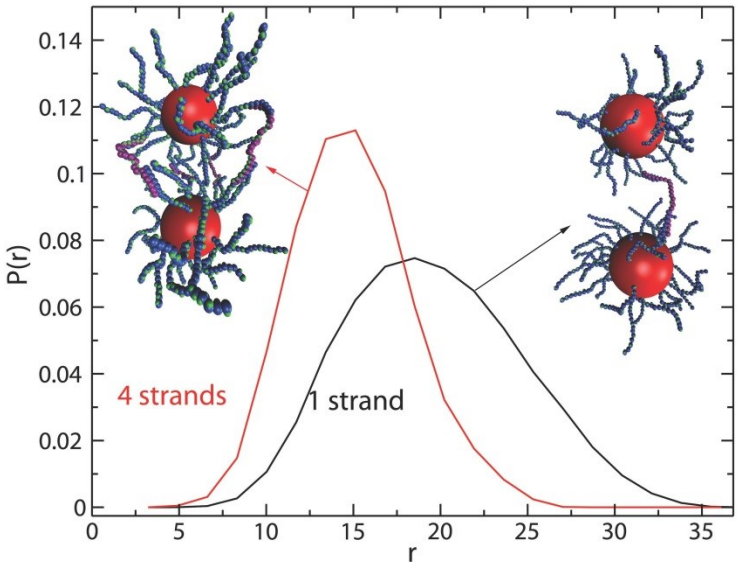

In short, the surface-to-surface distance is restricted by the linker with the shortest end-to-end distance, which is typically off the dimer axis. This finding can explain the difference between dimer and superlattice separations. For a NP in the BCC superlattice, the multibody interactions favor configurations where the linkers are distributed on a particle surface favoring particle-to-particle links that are localized in the $\pi/2$ solid angle between neighboring particles. As a consequence, almost all links lie along the axis of the interparticle separation in the superlattice. Such co-axial links will have a separation that is normally longer than off-axis links.

We next develop a theoretical description of how the separation varies with DNA linkage. Our previous experimental studies indicated that the worm-like chain model (WLC),[104] in which the end-to-end chain distance $\boldsymbol{R_e}$ is given by,

$$< R_e^2 >= 2L\, l_p - 2l_p^2\left(1 - e^{-\frac{L}{l_p}}\right), \tag{2.2}$$

describes reasonably well the $\boldsymbol{L}$ dependence of the nearest–neighbor interparticle distances of the superlattice for ssDNA linkers with a persistence length $\boldsymbol{l_p}$=2.1nm (Fig. 2.5). Motivated by this, we test whether our experiments for the dimer systems can be described in the same way. To do so, we need the end-to-end distance of the connecting ssDNA attached to the NP. We can approximate $\boldsymbol{R_e}$ by subtracting from the surface-to-surface distance 17.8 nm, which is the surface-to-surface distance of dimer linked by $\boldsymbol{L}$=0 connectors obtained from experimental measurement. Using Eq. (2.2), we find a surprisingly small value $\boldsymbol{l_p}$ =0.33nm (about half a base length of ssDNA) for the dimer systems. To rationalize this, we consider that the simulations have shown that the chains can be connected at points far from the axis between particle centers. As a consequence, using the interparticle separation systematically underestimates the end-to-end distances, resulting in an unphysically small value for $\boldsymbol{l_p}$.

We can quantitatively examine how interparticle separation underestimates R_e directly in simulations by comparing l_p evaluated from the actual R_e with that evaluated from the surface-to-surface distance r. Following the procedure used to analyze the experiments, we obtain a similarly unreasonably small l_p = 0.7 bases using r. In contrast, Fig. 2.7 shows the explicit calculation of R_e for L = 0, 10, 20, 30, 60 bases with either one or four linkers connecting NPs; for comparison, we also show a single free chain of ssDNA. The WLC model (Eq. (2.2)) describes the data well, with a physically reasonable persistence length that is larger than free DNA (l_p = 3.95 bases, or ≈2.5 nm) for NPs connected by 1 linker (l_{p1} = 5.74 bases), and by 4 linkers (l_{p4} = 4.86 bases). Thus the effect of being attached between the NPs slightly "stretches" the linking chain. Since we cannot access R_e in experiments, and the surface-to-surface separation r used in the WLC model gives unphysical values for l_p , we need to develop an improved description that can be verified from simulations and applied to the experiments.

Figure 2.9. Comparison of the computed end-to-end distance of free ssDNA (blue) with the ssDNA connecting the dimer via one linker (black) or four linkers (red). The curves are fits to the worm-chain model (eq. 2), which show that the effective persistence length relative to a free chain is larger for NP connected by one linker and smaller for NP connected by four linkers.

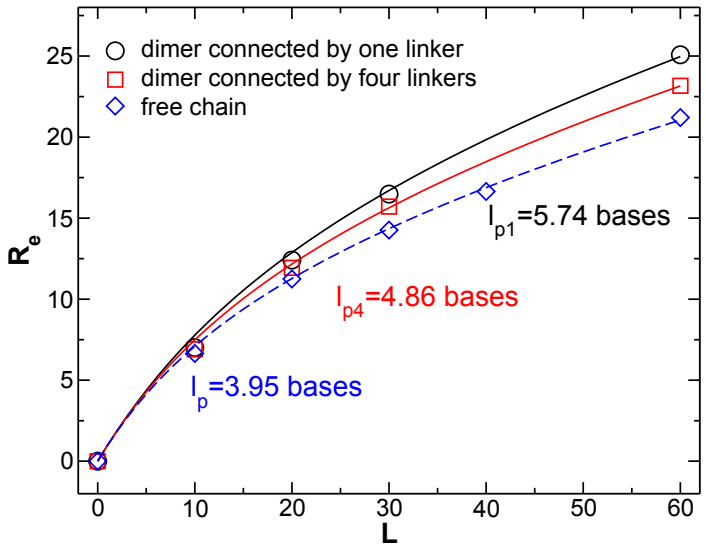

We propose a simple theoretical model that accounts for the effects of NP being linked by a combination of ssDNA and dsDNA regions, as well as multiple linkages. Consider a DNA bridge that connects the two DNA-grafted NPs that is formed by ssDNA regions ($\boldsymbol{L_{ss}}$ bases in total, with $\boldsymbol{L_{ss}} > \boldsymbol{l_p}$) and dsDNA regions (each region formed by $\boldsymbol{d_i}$ bp, with $\boldsymbol{d_i} < \boldsymbol{l_p^{dsDNA}}$). The mean square end-to-end distance $\langle R^2_{bridge} \rangle$ of such a DNA construct can be estimated by adding the end-to-end distances of each individual segment,

$$\langle R^2_{bridge} \rangle = 2 l_p L_{ss} + \sum_i d_i^2. \qquad (2.3)$$

In this expression, we approximate the ssDNA regions by the Gaussian model (since $\boldsymbol{L_{ss}} > \boldsymbol{l_p}$), and the dsDNA regions by the rigid–rod model (since $\boldsymbol{d_i} < \boldsymbol{l_p^{dsDNA}}$). We can approximate that

$\langle R^2_{bridge}\rangle^{½} \approx r$, the surface-to-surface separation for a single connecting strand. Figure 2.10 (a) shows that this simple model roughly describes the linking by a single chain in our numerical simulations. Note that the whole dependence on the linker length, including the initial separation at $\boldsymbol{L} = 0$, is calculated without any fitting parameters, assuming the same ssDNA persistence length $l_p = 3.95$ bases obtained from the simulations of the free ssDNA.

Figure 2.10. (a) The surface-to-surface separation ***r*** as a function of ***L*** for the dimer connected via one linker (black) or four linkers (red). The symbols represent the simulation data and the curves the theoretical model proposed in Eq (5). (b) The dependence of ***r*** on ***L*** from experiments at room temperature (26^{O}C) and before melting (35^{O}C); solid curves represent the function of ***r*** over ***L*** estimated from the analytical model with 1 (blue) and 4 (red) linkers in a dimer.

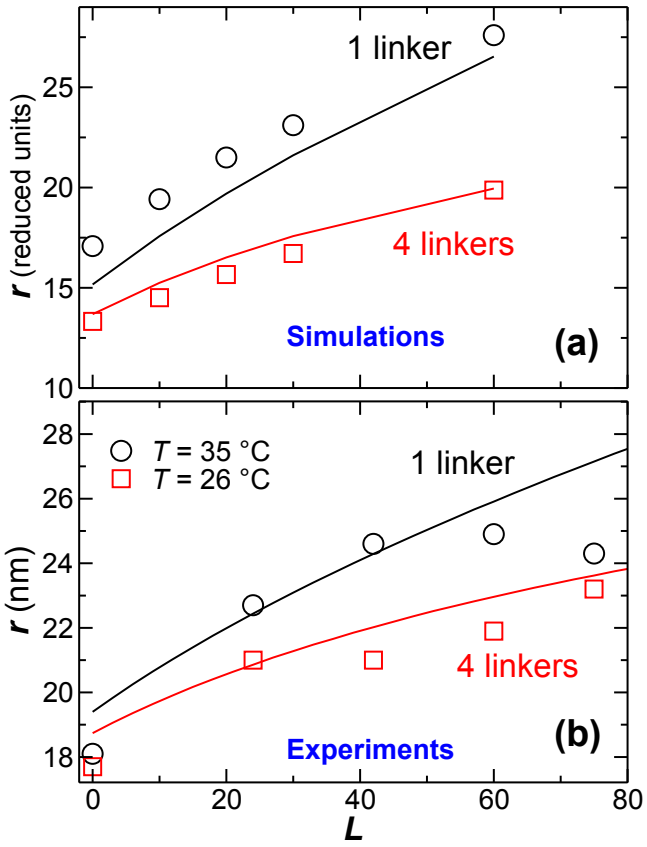

We next extend this model to account for multiple linkages. When the number of linkers increases, the competition for the binding sites, together with excluded volume effects result in greater distribution of the DNA connections over the NP surface. This effect leads to the following negative correction to the interparticle distance:

$$\Delta r = \frac{A_n + \Delta A_n}{\pi \mathrm{d}} = -(\mathrm{n}-1)\left(\frac{d}{N_0} + \frac{l_p L}{3\pi d}\right). \qquad (2.4)$$

Combining with Eq. 3, the resulting expression for the interparticle separation is

$$r = \sqrt{2 l_p L_{ss} + \sum_i d_i^2} - (\mathrm{n}-1)\left(\frac{d}{N_0} + \frac{l_p L}{3\pi d}\right). \qquad (2.5)$$

This correction captures the change in interparticle separation due to the multiple linkers observed in simulations (red curve in Fig. 2.8 (a)). Note that all the parameters are known, so no fit is involved.

A direct application of the same theory to experimental data does not give a satisfactory fit. However, we found that the experimental data for fully linked dimers (4 links) can be successfully described (Fig. 2.8 (b)) after a minor modification of the model:

$$r = \sqrt{2 l_p L_{ss}} + \sum_i d_i - (\mathrm{n}-1)\left(\frac{d}{N_0} + \frac{l_p L}{3\pi d}\right). \qquad (2.6)$$

Here, the first term represents the root-mean-square size of the ssDNA part of the bridge, the second term is the total contour length of the dsDNA segments, and the last term is the multi-bridge correction, Eq. (4). Physically, this variation of the model corresponds to the presence of a modest stretching force that is strong enough to orient dsDNA segments, but not too strong to significantly stretch the ssDNA fragments of the chain. As a result, dsDNA segments are aligned along the dimer axis, rather than randomly oriented as assumed in Eq. (2.5). The experimental

data sufficiently below the melting temperature is well described using this approach for a physically plausible l_p, from $2nm$ to $2.5\ nm$. The experimental data to test the effect of the number of linkers will be presented when we discuss the temperature dependence.

The theoretical model, Eq. (2.6), also works for more complicated systems, such as dimers connected with combined linkers. In this design, the linker is composed of two strands of ssDNA terminated by mutually complementary 15-base segments (as shown in Fig. 2.11(a)). This design allows for a longer interparticle separation. We observed that for the 15 bp double-stranded part that is between of the two single–stranded chains, the dimer separation increases by about 5nm, which is well captured by our theoretical model (Fig. 2.11(b)).

Figure 2.11. (a) Design of two studied systems: (system 1) dimers fabricated using a single stranded linker, and (system II) dimers fabricated using a combined linker. (b) Surface-to-surface distance ***r*** as a function of linker length ***L***. For the system II, ***L***=***M***+***N.*** Red curves represent the function of ***r*** over ***L*** for corresponding systems estimated from theoretical model at n=4, l_p=2.2nm.

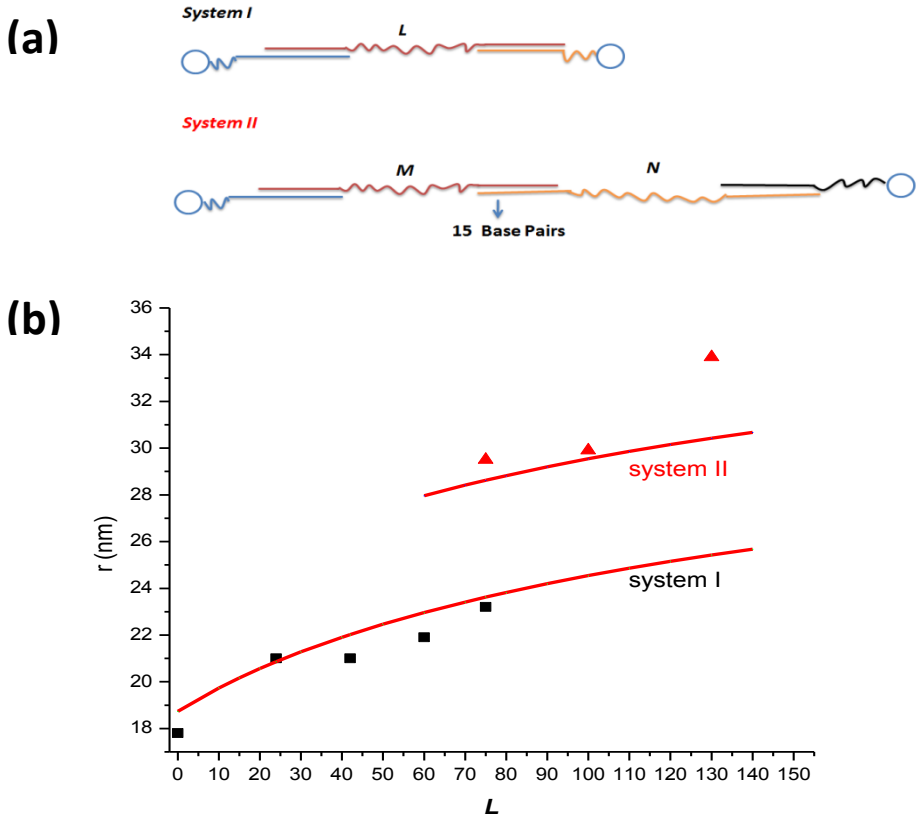

2.4.2 Temperature Dependence of Dimer Separation

We next examine the temperature ***T*** dependence of dimer separation *via* the SAXS technique. We perform a gradual heating of the systems from 26 ^{o}C to 31 ^{o}C, 33 ^{o}C 35^{o}C, 37 ^{o}C and 40 ^{o}C. Fig. 2.15 (a) shows the ***T*** dependence on ***r*** obtained by fitting the data using Eq. (2.1). All systems exhibit a modest increase of ***r*** with increasing ***T***.[105] However, the relatively large error bars do not allow us to compare a change of separations with temperature as a function of ***L***. At the same time, a SAXS monitoring of dimer melting reveals that for shorter linkers melting occurs at a slightly higher ***T***, with disassembly of ***L***=0 dimers at 40 ^{o}C (Figure 2.12, 2.13 and 2.14), which can be attributed to higher local density of DNA. The observed ***r*** increase exceeds that expected from the T-dependence of the DNA persistence length, which should only change slightly. To understand the origin of the increase of ***r(T)*** found experimentally, we examine our molecular simulations.

Figure 2.12. The change of the DLS measured hydrodynamic diameter (D_h) before (T=26 ^{o}C) and after a DNA melting (T=40^{o}C) indicate a dimer disassembly for experimental systems.

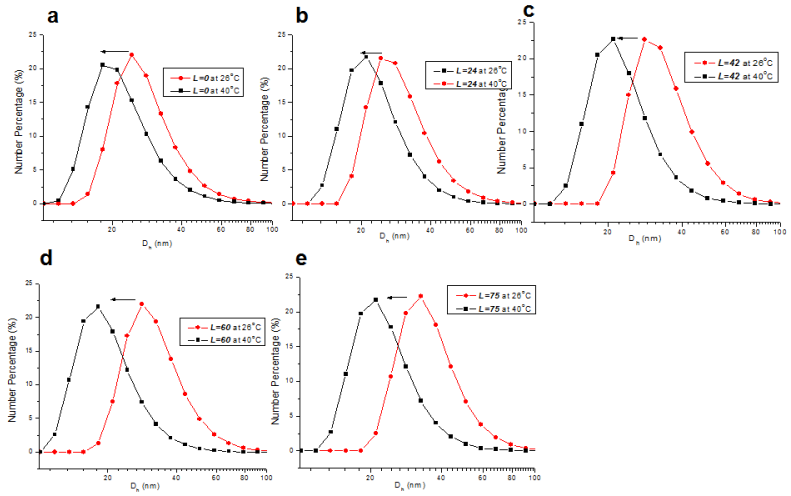

Figure 2.13. Temperature dependent D_h for corresponding linkers as shown; the data were obtained from DLS measurements. The number-averaged size of clusters depends on change of: a population of dimers (decreases during melting of dimers) and interparticle distances (increase with temperature). Overall, the first factor plays a more significant role in D_h change with temperature.

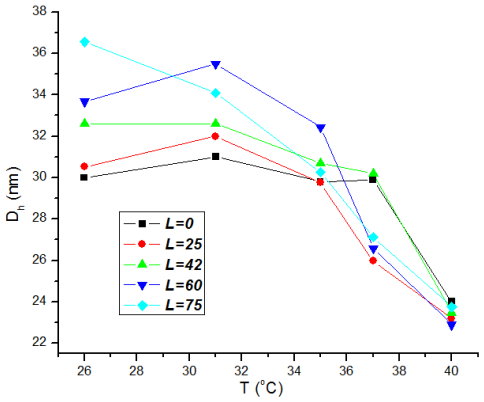

Figure 2.14. The comparison of SAXS patterns for different systems of dimers (***L=0*** (**a**), ***L=24***(**b**), ***L=42***(**c**), ***L=60***(**d**) and ***L=75***(**e**)) at the room temperature (26°C) and after melting (40°C). The structure factors were obtained as discussed in the text.

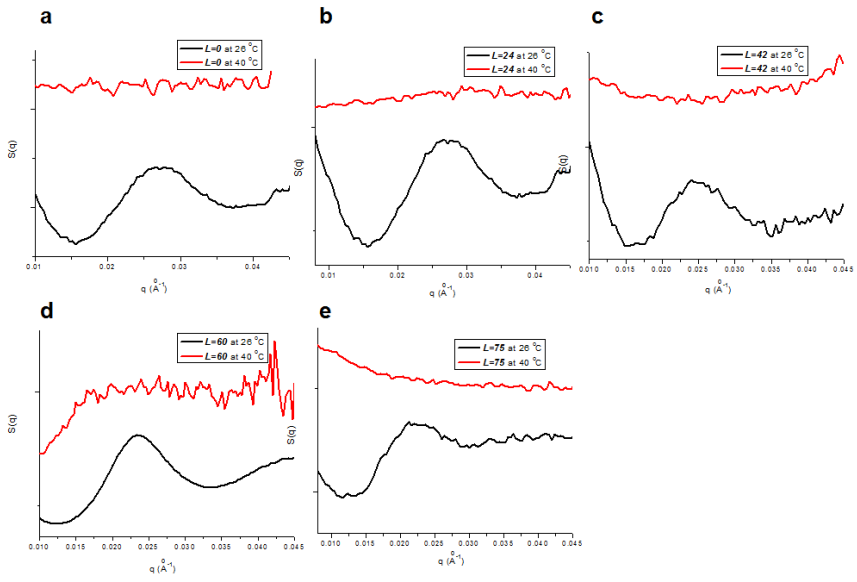

Figure 2.15. Surface-to-surface separation ***r*** as a function of temperature for various ***L*** from experiments (a) and simulations (b). The uncertainties of experiments are estimated from multiple measurements and SAXS peak fitting. Like the experiments, the interparticle distance increases with increasing ***T***. (c) Average number of linkers $\langle n_L \rangle$ connecting NP as a function of ***T*** from simulations, demonstrating that the change in ***r*** is caused by the reducing number of connecting linkers.

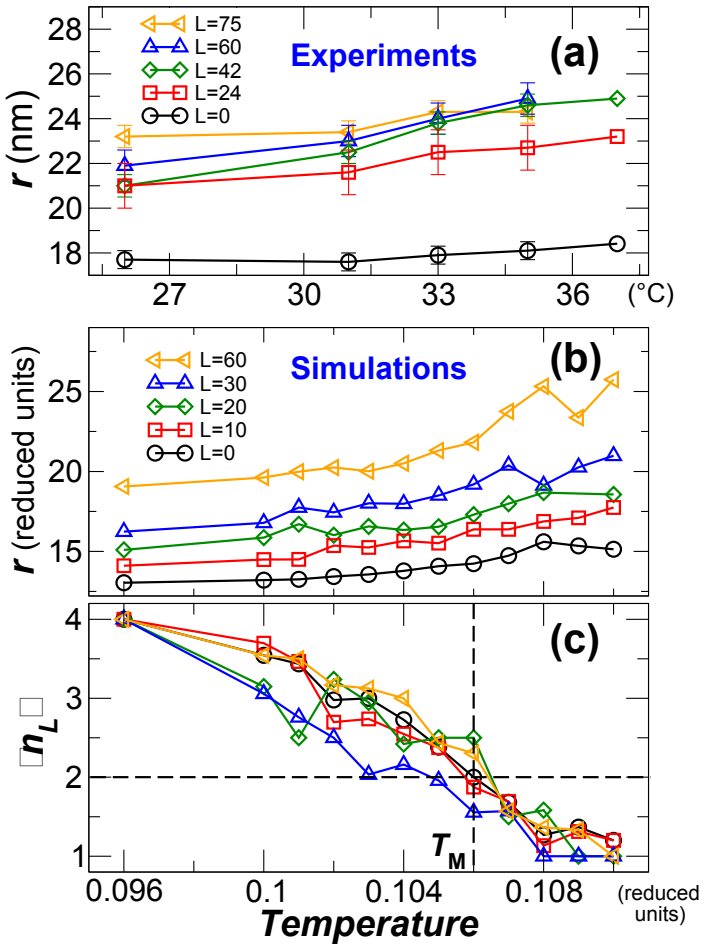

Following the experimental protocol, in the simulations we increase the temperature of dimers connected by four linkers from ***T***=0.096 (fully connected DNA) to a final temperature ***T***=0.120 where the dimers are melted. Fig 2.15 (b) shows ***r*** as for this range of ***T***. Like the experiments,

we find an increase in r when T increases, consistent with Fig. 2.15 (a). To explain this trend, we directly examine the number of links between the dimers in the simulations. We plot the average number of linkers $\langle n_L \rangle$ that connect the dimer in the simulations as a function of the temperature in Fig. 2.15 (c). We find that $\langle n_L \rangle$ decreases with increasing T. As previously shown in Fig. 2.8, when there are more connected linkers, the separation is dominated by the shortest link. Hence, the loss of linkers on increasing T results in increased r. This inter-relation is directly seen by plotting parametrically the dimer separation r as a function of $\langle n_L \rangle$ (Fig. 2.11). In doing so, we eliminate the explicit T dependence of the separation, and consequently can test the theoretical model proposed in Eq. (2.5), generalizing the expression to non-integer values of the number of linkers. Fig. 2.16 shows excellent agreement between the simulation data and the theoretical predictions (without any adjustable parameters). This verifies the predicted dependence on the number of linkers.

Figure 2.16. Surface-to-surface separation r as a parametric function of the mean number of links $\langle n_L \rangle$. The symbols represent the data and the lines the theoretical model proposed in Eq. (5).

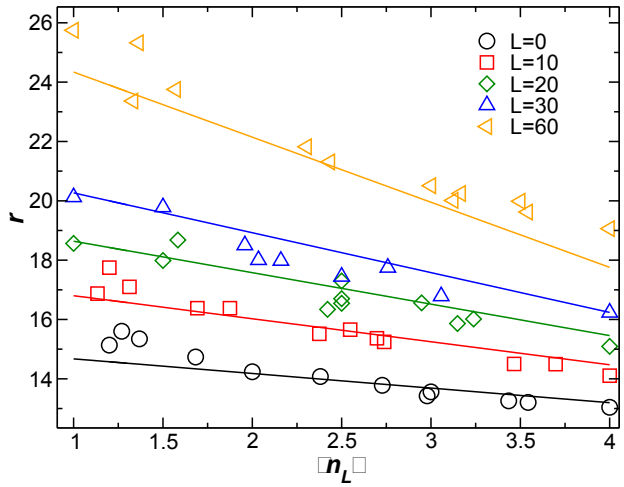

Since we now know that increasing temperature has the effect of decreasing the number of links, we can use experimental data from relatively low or high temperature as a way to test the predictions of the model for dimers connected by single or multiple linkers (Eq. (2.6)), respectively. As shown in Fig. 2.8(b), the measured ***r(T)*** for all systems is within bounds determined from the analytical model for a single linker connection (n=1) and four-linker connections (n=4). Near the melting point, the number of linkers per dimer decreases, and the interparticle separation should approach the $n = 1$ value just before dimer melting occurs.

2.5 Conclusion

We utilized synchrotron-based small-angle x-ray scattering to characterize the interparticle distance of a dimer of gold nanoparticles linked with DNA chains and interpreted the results with the aid of molecular modeling, leading to the development of an analytical description. We showed that, in the regime when nanoparticles and DNA chains are comparable in size, the separation distance between the two NPs is directly related to the number of links connecting NPs. In the regime when particles and links are comparable in size, the location of links can significantly deviate from the axis between the particles. As a result, the intradimer separation is constrained by off-axis links that yield smaller NP separation than expected for a single chain connecting NP. We combine these observations in a theoretical model that describes both our numerical and experimental data. The effect of temperature is thus understood as a consequence of changing the mean number of links between NPs. Our findings might play an important role in designing novel materials based on nanoparticles and polymers.

2.6 Methods

The fabrication procedure of dimers is shown in Figure 2.1. The first particle, Au_1, was functionalized with a mixture of two types of DNA, denoted as DNA_1 and DNA_1N. These two types of DNA serve the purposes of (i) recognition to surface grafted DNA (DNA_1NS) and (ii) for the consequent attachment of linkers (DNA_L) respectively. Au_1 were deposited on surface functionalized with DNA_1NS due to 15 bases complementary of DNA_1NS and DNA_1N. Following the deposition of the first particle layer, a fourfold excess of linkers DNA_L relatively to surface-attached particles Au_1 was added in order to hybridize with DNA_1 through 15-complementarity bases. At the third step, particles Au_2, functionalized with one type of DNA only (denoted as DNA_2), which is complementary to 3'-end of linker DNA_L, were added in a ratio 1:1 relative to Au_1. This resulted in a formation of surface immobilized dimers due to the hybridization of linkers between Au_1 and Au_2 particles which are linked by 4 DNA_L on average. Finally, the assembled dimers were released from the surface using a liberating strand (DNA_F) which has a higher affinity to the surface-grafted DNA_1NS than DNA_1N, due to 18- complementarity bases. Consequently, particles were dispersed in the 0.1 M PBS (10nM phosphate buffer, 0.1M NaCl pH=7.1).

Materials: 11 nm gold nanoparticles were synthesized as reported.[80] ssDNA strands (shown in the table S1) were obtained from Integrated DNA Technologies Inc. (Coralville, IA). The DNA were HPLC purified. Before nanoparticle functionalization, the disulfide oligonucleotides were first reduced by dissolving the lyophilized samples (100~300 nmoles) in 0.3 mL of a 100 mM dithiothreitol (DTT) solution in purified water or buffer. The reduced DNAs were loaded onto a freshly purified sephadex column (G-25, Amersham Bioscience) and eluted with 2.5 mL10 mM phosphate buffer (pH = 7.4). The DNA was quantified using UV-Vis analysis with the specific

DNA's extinction coefficient.

Functionalization of Au Nanoparticle: Gold particles Au_1 were functionalized with DNA_1 and DNA_1N, Au_2 particles were functionalized with DNA_2 following the literature reported protocol.[82] Briefly, gold nanoparticles were modified with alkanethiol oligonucleotide by adding oligonucleotide to an aqueous nanoparticle solution (particle concentration~20nM) up to a final concentration of 6μM. After 24h, the solution was buffered at pH 7.2 (10nM phosphate), and NaCl solution was added gradually. The concentration of NaCl was increased step by step, arriving at a final concentration of 0.2M. Excess reagents were removed by centrifugation for 90 min at 7000rpm. The gold nanoparticles were washed with 0.2M PBS buffer and subjected to successive rounds of centrifugation and resuspension. The nanoparticles were finally resuspended in the fresh 0.2M PBS solution.

Dimer Fabrication: Dimers were fabricated following the literature reported method.[71] The reactions took place at 0.1M PBS buffer (10mM phosphate buffer, 0.1 M NaCl, pH=7.1). Streptavidin-functionalized magnetic beads (Pierce Biotechnology Inc) were modified with the biotin-modified single stranded DNA DNA_1NS by incubating magnetic beads in the high concentration of the DNA_1NS solutions for about 1 hour. At the first step, 75μL of the magnetic beads (MBs) was added to the 5nM 500 μL Au_1 solution. The solution was incubated for about two hours allowing for absorption of Au_1 to MBs. A suspension was removed and the MBs were rinsed 3 times. In the second step, 250μL solution containing 4× linkers (*L*) excess over nanoparticles was added. After 3 hours incubation, the suspension was removed, and magnetic beads were rinsed. In the third step, Au_2 particles were added at a 1:1 ratio to the Au_1 particles absorbed on the surface incubated for 3 hours. The magnetic beads were separated and rinsed. At the last step, strands DNA_F (×1000) were added to release the dimers from MBs to a fresh 250μL buffer solution. The dimers were characterized by UV-Vis spectroscopy, Transmission Electron Microscopy (TEM), Dynamic Light Scattering Measurement (DLS) and Small Angle X-Ray

Scattering Measurements (SAXS). In the second system, shown in Figure 8, a combined linker $\boldsymbol{L=L_M+L_N}$ was used to connected gold nanoparticles. The linker was prepared by mixing $\boldsymbol{L_M}$ and $\boldsymbol{L_N}$ in a 1:1 ratio first. Other steps included the same procedures as discussed above.

Table 2.1 The ssDNA strands used in this study.

ssDNA	Sequence (5' to 3')
DNA_1N	ATT GGA TTG GAA GTA TTT TTT TTT TTT TTT-C_6H_{12}-SH
DNA_1NS	CTT GTG TCT ACT TCC AAT CCA ATT TTT TTT TTT TTT TT- Biotin
DNA_1	TTC TCT ACA CTG TCT TTT TTT TTT TTT TTT-C_6H_{12}-SH
$\boldsymbol{L}$	AGA CAG TGT AGA GAA $(T)_l$ ATT GTT ATT AGG
DNA_2	HS-C_6H_{12}-TTT TTT TTT TTT TTT TAG CCT AAT AAC AAT
DNA_F	ATT GGA TTG GAA GTA GAC ACA AG
$\boldsymbol{L_M}$	AGA CAG TGT AGA GAA $(T)_M$ ATT GTT ATT AGG CTA
$\boldsymbol{L_N}$	TAG CCT CAT AAC ACT $(T)_N$ TAG CCT AAT AAC AAT

Charactrization

Dynamic Light Scattering Measurement: DLS measurements have been performed on a Malvern Zetasizer ZS instrument. The instrument is equipped with a 633 nm laser source and a backscattering detector at 173°. The measurements were carried out at the temperatures as indicated on the figures S4. The dimers were dispersed in the 0.1M PBS solution.

Small Angle X-Ray Scattering Measurements: The SAXS experiments were performed at the National Synchrotron Light Source (NSLS) X-9 beamline. The samples were placed in quartz

capillary tubes with a home-built temperature controller. The scattering data was collected with a CCD area detector. The scattering vector q is defined as $q = 4\pi/\lambda(\sin\theta/2)$, where λ is the wavelength of X-ray, 0.8856 Å, θ is the scattering angle. The scattering vector q is calibrated by using silver behenate ($q = 0.1076$ Å^{-1}).

The SAXS measurements provide information on the structure factor ***S(q)*** of clusters in a solution. The 1D intensity profiles, *I(q)*, were obtained by an azimuthally integration of the 2D SAXS pattern. The background corrected intensity can be represented in a simple form $I(\boldsymbol{q}) = \boldsymbol{S}(\boldsymbol{q})\boldsymbol{F}(\boldsymbol{q})$, where *F(q)* is the form factor of free particles measured from the solution containing the equimolar mixture of free particles. The center-to-center distances between gold nanoparticles within the dimer were obtained from *S(q)* by accounting for the size of individual AuNP determined from the separate TEM and SAXS measurements. SAXS measurements were conducted for the samples in 0.1 M PBS buffer placed in a 1mm quartz capillary over the temperature range 26 ^{o}C to 40 ^{o}C with 20 seconds exposure time.

UV-Visible Spectrophotometry (UV-vis): UV-vis spectra were collected on a Perkin-Elmer Lambda 35 spectrometer (200-1100 nm).

Transmission Electron Microscopy (TEM): TEM micrographs were collected on a JEOL-1200 microscope operated at 120 kV. The samples were prepared by a drop casting aqueous solution of nanoparticles or dimers onto a carbon coated copper grid, followed by the slow removal of excess solution with filter paper after 5 minutes.

Chapter 3

Reaction Pathway Dependence of Fabrication Self-limited Dimer

3.1 Introduction

Binding DNA-coated nanoparticles with linker DNA strands has advantages over the direct hybridization system, as it is easy to control the number of connections and assembly kinetics. [55, 56] A previous study has successfully demonstrated how to use a DNA linker system to build crystal structures. It is interesting to notice that the crystalline behavior only happens in a medium range of number of linkers and length of linkers, while the other regimes are either amorphous aggregates or clusters.[55] For example, our previous work reported the transition from a disordered amorphous state to a crystalline bcc phase, which was determined by linker length of ssDNA and number of linkers. With the increase of linker length, the boundary of the crystal phase and amorphous phase shifts to a higher linker ratio. No crystalline phenomena was observed when linker spacer number L <24 or L>150. The same effect is also reported by Mirkin et al, who used DNA duplex linkers to connect nanoparticles.[59] The reason that long linkers lead to the cluster structure and the internal structure of cluster is still unclear. One possible reason for this occurrence might be that, when the linker is long, the aggregation of the NPs is kinetically hindered. However, more structure information is required to study this question in detail.

In Chapter 2, we examine the internal structure of the nanoparticle dimers made from a step-wise surface-encoding method by a combination of scattering experiments and molecular simulations. In this structure, the linkage DNAs connect the facing hemisphere of the nanoparticles. We find that, for a given DNA length, the interparticle separation within the dimer is controlled primarily by the number of linking DNA. Especially for the flexible ssDNA, the interparticle distance of the DNA dimers is constrained by the shortest DNA linkages between these two particles, with the impact becoming more significant in the long-linker regime.[57] Extended from this study, we connected the DNA-functionalized nanoparticles with various DNA linkers with no restriction on connection positions, and examine how flexible linkages influence the self-assembly process of nanoparticles and their internal structure.

In this chapter, we systematically discussed the system linked by various lengths of single stranded DNA linkers. We found that when a significantly long linker is applied, the system leads to dimers. We further studied the evolution of their structure as a function of linker length and preparation methods using Synchrotron-based X-ray scattering. We reveal a self-limited behavior of nanoclusters in which the long linker connects the opposing hemisphere of the nanoparticles and limits the growth of the nanoclusters. The findings explained why the system fails to form an aggregation/crystal structure, and demonstrated a simple way to fabricate a high yield of nanoclusters.

3.2 Experimental Design

Three different pathways were applied to connect two types of DNA-functionalized particles by the same number of DNA linkages (Figure 3.1). N represents the ratio of DNA linkages to the number of one type of the particles. In the first pathway, two types of particles were attached to

an equal number of linkers first. After incubation for several hours, the two particles were mixed together. In the second pathway, all the linkers were attached to one type of the particle first and then mixed with the other type of particle. In the third pathway, the particles and linkers were mixed together all at once. The third pathway leads to a lot of random states. It introduced the complexity which not only contains the mixture states of the first two pathways, but also contains other mixture states with various numbers of ssDNA linkers attached. Therefore, in this study, we mainly focus on the first two pathways.

Figure 3.1. Schematic illustration of particle-particle connections with DNA linkers of length L (a) and 3 different pathways to mix these three components (b).

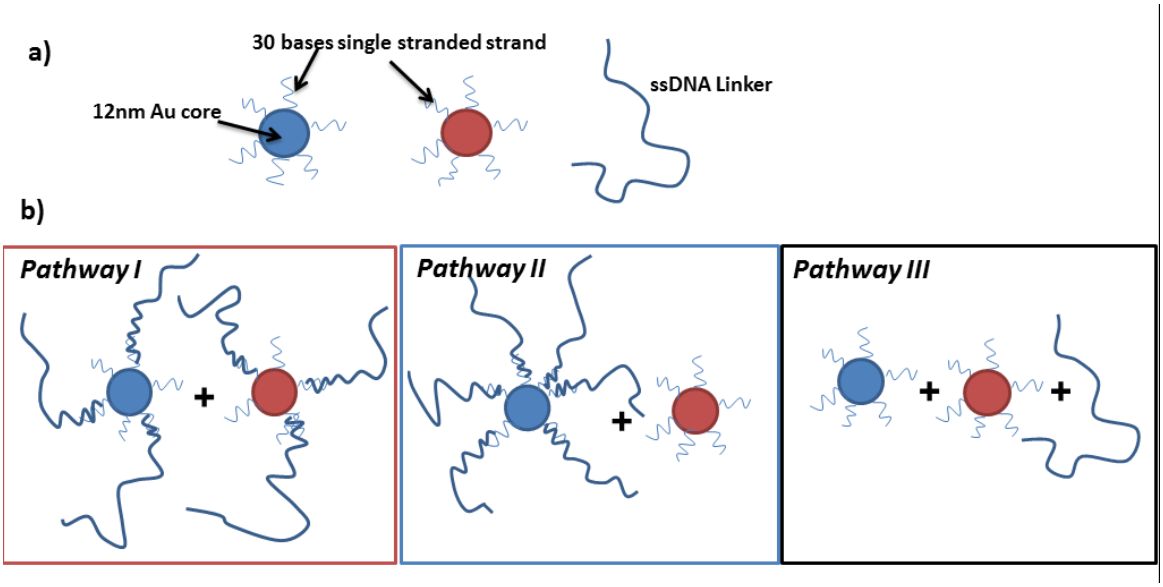

The experimental details are as follows: 12nm nanoparticles were first functionalized with two types of 30-base ssDNA: DNA_1 and DNA_2 as shown in Table 1, respectively. Then, those two types of particles were connected by various lengths and ratios of ssDNA linkers, which contain 15 bases complementary to DNA_1 and DNA_2 on each end. The number of bases in the spacers

has been denoted as *L* in bases which varied from 0 to 165 (eg, 0, 24, 42, 60, 75, 100, 125, 150, 165). N varied from 5 to 36.

By changing the mixing sequences of linkers and reactant particles, one would be able to tune the kinetic pathway of the particles, and eventually change the formation process of the assembled structure. In the first pathway, the steric repulsion between two types of particles is higher than pathway II, due to the stronger repulsion of polymer linkage due to the equal distribution on two particles. Also, the length of the linker in bases (L) and number of linkers connected (N) also have significant impact on the structure. Here, the assembled structure was investigated as a function of *N*, *L,* and assembly pathways.

3.3 Results and Discussion

3.3.1 Phase Diagram of the Assembled Structure

Dynamic light scattering (DLS) has been conducted to study the association process of nanoparticles in-situ, in a time-dependent manner by tracking the hydrodynamic diameter (D*h*) of the clusters/aggregates in the solution. For example, in figure 3.2a, we demonstrate the size of clusters as a function of reaction time by using two pathways in the presence of linker L=150 bases, with linker ratio N=10 at 33^{o}C. For both pathways, the formation kinetics shows a similar trend; the size of the clusters increase fast in the first 50 minutes from 22nm to around 57 nm, which indicates the formation of finite-sized clusters. Later, D*h* achieves a plateau and stabilizes afterwards, indicating that these clusters are stable without further growth. In contrast, for short linkers (L=25) prepared by pathway I (shown in Figure 3.2b), D*h* keeps increasing until the aggregates precipitate, which is consistent with our previously reported experiments. [55]

We further examined the morphology of the clusters formed by L=150, N=10 using pathway I as dried by scanning electron microscopy (SEM). Indeed, we observed that the majority were small clusters (shown in Figure 3.2c), or dimers. We did the statistics by counting more than 200 nanoparticles, and found that the number percentage of the nanoparticles that formed dimers is around 60% (as shown in Figure 3.2d and Figure 3.3). The percentage of clusters containing more than 3 particles is less than 7%. Both the SEM and DLS data confirmed the clusters are stable in the presence of long linkers. The D*h* of clusters obtained using linker L=150 is significantly higher than the D*h* of dimers obtained from short linkers (around 36nm as described in Chapter 2) which is attributed to the large gyration radius of DNA linkage L=150.

Figure 3.2. a) DLS-based time-dependent association profiles for 15 nM of single particles connected with ssDNA linker L=150 at linker-to-particle ratio N=10, obtained from pathway I (shown in red) and Pathway II (shown in blue) ; b) Comparison of the association profiles obtained from short linker (L25) and long linker (L150) by pathway I in the same conditions. c) Representative SEM obtained from pathway I in the presence of linker L=150, d) The statistics histograms based on counting number of particles in SEM images.

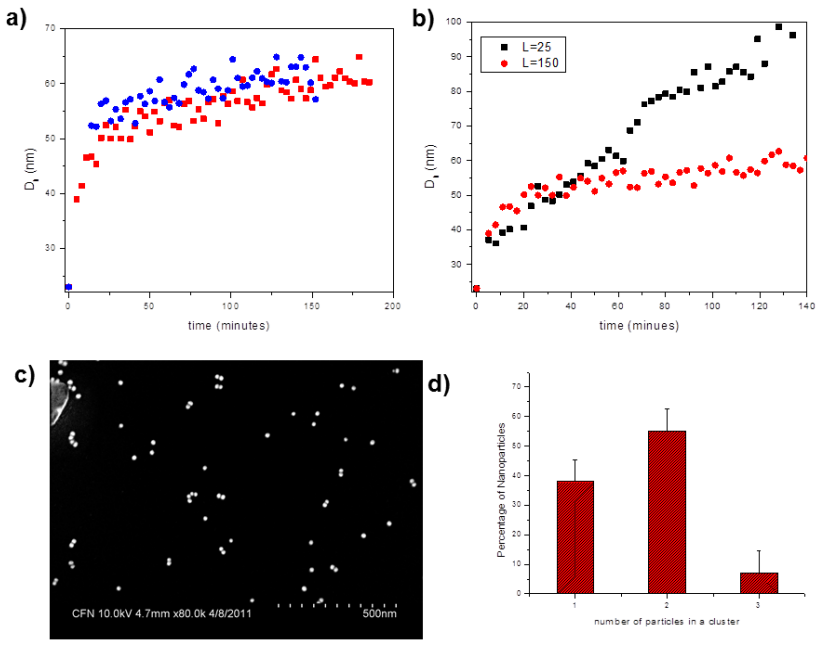

Figure 3.3. Typical SEM images of the self-limited structure fabricated using pathway I. There are a small poulation of the dimers with large interparticle distances as circled below.

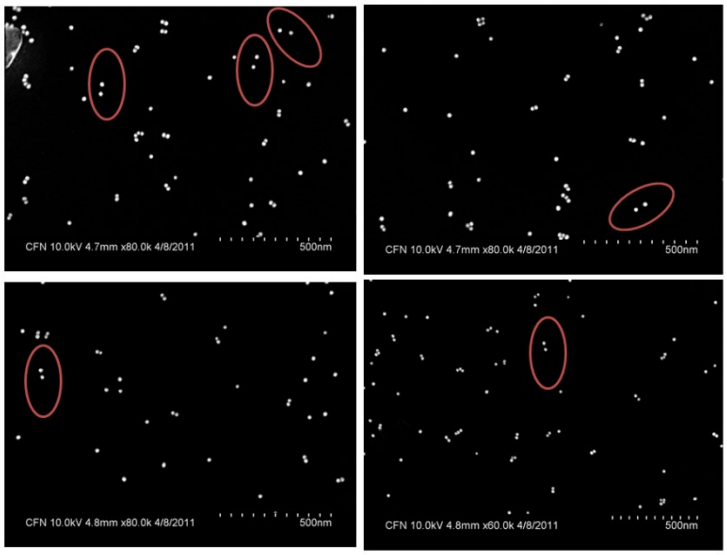

Figure 3.4. State diagram of aggregates *vs* clusters prepared by pathway I and pathway II. Circles represent the formation of aggregates, while triangles represent the formation of clusters.

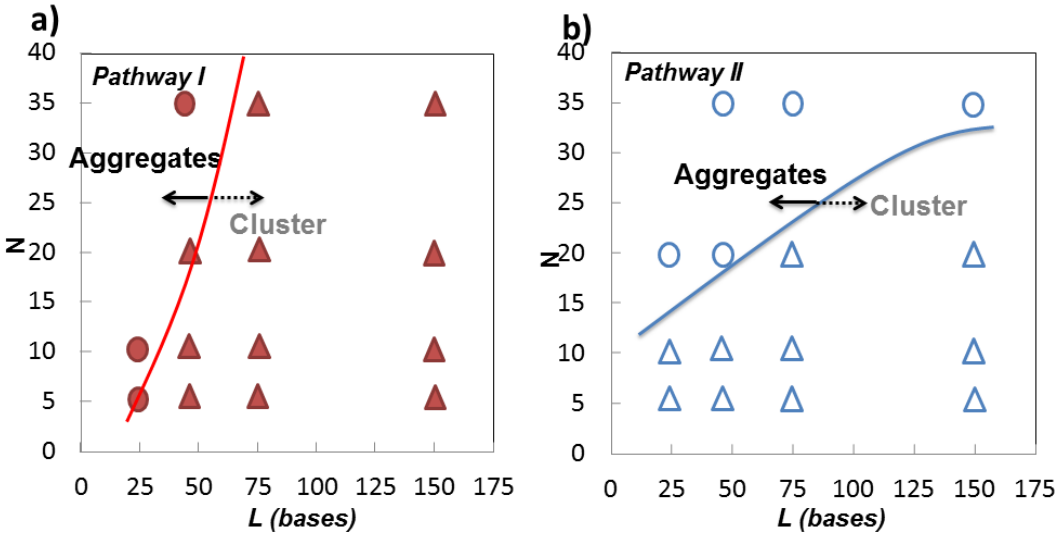

By tracking the particle assembly process in different pathways with DLS methods, the state diagram of aggregates vs clusters has been plotted as a function of L and N (shown in Figure3.4). The aggregates and clusters are defined by DLS, as shown in Figure 3.2b: if D*h* reaches a significant plateau, the assembled product was considered as a cluster. In contrast, if D*h* keeps increasing with time, the assembled product is treated as aggregates. The boundary of aggregates and clusters is plotted based on the guided of eyes. The particle concentration was fixed to 15nM in this study. The reaction is taken place at 33^{o}C.

Interestingly, we found different pathways lead to different boundaries between aggregates and cluster phase. For pathway I, the key factor determining phase diagram is linker length. The cluster regime emerged at a long linker area (when L>75) (Figure 3.4a). For pathway II, the number of linkers also plays a very important role in cluster formation. The cluster regime is located at low N regime (Figure 3.4b). For example, in pathway I, when linker length L=25 was

applied, we observed an aggregate formation at N=5. The boundary between aggregates and clusters appear at linker length L=75; no aggregates were observed when linker length L>75. For pathway II, the aggregates emerged at N>10 even for the short linker L=24. As the linker length increased, the number of linkers needed to form an aggregate is increased. However, the increased slope is much shallower than that for Pathway I. Different from pathway I, aggregation can still obtained at long linker regime as long as linker number is enough. For example, aggregation was obtained in the presence of L=150 at 45^{o}C.

3.3.2 Internal Structure of Assembled Clusters

We further examined the internal structure of the clusters obtained from both pathways by small-angle X-ray scattering. The *in-situ* SAXS method provides a direct probe of the internal cluster structure and allows for the determination of interparticle distances of dimers with sub-nanometer precision. The SAXS experiment was performed as described in the previous chapter. Figure 3.5a and b shows the representative 2D patterns which correspond to the cluster formed by ssDNA connector L=150 using pathway I (b) and pathway II (a), respectively.

Both patterns exhibit a faded ring, which is consistent with the dimers' typical scattering patterns. The position of the rings corresponds to the peak of the 1D S(q) curve, and essentially related to the interparticle distance of the dimers. Those representative 2D patterns indicate that the interparticle distance of dimer clusters prepared by pathway I is significantly shorter than it is for the dimer cluster prepared by pathway II.

Figure 3.5. Left panel (a and b). Representative 2D small-angle x-ray scattering patterns of dimers for pathway II (a), and pathway I (b). Right panel (c) surface-to-surface distance ***r*** as a

function of linker length ***L*** for different pathways (II shown in blue, I shown in red) at **N=10.** The inset cartoon shows the possible internal structure estimated from ***r.***

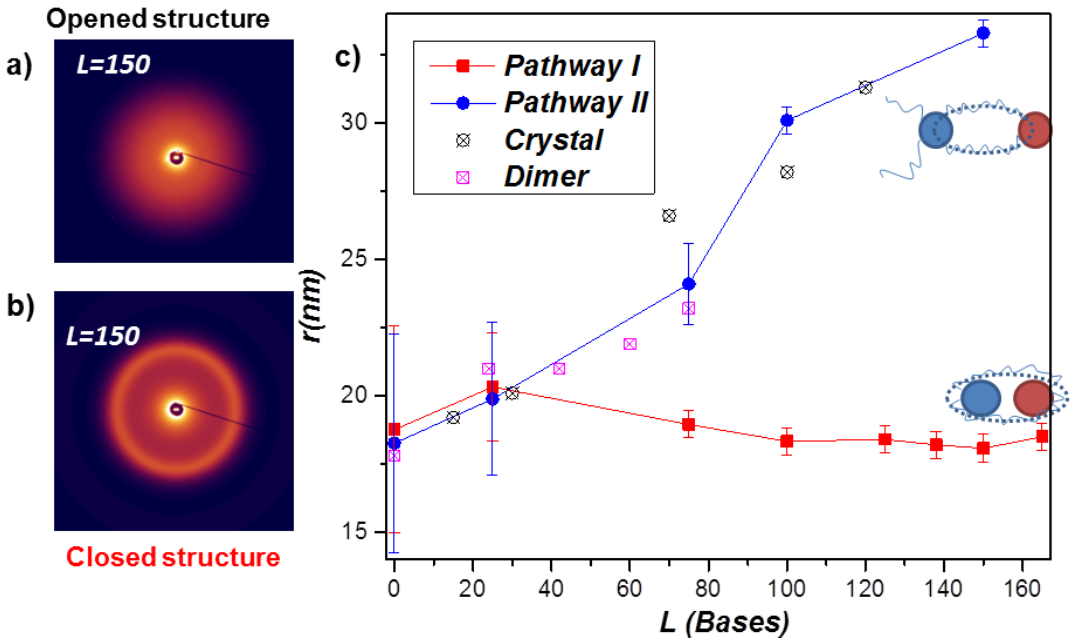

Figure 3.5c shows the dependence of the interparticle distance of r as a function of L for two different pathways. The interparticle distance r is extracted from their corresponding 1D structure factor using a Dumbbell model.[102] Due to the aggregation of nanoparticles in the presence of short linkers (L=0 and L=24), the dumbbell model is not applicable, and the error bar of data fitting is calculated based on the difference between the data obtained from the Dumbbell model and r=2π/q. We see an increase of r as a function of L for pathway II from r=22 at L=0 to r=33nm at L=150. We compared the interparticle distance of this structure to the data that we obtained from crystal structures and dimers built from a step-wise method. The interparticle distances r obtained from pathway II exhibit a similar trend with this two cases when increasing L. In contrast, we observed a complete deviation of r for pathway I: r slightly decrease from

22nm at L=24 to 18nm at L=75, then reaches a plateau at r=18nm through the rest of our studied regime (until L=165).

Those two trends suggest two different internal structures of obtained clusters from these 2 pathways. For clusters obtained by pathway I, when increasing the ssDNA linker, the linkers connect the nanoparticles from the opposite side of the particles, forming a "close structure" in which the interparticle distance is mainly restricted by the shell thickness of DNA, exhibiting a plateau (shown as Figure 3.5 inset). This "close structure" limits the growth of the clusters, and eventually leads to a stabilized cluster state.

For pathway II, particles are connected by linkers at the facing hemisphere and exhibit an "open structure". The interparticle distance is mainly dependent on the linker length. Although the structure allows for the growth of the clusters, the small recognition cross-section of particles prohibited the aggregation kinetically. By increasing the number of linkers and reaction temperature, aggregates will be still obtained.

The self-limited behavior has further been confirmed by optical measurement of quantum dot (QD) and gold nanoparticle nanoclusters linked by various lengths of the linkers (Figure3.6a). For example, 10nm AuNPs were connected to QD ,with emission at 535nm using pathway I in the presence of L150. The lifetime of the quantum dots in self-limited clusters decreased from14.8ns for the control samples (including the same concentration free quantum dots and gold nanoparticles in the absence of DNA linkages) to 10s, while the lifetime of quantum dots in nanoclusters linked by L0 is 12.3ns (Figure 3.6c). The results indicate that the distance between QD and Au nanoparticles linked by L150 is shorter than it is for L0, which leads to the quenching of the fluorescence signal of QD and a shorter lifetime.

Figure 3.6. Lifetime of DNA-regulated self-limited quantum dots and gold dimers linked by L=0 (blue) and L=150 (red). The control sample is the mixture of quantum dots and gold nanoparticles in the absence of linkers. The proposed internal structures of dimers are shown inset.

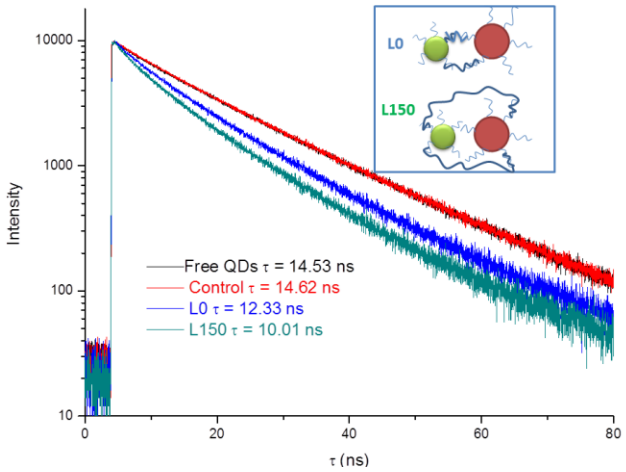

3.3.3 Mechanism of Interparticle Reactions

The mechanism of the reactions can be explained as follows: for pathway I, when short linkers were applied (Figure 3.7a), the system acts as the typical direct hybridization system of two types of DNA-functionalized nanoparticles. Aggregates form fast in the presence of low numbers of the DNA linkages.[50, 52] In contrast, when long linkers were applied (shown in Figure 3.7b), the large hydrodynamic radius of linker-covered nanoparticles yields to a much slower diffusion rate than it does for nanoparticles with short DNA shells. Along with strong steric repulsions between the particles, the reaction kinetics is slow. When two DNA nanoparticles diffused together, the possibility of collision with a third particle in a short period of time is small. Therefore, all of the linkages will be consumed between these two particles. The structure tends to take the configuration with the least steric repulsion from linkers. The first couple of linkers connected to the opposite hemisphere of the particles. The collective effect of these linkages

leads to an interparticle distance constrained by the shortest linkage, which is close to the shell-thickness of the particles.

For pathway II, when small ratios of short linkers were applied (Figure 7c), linkers on the center particle surface can be easily occupied with the second type of particles and eventually leads to small clusters. In contrast, for the long linker case as shown in Figure 3.7d, when linker attached to one of the particle first, the other end of linker has more flexibility to grab DNA strands on the surface of other particles at any random positions at first one or two connection. However, as soon as a couple of interactions formed with this nearest neighbor particle , the interaction between these two particles become less favorable due to a much larger entropy penalty for extra connection. Nanoparticles formed an intermediate "open dimer" containing free linkers available for further hybridization. When connections were made between two types of particles, another particle with a short DNA shell can grab the linkers from the other end and form aggregates (Figure 3.7d). However this process is very slow due to the small cross-section.

Figure 3.7. Illustration of reaction mechanisms for pathway I (a, b) and pathway II(c,d).

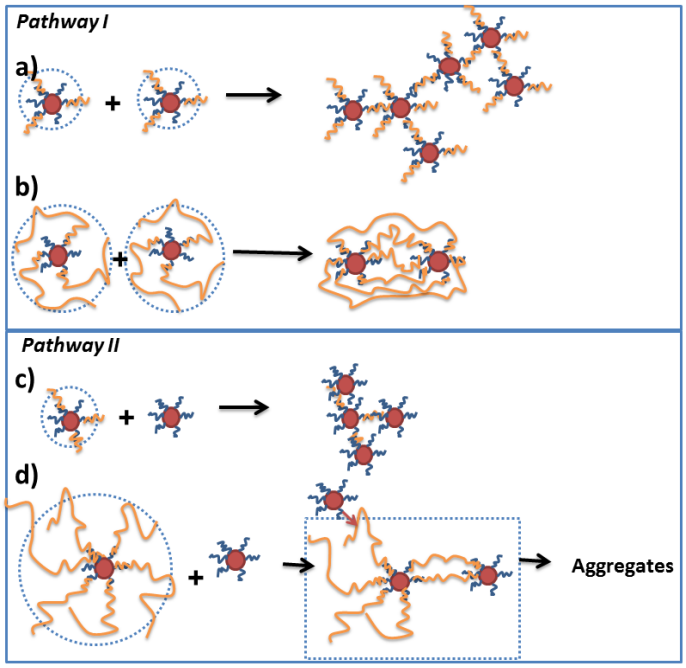

3.4 Conclusion

We explored the self-assembly process of nanoparticles in the presence of various lengths of linkers with low linker/nanoparticle ratios. We found the formation of a high yield of small nanocluster (mostly dimers) in the long linker regime (when L>75). The Small Angle X-ray Scattering experiment suggested two types of structures of the dimers: one is an open structure with ssDNA linkages connecting the facing hemisphere of the particles, exhibiting an increasing interparticle distance with increasing linker length; the other is a "close structure" with DNA linkers connecting to opposite hemispheres of the nanoparticles. This structure inhibited the growth of nanoparticles, with the interparticle distance decreasing to the shell-thickness of the nanoparticles. This finding explains why the crystal structure cannot form in the long linker regime, and demonstrates a simple method to fabricate dimer nanoclusters.

3.5 Method

Two types of 12nm nanoparticles were first functionalized with the DNA listed below in the following Table, in which n varied from 0 to 165. Then those two types of nanoparticles were mixed with various lengths of the linker strand by different pathways as mentioned in the text. The reaction is taken place at 33^{o}C.

Table 3.1. DNA ssDNA strands used in this study

DNA_1	TTC TCT ACA CTG TCT TTT TTT TTT TTT TTT-C_6H_{12}-SH
L	AGA CAG TGT AGA GAA (T)n ATT GTT ATT AGG
DNA_2	HS-C_6H_{12}-TTT TTT TTT TTT TTT TAG CCT AAT AAC AAT

As mentioned in the previous chapter, we applied synchrotron-based SAXS measurements (beamline X9 at the National Synchrotron Light Source) to probe an internal dimer structure. The 2D scattering data were collected with a charge-coupled device area detector (MAR CCD) at wavelength λ=0.8856 Å. The SAXS measurements provide information on the structure factor *S(q)* of clusters in a solution. SAXS measurements were conducted for the samples in 0.2 M PBS buffer, placed in a 1mm quartz capillary over the temperature range 26 ^{o}C to 40 ^{o}C with 20 seconds exposure time.

Dynamic Light Scattering Measurement: DLS measurements have been performed on a Malvern Zetasizer ZS instrument. The instrument is equipped with a 633 nm laser source and a backscattering detector at 173^{o}.

Chapter 4

DNA Driven Interaction of Asymmetric Nanoclusters with Surface and in Bulk

4.1. Introduction

Self-assembly of asymmetric units is an increasingly popular topic for building materials by a bottom-up approach.[106] The asymmetric colloidal particles can be fabricated by the surface-based method, in which the surface breaks the symmetry of particles' functionalization and gives rise to asymmetric particles (Janus nanoparticles) and clusters (such as heterogeneous dimers). The asymmetric property allows aligning the particle in a designed way a with specific orientation, and yields a series of structure from small clusters to 1D, 2D and 3D structures.[107-117] Janus particles with both hemispheres functionalized with two chemical compositions is a promising subunit to build colloidal clusters. The attraction force and repulsion force between Janus particles can be generated by grafting polymers with different properties, such as hydrophilic/hydrophobic force. The balance of these attraction and repulsion forces can be tailored by patch area and reaction conditions, such as salt concentration and pH, which will eventually yield various assembled structures.[115] For example, Chen et.al reported the formation of a Kagome structure using patchy particles with hydrophilic parts in two poles and hydrophobic parts in the middle. Also, the assembly kinetics are critical to the self-assembly of

asymmetric structures. For example, the colloidal cluster intermediate with a long life time can fuse into a highly-ordered non-equilibrium structure which has been reported recently.[116]

Compared to the micro-sized colloidal particles, the size of the nanoparticle is in the regime of a polymer shell, therefore, the geometry of the particle and the polymer distribution on the nanoparticles might have a more complicated impact on their self-assembly process than it does for the colloidal particle. Understanding how this asymmetric geometry influences the self-assembly process is essential to build complex clusters and hierarchical structures, as well as to explore their corresponding applications.

The recognition behavior between the DNA-encoded nanoclusters and recognizable surface has been systematically investigated. DNA serves as a "smart polymer", which provides the selective, reversible, and programmable connection to bind nanoparticles, while at the same time the polymer nature of DNA results in a repulsion force between nano-objects. The balance of these interactions leads to interesting recognition behaviors. Moreover, the assembly process of DNA-functionalized micro-sized colloidal particles has been systematically studied, and a few quantitative models have been established to interpret the experimental results, which provide us further insight to create corresponding models in the nanoparticle systems.[50, 52, 118] The interpretation of these recognition processes allows for developing various applications of DNA-encoded surfaces, for example, to separate DNA-functionalized nanoclusters with different geometries and encoded DNA strands.

Here, we have investigated several types of nano-objects interacting with DNA-functionalized surfaces: spherical particles, asymmetrically functionalized particles such as Janus particles, and the simplest asymmetric nanocluster containing two particles, dimers. The single-stranded DNAs immobilized on the surfaces are complementary to DNA grafted on one of cluster

particles or on a side of the Janus particle. The recognition processes were tracked by UV-vis in a time-based manner, which measures the intensity decrease of the surface plasmon band of gold nanoparticles. The following questions are addressed in this work: 1. How does the distribution of DNA strands on the nano-objects influence their assembly process? 2. How the system design parameters affect this recognition process. Furthermore, based on these discoveries, we developed two strategies to separate nanoclusters via a DNA-grafted surface.

4.2. **Recognition of Asymmetric Nanoclusters by DNA functionalized surfaces**

Figure 4.1. The simplified scheme presents the recognition of single particle, Janus Particle and dimers on the corresponding encoded surface.

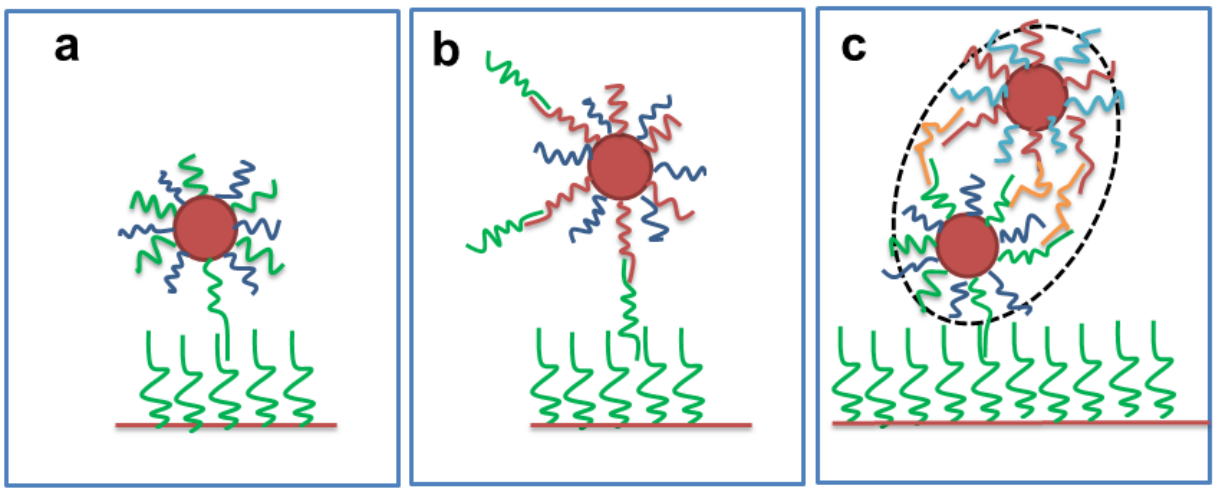

The three systems that were studied were symmetric single particles, Janus particles, and dimers, as illustrated in Scheme 4.1. The spherical single particle is an 11nm particle capping with the composition of two types of 30-base single-stranded DNAs: DNA_C (Figure 4.1a shown in green), which provided complementary recognition between the particle and surface via a 15 base-pair (bp) duplex formation and noncomlementary strands DNA_N1 (shown as blue). For each particle, there are more than 50 DNA strands equally distributed on the particle surface.

Both dimers and Janus particles were fabricated by a step-wise surface-based method followed by reference [71]. In particular, the Janus particle is fabricated with a single particle functionalized with strands DNA_N1 (Figure 4.1b, shown as red) and DNA_N2 (Figure 4.1b, shown as blue), which are noncomplementary to the strands on the surface . A linker (DNA_l_Janus, Figure 4.1b shown as green) was attached on one hemisphere. This linker bound the particle by a 15-base complementary with an overhanging part containing the other 15 bases of DNA, which provides complementary recognition to the solid surface. A dimer is composed of two 11nm gold nanoparticles (AuNP) connected by a ssDNA linker. One of the particles, Au_1, was functionalized with a mixture of DNA_1N (blue) and DNA_C (green), which is the same as the symmetric single particle control, while the other particle, Au_2, was capping with two uncomplimentary strands DNA_N2 and DNA_N3. Linker strands DNA-L binds the two Au particles via 15-base complementary nucleotides located at the DNA-L ends to DNA_1(red) and DNA_N2 (light blue) correspondingly.

We used the DNA_C'-encoded streptavidin-coated magnetic microparticles as the recognizable surfaces. The advantage of using this type of surface is that it can be easily separated from solution in a magnetic field, which provides a convenient way to characterize reactions by looking at the concentration of the nanoparticles/nanoclusters in the supernatant. Moreover, streptavidin-coated microparticles allow for a highly-immobilized oligonucleotide density on the surface. To prepare those particles, we incubated the magnetic particles with different concentrations of biotinlated DNA; the DNA density grafted on the surface of microparticles can be tailored from 1% to 100% saturation, which allows us to study a wide range of DNA densities on the surface. The density of immobilized oligoneucleotides has been roughly evaluated by the area a DNA has occupied using the number of DNA functionalized on the surface divided by the

surface area of the particles, in which we assumed that the surfaces are smooth and the magnetic particles are perfectly spherical. For the 100% saturated surface, the estimated density of DNA is about 8.3 pmol/cm^2, (calculated from the 4800 biotin/per mg of streptavidin-modified magnetic beads with 1% solids) which corresponds to numbers of DNA per unit square: 5×10^{13} / cm^2, about 0.5 ssDNA /nm^2 . The DNA density on the surface was tailored from 5% to 100% saturated, corresponding to the DNA density from 0.025/nm^2 to 0.5/nm^2 . The recognition behavior of the nanoclusters to the surface was probed by the UV-visible spectrophotometer (UV-Vis). UV-vis probes the surface plasmon (SP) resonance band, the intensity of which is proportional to the nanocluster's concentration in the solution.

Figure 4.2 (a) The scheme illustrates the experiment design as an example of single particle absorption. Representative UV-vis spectrum of single particles (b) and asymmetrically functionalized dimer (c) measured from supernatant at different incubation time.

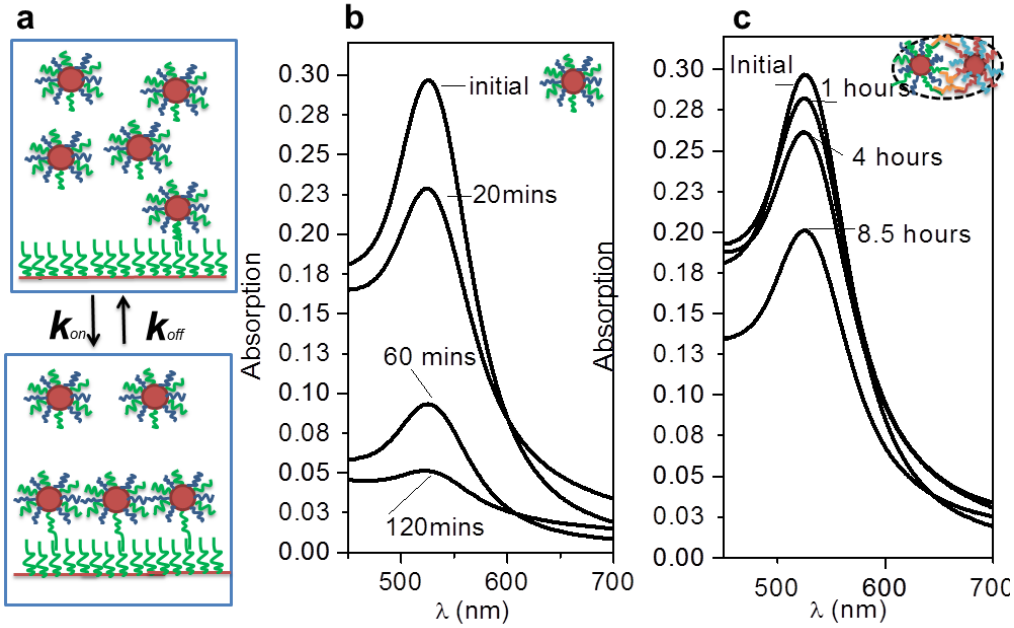

The intensity of these surface plasmon bands, at 519nm for this particular size of the Au nanoparticle is proportional to the cluster's concentration remaining in the solution. The experimental illustration is shown in Figure 4.2 using single particle and dimer as an example: The micro-sized magnetic particles grafted with corresponding single-stranded DNA were mixed with a single particle and dimer solution, respectively. After a few hours of incubation, the color of the solution varied from pink to light pink, which indicates the recognition of single particles/dimers on the surface. After removing the surface supported by magnetic field, the concentration of the supernatant is quantitatively determined by UV-vis spectrum.

Figure 4.2b and c show a series of representative spectra of single particles and dimer supernatants at different incubation times. For the single particles, the peak of surface plasmon (SP) quickly decreased from 0.3 to 0.04 in 2 hours indicates the fast absorption of the single particles. While for dimers, the first hour assembly reveals the peak of the SP band decreased from 0.3 to 0.285. It indicates that 95% of the particles remain in the solution and only 5% of the dimers were recognized by the surface in an hour. The extinction peak of the supernatant decreased to 0.27 in 4 hours, and decreased to 0.215 in 8 hours, indicating that more than 70% of the dimers remains in the solution instead of being recognized by the surface. The remaining particle fraction was defined as Φ , which is calculated by dividing the absorption peak intensity at various measuring times by the initial plasmonic peak intensity. The reaction is started with 3nM of nanoclusters (or particles) in order to keep a consistent kinetic measurement. By extracting Φ from that spectrum and plotting it as a function of time, one is able to understand the recognition kinetics of each system. For further analysis, we define k_{on} as the kinetic constant of this recognition, and k_{off} as the kinetic constant of the reverse reaction. The equilibrium constant of the recognition can be presented as K, which is equal to k_{on}/k_{off}.

We first compared the differences in the recognition process as a function of DNA distribution on nanoparticles. Figure 4.3 (black dot) shows the time-dependent recognition profiles of Φ extracted from Figure 4.2b and c. Using the same method, the time-dependent of Janus particles and spherical particles can also be obtained, which allows a comparison of recognition processes for nano-objects with different geometries. From figure 4.3, we can conclude that the symmetric single particle shows a much more efficient absorption than the Janus particle and dimer. For example, the absorption of the single particles exhibits the fastest decay and achieves a plateau at in 120 minutes. Meanwhile, the Janus particle shows an intermediate decay rate, and takes about 300 minutes to achieve the equilibrium at Φ=0.4 . Dimers experience the slowest decay, with Φ is still as high as 0.8 when the measuring time t=500 minutes.

Figure 4.3. Absorption of nano-objects at DNA grafted surface density 0.5/nm^2 (a) time-dependent absorption profiles extracted from UV-vis spectrum, in which dimers are represented by black squares, Janus Particles are represented by red spheres and symmetric spherical particles are represented by blue triangles . The solid lines represent the fit s using the equation (2). (b) Corresponding k_{on} (shown as red) and k_{off} (shown as blue) obtained from fitting as described later.

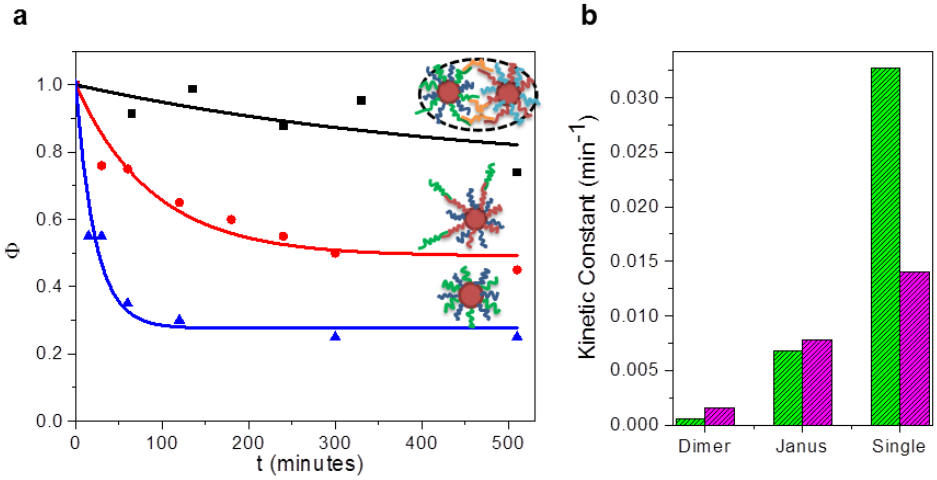

Table 4.1. Thermodynamic and kinetic parameters of the dimer, Janus particle and symmetric single particles at different surface densities obtained by fitting equation (2).

	δ=0.5/nm^2			δ=0.125/nm^2			δ=0.025/nm^2		
	Sphere	Janus	Dimer	Sphere	Janus	Dimer	Sphere	Janus	Dimer
k_{on} (min^{-1})	0.032	0.0068	0.00055	0.029	0.029	0.0027	0.03	0.022	0.006
k_{off} (min^{-1})	0.025	0.0078	0.0015	0.016	0.02	0.0019	0.012	0.006	0.0012
K	1.25	0.86	0.35	1.82	1.45	1.44	2.46	3.3	4.8

We then investigated the effect of the DNA-grafted density on the surface. Naively, one may expect a more efficient recognition in the presence of a surface with high DNA density. In previous research we also reported a significant faster aggregation of nanoparticles and microparticles systems with high DNA surface density than it does for particles with low DNA surface density. However, here, we observed an opposite trend. We found that for the surface of a particle with lower grafted density, the recognition process is much more efficient. For example, when the DNA density is as low as 0.025/nm^2 (black curve in Figure 4.4a), the system arrived at equilibrium at t=320min, with a corresponding Φ =0.2. When DNA density is 0.125/nm^2, the recognition shows an intermediate recognition rate with Φ=0.5 at t=500min.

In order to better understand and quantify k_{on} and k_{off} in this surface recognition process, we

applied a simple kinetic model to extract kinetic parameters. This model treats the recognition of the particle/cluster on the surface as a one-step recognition reaction.

$$P + s \leftrightarrow P - s$$

To simplify the model, we assume that (i) $[s] \gg [P]$, which means the number of recognition sites on the surface is larger than the number of particles(or nanoclusters) and can be considered as a constant during the recognition process; the assumption is reasonable because of the high packing density of the surface. (ii) The reaction is first order to the particles concentration. Therefore, the following equations can be obtained:

$\frac{d\emptyset}{dt} = -k_{on}\emptyset + k_{off}(1 - \emptyset)$, (1)

We use the following equation to describe the as a function of t by solving the previous equations:

$\emptyset = \frac{k_{on}}{k_{off}+k_{on}} e^{-(k_{off}+k_{on})t} + \frac{k_{off}}{k_{off}+k_{on}}$(2)

By fitting the decay of the particle concentration in the solution, we will be able to extract the information about the kinetics and thermodynamics process of this system.

We used equation (2) to fit the data points in Figure 4.3a and yields a series k_{off} and k_{on} as shown in Table 1. In particular, the comparison of kinetic parameters in δ=0.5/nm^2 was shown in Figure 4.4b. Those parameters are on the same order to the kinetic paramters obtained from DNA micro-array systems. [[119]] Consistent with what we observed in experiment, we found

that k_{on} of dimer is significantly lower than Janus particle's and single particles. For example, the k_{on} of symmetric spherical particle and Janus particles is 16 and 5 folds of what it does for the dimers, respectively. Besides, dimer also shows the lowest k_{off} . From figure 4.2b we could also find that, k_{off} is not as sensitive to the geometry of nano-objects as it does for k_{on}. The overall impact of geometry on the k_{on} and k_{off} yields to various equilibrium constant K. For example, at high surface density δ=0.5/nm^2

K of the symmetric nanoparticle is around 4 times higher than it does for the Janus particles. In other words, the geometry of nano-objects not only influences the kinetics of the recognition process, but also influences the thermodynamic process of the particles. This effect can be understood by the small reaction cross-section of asymmetric dimers/Janus particles compared with spherical particles. The detail mechanism will be discussed later.

Figure 4.4. Kinetics of dimer absorption at surfaces with different DNA densities at 0.1M salt concentration a) time-dependent adsorption profiles of dimers at DNA surface densities 0.025/nm^2 (shown as black square) , 0.125/nm^2 (shown as red spherical particle) and 0.5/nm^2 (shown as blue triangle) . (b) Corresponding kinetic constant dimer system extracted from profiles as described in the text.

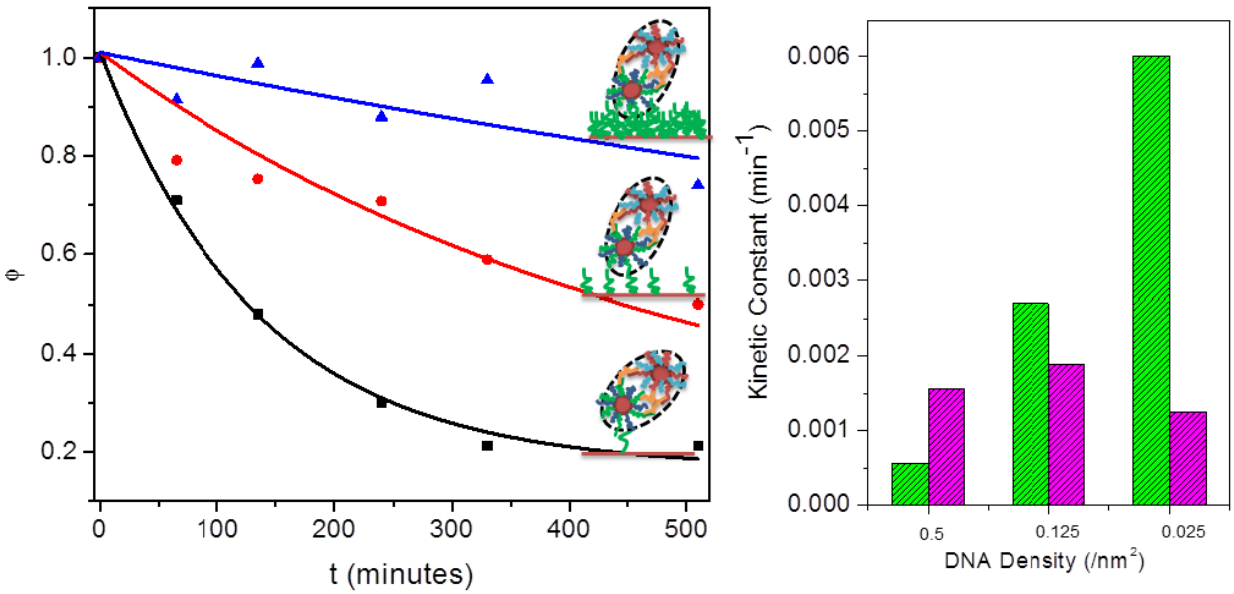

We fitted these time-dependent recognition profiles at different DNA grafted density by equation (2) and obtained various parameters as shown in Table 1 and Figure 4.5b. We found that, for dimer case, k_{on} increases a magnitude when we change the DNA surface density from 0.5/nm^2 to 0.025/nm^2, and increases 2.2-fold when DNA density increases from 0.125/nm^2 to 0.025/nm^2. Interestingly, k_{off} is not sensitive to the DNA density on the surface. The corresponding equilibrium constant, K, increased 13 times when the DNA surface density decreased from 0.5/nm^2 to 0.025/nm^2, and increased 3.4 times when DNA surface density decreased from 0.125/nm^2 to 0.025/nm^2 The same trend was also observed in the Janus particle system. For the

symmetric spherical nanoparticles, the recognition process shows a slight increase when we decrease the DNA density on the surface.

This effect can understood as follows: the DNA brushes on the surface provide the attraction force to the complementary DNA grafted on one side of the particle/clusters. At the same time, it provides the steric repulsion to the particles and clusters. For example, the density of DNA grafted on the nanoparticle is $14nm^2$/DNA, while for the surface with densest packing, the DNA grafted on the surface is $2nm^2$/DNA~$40nm^2$/DNA. For each particle with about 20nm in diameter (including 10nm diameter for hard core and another 10nm for DNA shell thickness), there are correspondingly about 8~170 DNA strands underneath. Due to the curvature of the nanoparticles, less than 5 connections can be made between surface and clusters. When significantly decrease the DNA density on the surface, the number of the connections remains the same and the hybridization energy does not change too much while the repulsion energy significantly decrease which eventually leads to fast recognition.

In order to further understand the effects of the nano-objects' geometry and DNA surface density on the recognition process, we proposed a model as followed

1) Thermodynamic model

We use a statistical mechanical model to interpret the experiments results and derive general thermodynamic parameter (such as ΔG and K) of the recognition process of nano-objects. This quantitative model has been successfully applied on the aggregation in micro-sized colloidal systems with DNA-mediated interactions.

The partition function of the DNA functionalized two micro-sized colloidal particle can be written as [reference]:

$$Z = \left(1 + ge^{-\beta\Delta F}\right)^{N} (3)$$

In which, N is the number of connections, g is the number of complementary strands which can be bound on the opposite surface. ΔF is the free energy of a single tethered DNA bond, which can be represented as $\Delta F = \Delta H - T\Delta S_0$. ΔS_0 is the configuration entropy cost due to the stretching of DNA when it try to reach the complementary DNA strand on the opposite surface. $\beta = \frac{1}{kT}$.

In order to obtain this simplified partition function, the possibility of hybridization for each DNA strands on these planar surfaces can be treated as the same . Since the length of the linkers is much smaller than the micro-sized particle radius R (L<<R), the assumption is fairly reasonable.

The assumption is not true for the nanoparticle cases when particle size is comparable to the DNA shell thickness. Due to the surface curviness of the nanoparticles, ΔF is the function of the relative position of the complementary DNA strands, For example, it cost less configuration entropy for DNA strands grafted nanoparticles which is closer to the surface to grab the DNA brushes on the surface than it does for the DNA strands father from the surface. Due to the surface curvature, k =1. The partition function of the symmetric spherical particle can be rewritten as:

$$Z = \prod_{i=1}^{i=N}\left(1 + e^{-\beta\Delta F(i)}\right) \quad (4)$$

For the assymmetric nanoparticles/nanoclusters, the partition function is the total number of all the possible connection statues.

$$Z = \sum_{N=1}^{N=Nmax} \rho \prod_{i=1}^{i=N}\left(1 + k_i e^{-\beta\Delta F(\rho)}\right) (5)$$

ρ(N) is the number percentage of each connected configuration in the all possible connection configurations, which describes the percentage of the connection number equals to N states over the total number of recognition statues. N is the number of connection in each configurations, N_{max} is the maximum possible connections can be achieved.

This model gives a qualitative interpretation on equilibrium constant K increases as the decrease of DNA grafted density on the surface. Different from nanoparticles' aggregation process, in which the number of connection (N) is determined by DNA grafted density. In the surface recognition system, because the DNA density on the 2D surface is much higher than it does on the nanoparticles, therefore, the number of connection N is only determined by the DNA grafted density on the nanoparticle. When we decrease DNA density on a 2D surface, N is a constant as long as the number of recognition sites on the 2D surface are more than the complementary strand grafted on the nanoparticle. When the DNA density of the surface decreases, the configuration entropy loss ΔS decreases significantly because it's much easier for a single stranded DNA in a coiled mushroom region to reach the DNA grafted on the nanoparticle surface compared it does for a ssDNA strands in a stretched brush region. Overall, these two effects lead to a decrease of Z , and therefore leads to a less negative ΔG and lower K.

2) **Kinetics Model**

The reaction kinetics of nanoparticle recognition on the DNA grafted surface is only dependent on the hybridization kinetics of the first DNA linkage in between, which can be represents as follows:

$$\frac{dC_a}{dt} = k_{(\sigma)} \times C_a \times C_b = k_{(\sigma)} \times 1/h \times \sigma \times C_a = k_0 \times \mathrm{e}^{-\beta\Delta} \times 1/\mathrm{h} \times \sigma \times N_c \times C_P \quad (6)$$

the reaction kinetic constant $k_{(\sigma)}$ is related to the surface DNA grafted density, for example, a surface with high DNA grafted density usually provides high steric repulsive force for the penetration of the strands and further leads to a high kinetic barrier. The concentration of the DNA grafted on the surface can be represented as $C_b = 1/h \times \sigma$, in which h is the height of polymer brush, σ is the DNA surface grafted density. The concentration of complementary DNA on the nanoparticles is determined by number of complementary DNA on each nanoparticles (N_c) and particle concentrationC_P.

For the assyemtric nano-objects, the asymmetric propertiy leads to a large number of inefficient collisions. Considering this effect, a steric factor $f(\rho)$ is introduced, which is the function of distribution of complementary DNA on the nanoparticle surface.

$$k_{on} = k_0 \times \mathrm{e}^{-\beta\Delta} \times f(\rho) \times 1/\mathrm{h} \times \sigma \times N_c \quad (7)$$

The equation indicates that the kinetic difference of the symmetric nanoparticles and assyemtric nano-objects comes from following 2 factors: 1) The difference of steric factor $f(\rho)$: f(dimer)<f(Janus)<f(spherical particle). 2) The asymmetric structure yields a high kinetic barrier from the penetration of the uncomplimentary strand. For example, Δ of dimers is more than the Janus particles' because of the influence from the other nanoparticles which are functionalized the uncompelemtary DNA strands, therefore, dimers exhibit the slower recognition rate. When decrease the DNA density on the surface, the kinetic barrier Δ significantly, which speeds up the reaction.

Figure 4.5 Absorption of dimers at DNA grafted surface density 0.5/nm^2 at different salt concentrations. a) time-dependent adsorption profiles of dimers at 0.1M (Black Square), 0.3M (red spheres) and 0.5M (blue triangle) sodium chloride concentrations. b) Corresponding kinetic constant k_{on} (shown as red) and k_{off} (shown as blue) extracted from fitting of the profiles.

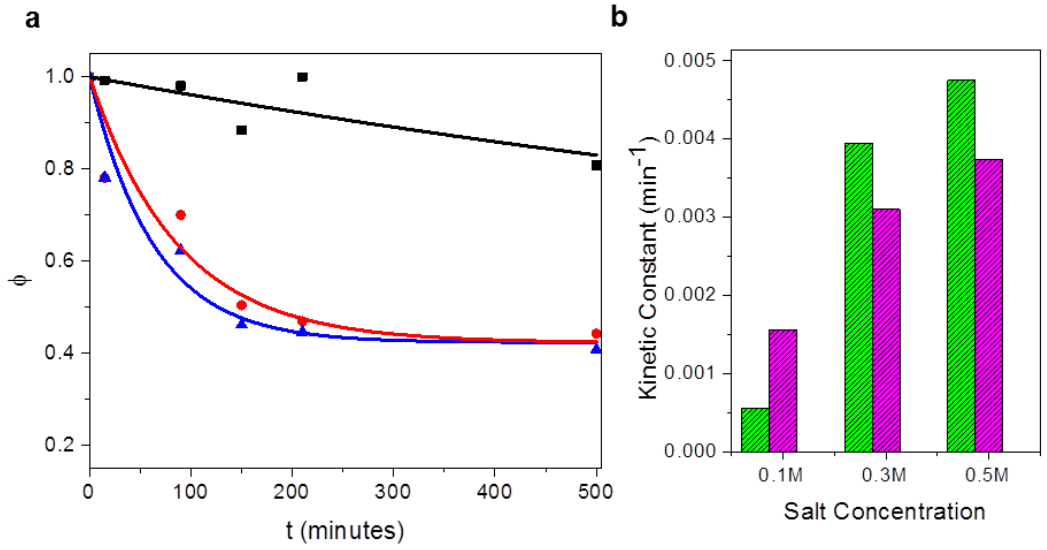

Table 4.2. Thermodynamic and kinetic parameters of the dimer at various salt concentrations extracted from Figure 4.5a.

	0.1M Salt	0.3M Salt	0.5M Salt
k_{on} (min^{-1})	0.00052	0.0039	0.0047
K_{off} (min^{-1})	0.0015	0.0031	0.0037
K	0.35	1.27	1.27

In order to further prove our hypothesis, we investigated the effect of salt concentration. By fixing other parameters the variation of salt concentration provides a more direct evidence to

confirm how kinetic barrier Δ and hybridization free energy of a single DNA strands influence the thermodynamic and kinetic process. Figure 4.5a shows the recognition profiles of the dimers at different salt concentration: 0.1M, 0.3M and 0.5M. When the salt concentration is as high as 0.3M and 0.5M, we observed a more efficient recognition. When t=300min, the recognition of dimers achieved the equilibrium with $\emptyset = 0.4$.

The recognition profiles yield to a significant increase of k_{on} and K when salt concentration increase from 0.1M to 0.3M and increase slightly when salt concentration increased to 0.5M as shown in Table 2 and Figure 4.5b. For example, k_{on} of the recognition increase 7 times when salt concentration increase from 0.1M to 0.3M , the corresponding k_{off} increase 2.4 folds and K shows a 3.6 folds increase. When salt concentration increase from 0.3M to 0.5M, the parameters do not have a significant increase. The similar trend was observed in various systems such as symmetric single particles. For example, k_{on} increase 6 times and K increase 2.5 folds for spherical single particle case when salt concentration increased from 0.1M to 0.3M.

The phenomena can be well explained by equations (5) and (7) as follows: at high salt concentration, DNA strands on the surface coil to mushroom regime and yield to a low penetration energy, which leads to a low kinetic barrier and eventually a higher k_{on}. At the same time, the free DNA hybridization energy (ΔF) becomes more negative at high salt concentration and results in a higher K.

4.3. Surface-based separation nanoclusters with different structure

Our discovery gives further insight on the surface-based dynamic self-assembly of nanoclusters and opens up many possibilities to develop various applications on the DNA-grafted surface. As

an example, we proposed two strategies to separate nanoclusters with different geometries by a DNA-encoded surface shown in the figure 4.6:

The first strategy separates dimers and single particles by taking advantage of the significant difference of the recognition kinetics has on the surface for various types of the nanoclusters. A surface with high DNA_C' (0.5 DNA/nm^2) can be utilized to absorb separate symmetric spherical particles and asymmetric dimers. Since the surface recognition process is much faster for the symmetric single particles than other asymmetric functionalized particles at this grafted density region, after a short incubation (about 2 hours), most of the single particles were absorbed to the surface, while the majority of the dimers were still in the supernatant. The separation has been proven by counting the number of dimers and single particles in the SEM/TEM images (Figure 4.7). The size distribution of nanoclusters is determined by dynamic light scattering (DLS). For example, as shown in Figure 4.7e an initial mixture is made up of about 22% dimers and 78% single particles, with a number averaged hydrodynamic diameter at 23nm collected from DLS. After incubation with a high density of surface-grafted DNA (such as $2nm^2$/DNA) for about 2 hours, the particle remains in the solution, containing a much higher population of dimers, which can also be confirmed by the increase of the particle size to 27nm (Figure 4.7 a and e), with about 55% of the particle forms dimer the solution. This approach provides a convenient one-step reaction to remove the majority of single particles from the solution. However, this method will not be able to obtain a high purity of dimers because, when the concentration of the single particles in the solution is lower than the dimers, the recognition rates of the single particles and dimers are getting close, the kinetic selection cannot be achieved. Therefore, we proposed another strategy which leads to a much higher separation efficiency.

Figure 4.6. Schematics of separation strategies to separate dimers and single particles. Strategy I, kinetic selection: separate single particles and dimers by the surface encoded with high DNA density; the surface will selectively bind to the spherical single nanoparticles in a short incubation time. Strategy II, thermodynamic selection: Selectively binding dimers with a surface encoded with DNA which is complementary to the DNA_N2' in the dimers. Low encoded DNA density on the surface greatly accelerates the recognition process.

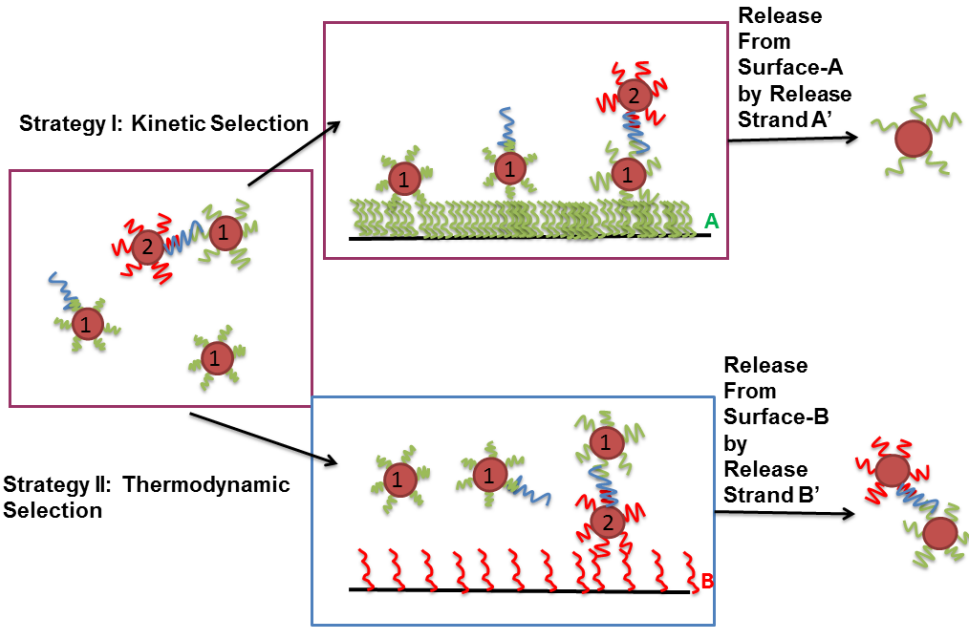

In the second strategy, we separate the nanoclusters by selectively binding the nanoclusters via another surface provides complementary DNA binding (Figure 4.6). The surface was functionalized with DNA_N2', which is only complementary to the DNA grafted on the other particle in the dimers and nocomplementary to any sequences on the spherical particles. By adjusting the DNA density on the surface to a low value, one can achieve an efficient absorption of dimers. At the same time, the single particles and Janus particles which functionalized with

the uncomplimentary DNA on the surface will be left in the supernatant. An extra step is needed to release dimers from the encoded surface by using the release DNA strand with a higher affinity to the DNA encoded on the surface. A similar statistic study has been carried out such as we did for the first strategy. It can be concluded that the percentage of particle forms to dimers has been improved from 63% in the initial mixture to 90% for the solution released from the surface (Figure 4.7c and d), with the number average of the diameter of the nanocluster mixture increasing from 30 to 36 nm. The particles in the supernatant are mostly single particles, with a size of about 18 nm (Figure 4.7e). These evidences confirmed the higher purities of dimers in the final product. Compared with other separation methods such as electrophoresis, these strategies provide convenient ways to separate large amounts of nanoclusters in order to achieve a high purity of one species. These approaches can be potentially used to separate nanoclusters with various structures.

Figure 4.7. (a, b) Statistic percentage of dimers and single particles obtained before separation and after separation using the described two strategies, respectively. (c,d) Corresponding SEM/TEM images of the mixture before separation steps (left), and the dimers obtained after separation steps(right) obtained from thermodynamic Selection. (e) Number averaged of the hydrodynamic diameter of nanocluster mixtures before and after separation steps by using kinetic selection (shown as blue) and thermodynamic selection (shown as red).

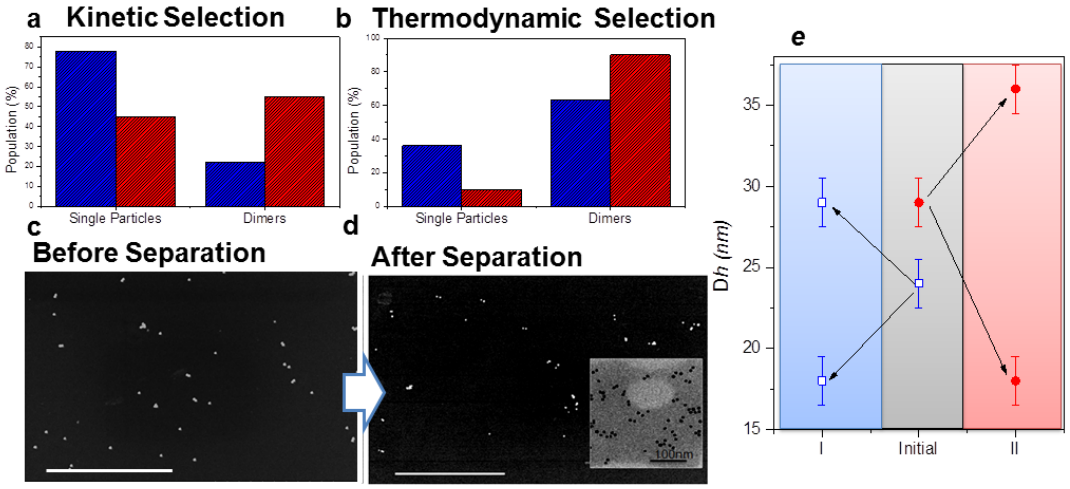

4.4.Building Hierarchical Structures using Dimers as a Building Block

Building a hierarchical structure by a small nanocluster unit is attractive from both a self-assembly point of view and application point of view. The success of a high yield of dimer synthesis allows one to use dimers as modular units to build a more complicated cluster with secondary or higher level structures. More interestingly, a dimer, as an asymmetric nanocluster, with two particles functionalized by two different types DNA brushes, allows for a directional interaction of the units. The aim of this work is to explore the dimer self-assembly process in the presence of various lengths and numbers of linkers in a self-assembly system.

Figure 4.8. A schematic illustration of the experimental design of hierarchical structure

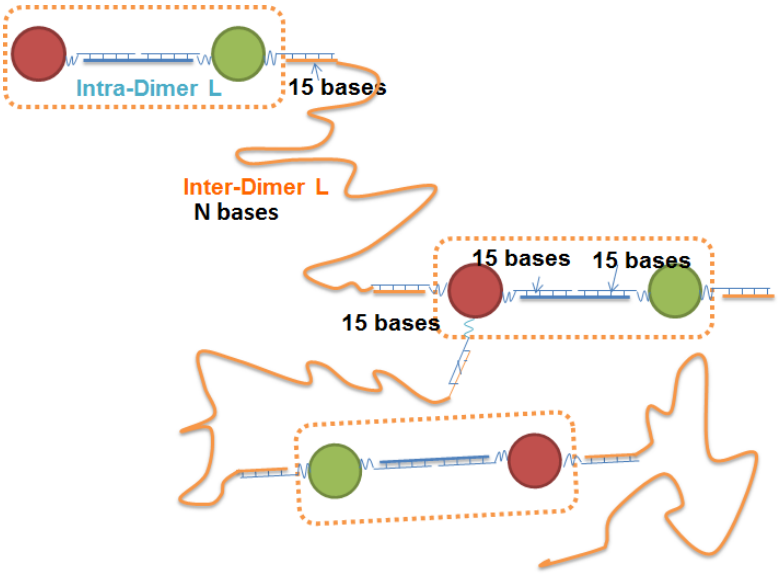

A schematic illustration of the experimental design has been shown in Figure 4.6, in which a secondary linker has been applied to connect the dimer of gold nanoclusters. As shown in Figure 4.6, there are two types of linkers in the system; one is the linker in the dimers (shown in blue), as denoted as intradimer linkers. The intradimer linker is composed of 30 bases of ssDNA with 15 bases complementary to ssDNA grafted on the particle's surface without any flexible spacer, leading to a rigid dimer unit . The other linkers used to connect dimers were interdimer linkers (shown in orange). Similar to the intradimer linker, this linker connects dimers with 15 complementary bases to both DNAs on the end of the dimers. However, the length of the linker can be varied by spacers with different numbers of poly T bases. The number of poly T bases was varied from 0 , 24, 75, 90, and130. SEM has been applied as a convenient tool to investigate the morphology of the clusters built by dimer units. Small Angle X-ray Scattering (SAXS) studies give more detailed structure information on how the dimer is aligned in an aggregate . The assembled structure was investigated as a function of interdimer linker number, length, and flexibility.

One of the challenging aspects of the self-assembly process of asymmetric structures is kinetics. As explained in chapter 4, dimers have a much smaller reaction cross-section than spherical particles, which leads to significantly slower recognition kinetics. In order to overcome this challenge, one may increase the length of linking DNA on the reaction cross-section. []For example, instead of simply mixing the dimers with linkers, one could first attach the linkers to the surface of one of the particles of the dimer by using a step-wise method to increase the self-assembly kinetics . On the other hand, the reaction kinetics is also dependant on the length and flexibility of the single-stranded linkers. Generally, the longer these single-stranded linkers are, the slower the reaction kinetics would be. When using a linker length of L=75, the reaction efficiency is greatly decreased. In order to achieve faster kinetics with long flexible ssDNA linkers, one could introduce a short double-stranded linker as described in the second system of chapter II.

We first explored the self-assembly behavior of the dimers in the presence of small ratios of interdimer linkers, with N= 3 linkers per dimer. The dimer solution was mixed with the interdimer linkers and was allowed to incubate at room temperature for a few days. At these conditions, there is not a significant aggregate in the reaction solution, indicating the comparatively small size of the aggregates. Their corresponding X-ray scattering data exhibits the same scattering feature as that which we observed in the dimer case, with the interparticle distance indicating slow binding efficiency at this linker ratio. SEM was applied to characterize the morphologies of the products present in the solution. In order to avoid the evaporation of solvent leading to the unspecific aggregation, all the SEM studies were performed on the silicate substrates coated with positively-charged PDDA. The nanoparticles modified with negatively-

charged DNA backbones will be attracted by the surface. The position of the nanoparticles could be fixed during the following rinse and evaporation processes.

Figure 4.9. Typical SEM images of the aggregates in the presence of ×3 of L0 (a), L24(b) and L75(c).

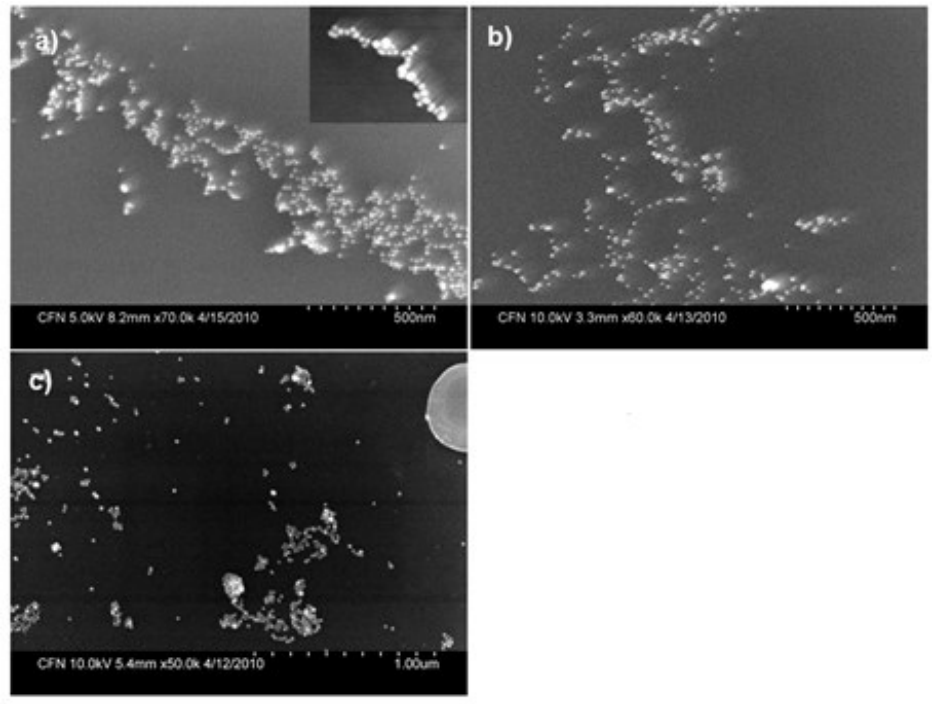

As shown in Figure 4.9, the aggregates tend to exhibit an 1D linear structure with a few branches. The effect can be explained as follows: when the number of interdimer linkers is lower, the repulsion energy from uncomplimentary DNA brushes, the interdimer linkers prefer to extend along the longitudinal axis of the dimer, leading to the end-to-end alignment of the dimers. However, when this aggregate happens to connect with single particle impurities, the symmetric spherical particle will ignore these directional interactions, which lead to a more random alignment and eventually leads to branching of the particle. This phenomenon confirmed that the asymmetric structure of the dimers leads to the directional growth of the structure.

The length of the dimer linker will influence the structures of the 1D dimer aggregates. The short interdimer linker (such as L=0 and 24 shown in Figure 4.7a and 4.7b) allows for a faster reaction, leading to a more rigid structure. While, at L=75, we observed long 1D structures with more flexible linkages

We continue to increase the ratio of linkers compared to the dimers. A SAXS study was performed on the aggregates formed by dimers with more than ×10 number of linkers; the details of data analysis is based on the previous chapter. For the ss-Stranded linker with different number of poly T spacers (for example, 24, 45 and 75), as shown in figure 4.10, the typical structure factor of the aggregates exhibits two broad peaks; the peak position of the second peak is roughly two times that of the peak position of the first peak. (Shown in Table 4.4) We could not tell the difference between the intradimer distance and interdimer distance from the diffraction peaks. The reason for that is probably because, when a single-stranded interdimer linker was used, the distance between the nanoparticles in the dimers is very close to the distance between the nearest nanoparticles in different dimers.

Figure 4.10. Representative 2D small-angle x-ray scattering patterns of dimers linked by L75 single-stranded/double-stranded interdimer linkers for ssDNA and their corresponding 1D structure factor .

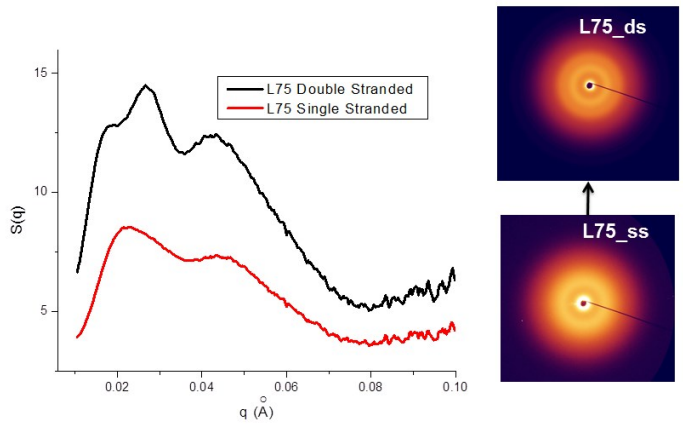

Table 4.3. The peak position of structure factors for dimer aggregates linked by various numbers of single-stranded interdimer linkers and their corresponding ratio. 75b represents the dimer aggregates connected by combined linkers with M=33, N=42 (as shown in Table 4.6). 100b represents the dimer aggregates connected by combined linker M=25, N=75. The peak positions in S(q) were determined by fitting a Lorentzian function.

SSDNA(number of bases)	Peak1	Peak2	Peak2/Peak1
45	0.023	0.041	1.78
60	0.024	0.041	1.71
75	0.021	0.0467	2.23
75b	0.0194	0.039	2.01
100b	0.202	0.039	2

Table 4.4. The peak position of structure factors for dimer aggregates linked by various numbers of double-stranded interdimer linkers and their corresponding ratio.

DS DNA (number of bases)	Peak1	Peak2	Peak3	Peak2/Peak1	Peak3/Peak1
45	0.023	00.41		1.78	
60	0.0245	0.042		1.83	
75	0.0169	0.0262	0.0448	1.55	2.62
90	0.0133	0.023	0.038	1.72	2.84
115		0.021	0.03858	1.82	

In order to signify the difference, the filler strands with corresponding numbers of poly A were added to switch the single-stranded spacers to double-stranded spacers, which will greatly increase the distance between dimers. For example, by adding the filler strands to the interdimer linkers with 75 poly T spacers, the interdimer linker turns rigid, which leads to a longer intradimer distance. The first broad peak in the structure factor of a structure linked by ssDNA at q=0.021 $Å^{-1}$was separated into two peaks at q=0.017 $Å^{-1}$and q=0.026 $Å^{-1}$(Shown in Table 4.4, 4.5). The first shoulder peak at q=0.017A^{-1} corresponds to the interdimer distance 36.9nm (estimated by $2\pi/q$), which is consistent with our previous measurement for the interparticle distance of double-stranded linkers at L =75. The second peak at q=0.026 $Å^{-1}$ corresponds to the intradimer linker, with the interparticle distance of the dimer at L=0. This is consistent with

values obtained using the dimer control sample: without interdimer linkers with the surface-to-surface, interparticle distance equals to 18nm (as described in the Chapter 2).

At interdimer linker length L=90, a similar phenomenon has been observed (shown in Table 4.3, 4.4): when a single-stranded linker was used, we only observed two broad peaks at q=0.0194 $Å^{-1}$ and q=0.039 $Å^{-1}$. After adding the filler strand, the first peak was separated into two peaks. The first shoulder peak emerged at q=0.0133 $Å^{-1}$, which corresponds to the interdimer distance of 47.2 nm, while the other peak is still at q =0.026 $Å^{-1}$, corresponding to the interparticle distance of the dimers. When a longer linker was applied (such as L=115 and L=130), the efficiency of the reaction was greatly decreased, therefore the majority of the particles are dimers which do not link into aggregates.

Later, we annealed these aggregates and the structure was melted without any feature in the structure factor. We failed to get a more organized hierarchical structure during this annealing process. The challenge for this annealing process is the small temperature window for the aggregates. The appropriate annealing temperature should be lower than the melting temperature of the dimers, but also at a higher temperature than the melting temperature of the linkers connecting the dimers. Melting temperature of the dimers is significantly lower than the DNA-linked aggregates, due to the smaller number of linkages caused by the few connections between particles. For example, the melting temperature of the dimer is around 35^{o}C. The melting temperature of linkers between dimers, on the other hand, can be as high as 55 to 60 ^{o}C . Therefore, it is important to find an overlapping temperature by carefully designing the DNA sequences.

If we continue increasing the ratio between linkers to dimers, the structure factor of the aggregates obtained from ×18 linkers shows similar diffraction peaks as the aggregates obtained from ×10 linkers with relatively weaker intensity. When the linker ratio increased to 36, the DNAs on one of the dimer surfaces will be saturated; aggregates cannot be formed by dimers at this condition.

Future work will be devoted to obtain a high quality of the 3D hierarchical structure and further understand the alignment of the dimer unit in the hierarchical structure. In order to achieve this goal experimentally, one needs to first achieve a high purity of dimers with fewer single particle impurities. Secondly, by carefully designing the sequence of the DNA on the nanoparticles, one might locate the small temperature window ideal for annealing these hierarchical structures, thereby producing an ordered structure.

Lastly, a mathematical method needs to be developed to analyze the structure factor of hierarchal structures. Regarding how we abstract the secondary structure from the structure factor of the dimer aggregates, the preliminary assumption is that the structure factor of the dimer aggregates is the convolution of the structure factor of the dimer and the structure factor of secondary structures (if we consider one dimer as a unit). More detailed analysis of this process is still in progress.

4.5 Conclusion

As a conclusion, we found that the symmetry of the DNA-grafted nanoclusters plays an important role in the self-assembly process. The study based on the interaction of

DNA-encoded spherical single particles, Janus particles, and heterogeneous dimers to a DNA-recognizable surface revealed that asymmetric nano-objects exhibit much lower recognition rates and equilibrium constants than it does for the symmetric functionalized nanoparticles. This different thermodynamic and kinetic behavior is attributed to the asymmetric distribution of recognizable DNA on the nanoparticle surface, as well as the entropy loss during the DNA hybridization. Moreover, the recognition process of asymmetric structures is very sensitive to the reaction environment; therefore, it can be easily tailored by the DNA density and salt concentration. This discovery allows for two convenient strategies to separate dimers from single particles based on a surface-selective binding process. Dimers can also be used as a unit to build hierarchical clusters in the presence of various ratios and lengths of interdimer linkers. A dimer's unique asymmetric structure allows for directional connections in the presence of a low ratio of linkers (N=~3), which exhibits the 1D morphologies. At a high linker ratio (N=10), the formation of the 3D hierarchical structure can be confirmed by the SAXS results, which featured both interdimer distance and intradimer distance. Our findings might have an important contribution to building complex structures with asymmetric units.

4.6 Method

Chemicals The streptavidin-coated magnetic microparticles (0.6 μm diameter) were bought from Seradyn . Table 4.5 lists all the ss-DNAs used in the study.All oligomers were synthesized and purified by a standard desalting process at Integrated DNA Technologies (Coralville, IA). The reaction took place in a 10mM sodium phosphate

buffer at pH=7. 0.1M NaCl was a standard buffer for the particle coating and dimer fabrication**.**

Table 4.5. The ss-DNA used in this study.

ss-DNA	Sequence 5' to 3'
DNA_C'	Biotin- TTT TTT TTT TTT AAT ATT GAT AAG GAT CTT GTG TC
DNA_N2'	CTT GTG TC-T ACT TCC AAT CCA ATT TTT TTT TTT TTT TT- Biotin
DNA_C	HS-C_6H_{12}- TTT TTT TTT TTT GCT ATC CTT ATC AAT ATT
DNA_N2	ATT GGA TTG GAA GTA TTT TTT TTT TTT TTT-C_3H_6-SH
DNA_N3	TTC TCT ACA CTG TCT TTT TTT TTT TTT TTT-C_3H_6-SH
DNA_N1	HS-C6H12-TTT TTT TTT TTT TAG CCT AAT AAC AAT
DNA_L_D	AGA CAG TGT AGA GAA ATT GTT ATT AGG CTA
Fuel_A	GAC ACA AGA TCC TTA TCA ATA TT
Fuel_B	ATT GGA TTG GAA GTA GAC ACA AG
Intra-dimer L	AGA CAG TGT AGA GAA ATT GTT ATT AGG
Inter-dimer L	AGA CAG TGT AGA GAA $(T)_{\boldsymbol{l}}$ATT GTT ATT AGG
Inter-Dimer L_M	AGA CAG TGT AGA GAA $(T)_{\mathbf{M}}$ ATT GTT ATT AGG CTA
Inter-Dimer L_N	TAG CCT CAT AAC ACT $(T)_{\mathbf{N}}$ TAG CCT AAT AAC AAT

Surface coating Two types of MMPs were modified by different DNAs by the biotin-streptavidin recognition. MMPs was modified by biolated ss-DNA_C' with 100% saturation, which provides a support to synthesis dimers (s-A). The effect of immobilized DNA density on the recognition process has been studied by MMPs. B was modified by biotinated ss-DNA_N2' with 5%, 25%, 50%, 75% 100% saturation (s-B). The reaction was taken place at room temperature, 5μL of the magnetic beads rinsed and resuspended in the buffer with the concentration of 1μM DNA-A, and allowed to react for about one hour until no further decrease of UV-absorption spectrum at 260nm has been observed, or all the biotinated DNA has been absorbed.

Fabrication of asymmetric Janus Particles and dimers: dimers were fabricated by the literature reported method, which was demonstrated in Chapter 2. In brief, single particles Au_1 and Au_2 were prepared by functionalizing 11nm Au nanoparticles with corresponding thiolated single stranded DNA, respectively. Firstly, 75μL MMPs A (s-A) was added to the 500μL solution with 5nM Au_1 and incubated for 1-2 hours, until almost all of the single particles were absorbed by the MMPs, accompanied by a color change from ruby red to colorless. Secondly, 3 times the amount of linker DNA_L_D compared to the amount of nanoparticles absorbed to the MMPs was added and incubated for about 2 hours. By releasing the particle from s-A, the Janus Particle can be obtained. The dimer's fabrication will continue.

Absorption of dimer by DNA functionalized surface s-B with different saturations were incubated in the dimer solution. Recognition of dimers on the DNA-coated surface leads to the decrease of dimer concentration in the solution, which has been monitored real-time by UV-vis. The color of the solution changed from ruby red to colorless.

Separation of dimers from single particles The mixture of single particle Au_1 and dimers has been used as the initial solution to evaluate the ability for the s-B to separate dimers and single particles. s-B with different saturation percentages was added to this mixture solution. After overnight incubation, the s-B was separated from the reacting solution, rinsed 3 times, and re-dispersed in the solution containing excess amount of Fuel_B, and the released solution was collected. Dynamic light scattering (DLS) was used to check the size of the nanocluster in the initial solution before separation, remaining solution after incubation, and the released solution from s-B.

Fabrication of dimer aggregates The dimer was fabricated by a step-wise method as explained in chapter I. The dimer aggregates were obtained by incubating freshly prepared dimer samples with various lengths of interdimer linkers described in the text. When a combined linker was applied, we first mixed $\boldsymbol{L_M}$ and $\boldsymbol{L_N}$, then mixed it with dimer units. The reaction is taken place at room temperature (25^{o}C). The reaction solution was allowed to incubate for several days.

Chapter 5

Sensing Nucleic Acids with Dimer Nanoclusters

Elements reprinted with permission from Advanced Functional Materials, **2011,** *21*, 1051.

5.1 Introduction

Gold nanoparticles (AuNP) are widely used for biodetection due to their unique optical properties, low toxicity, their compatibility with electrical measurements and electro-chemical processes,[120] and their relative ease of functionalization with a broad range of biomolecules.[32, 33, 121] Recent advances in DNA-based functionalization and assembly methods have allowed for the precise control of particle recognition properties, interparticle spatial properties, as well as architectural control of small clusters of particles. This specificity and tunability of nanostructures provides a platform for comprehensive biosensing strategies using an array of transduction approaches. [3, 122, 123] Signal transduction is best illustrated by the use of AuNP optical properties, which can be significantly modulated based on variations of the interparticle distances and particle arrangements. This serves as a basis for various state of the art detection schemes using colorimetric detection, Surface Plasmon Resonance (SPR),[124] and Surface Enhanced Raman Spectroscopy (SERS). [125]

A colorimetric scheme, based on highly specific binding of single-stranded oligonucleotides to induce nanoparticle aggregation was successfully demonstrated.[126] The

approach provided an experimentally simple platform for the detection of not only DNA, but heavy metals, proteins and small molecules including adenosine, ATP and cocaine. [122, 127, 128] One limitation in these aggregate-based assembly and disassembly detection schemes is related to the diffusion of analyte molecules in the condensed aggregates, and the necessity for aggregate formation for detection. This considerably affects the kinetics of the reaction since the compact structure of the aggregates restricts the diffusion of target molecules and reaction products. Moreover, the aggregate assembly/disassembly process requires bridging/opening of multiple interparticle connections and further particle diffusion. On other hand, while SPR and SERS were shown to be sensitive, they are often limited in a selectivity of detection.

A promising approach to address these limitations is to employ clusters containing only a few particles. Assembly or disassembly of such simple structures is not limited by analyte diffusion. Besides, the reduced steric and kinetic restrictions, the simple architecture of small clusters permits a more efficient reaction process compared to aggregates that can provide convenient integration with lab-on-a-chip microfluidic reactors. [129] Additionally, only a few target molecules are required for cluster disassembly; therefore, detection based optical properties of nanoclusters, such as fluorescence, [63, 130] plasmon resonance [33, 71, 88, 131] and the surface enhanced Raman signal, [132] may potentially allow for near single molecule analyte detection. For example, our recent results indicates that a modulation of fluorescent properties can be achieved in a dimer of metal-semiconductor particles, which might allow for a dimer detection on single molecule levels. [63] Here, we demonstrate the sensing properties of the simplest nanoparticle cluster, a dimer, consisting of two gold nanoparticles connected by a single-stranded DNA linker. The dimers are assembled using a modular stepwise surface encoded assembly method [71] that permits for a high-yield fabrication of dimers. By tailoring the

sequence of linker strands, this approach can be adapted for the detection of various target sequences. The novelty of this method is that detection is based on monitoring structural changes of the dimer during disassembly. Briefly, the disassembly is triggered by the ssDNA target, which replaces a dimer linker, as schematically shown in Figure 5.1a. Dynamic light scattering (DLS) is used as a convenient method to investigate dimer disassembly, as well as to probe the mechanism of the recognition of target DNA.[133] Through monitoring dimer disassembly, we demonstrated successful recognition of a target DNA sequence. Furthermore, we showed the ability of the dimer probe to discriminate single-base mismatches and the ability to recognize target DNA in the presence of interfering DNA oligonucleotides.

5. 2 Results and Discussion

The dimer probe, fabricated using a previously reported method of stepwise cluster assembly, [71] is composed of two 11nm gold nanoparticles (AuNP) connected by a ssDNA linker. The first particle, Au_1 was functionalized with a mixture of DNA_1 and DNA_1N which recognize the 5'-end of a ssDNA linker (DNA_L) and ssDNA modified surface (for fabrication purposes), respectively. A second AuNP was functionalized with DNA_2 (Au_2), which is recognized by the 3'-end of DNA_L. The DNA_L acts as the structural element that links the two AuNPs in a dimer morphology, provides interparticle separation, and acts as the recognition region for the analyte (Figure 5.1b). More specifically, DNA_L binds via 18 and 15 complementary nucleotides located at Au_1 and Au_2. The hybridization of DNA_T begins in the fully complementary interparticle spacer region of DNA_L and overlaps DNA_1 sequences, which results in dimer disassembly. The ratio between particle pairs and DNA_L controls the number of linkages within a dimer, which was fixed at three in this study.

We first investigated the disassembly of the dimer using DNA_T, a 27-b DNA that is

complementary starting at the 5'-end of DNA_L and includes 9 bases of the interparticle spacer region. Thus, DNA_L has a higher affinity for DNA_T than it does for DNA_1 on the particle surface because it demonstrates a greater complementarity with the former. The hybridization between DNA_T and DNA_L is expected to occur first at the exposed overhang and to proceed by branch migration until DNA_1 and DNA_L are completely dehybridized.[31] To better describe this process, we name the target recognition side (T-side, Fig 5.1b) of DNA_T as the region which initially hybridizes to DNA_L first, and the replacement side (R-side) as the region that gradually replaces the DNA_1 bound linkage, leading to disassembly. [31]

Figure 5.1. Schematic design of dimer nanoparticle clusters. a) Bulk representation of dimer disassembly in the presence of target DNA b) The dissociation process of dimers induced by binding of target ss-DNA. Linker DNA (green) connects particles functionalized with single-stranded DNAs (blue). Target DNA (pink) attaches to ss-part of DNA-L by its Target side (T-side), subsequently Replacement side (R-side) substitutes DNA from the particle in the hybridization with DNA-L, which results in a dimer dissociation.

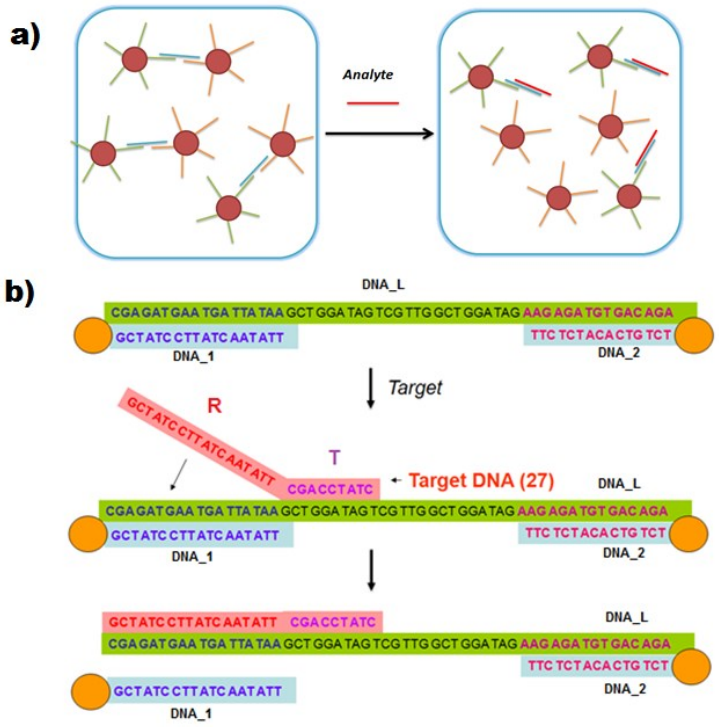

As a result of the DNA_T recognition, the dimer separates into two asymmetric nanoparticles with slightly different structures: Au_1 and Au_2 to which the DNA_L – DNA_T complex is attached. The change from dimer cluster into two separated AuNPs results in a change in hydrodynamic diameter (D_h), which can be monitored via dynamic light scattering (DLS). Figure 5.2a shows representative time-dependent disassembly profiles based on the number averaged D_h for the recognition of DNA_T by the dimers. The dimers assembled using linker

DNA_L show D_h of 33 nm, while the D_h of single particles is close to 19 nm. The D_h value for the dimer cluster agrees with the model estimation. In the model a dimer is represented as an ellipsoidal object. The short diameter of ellipsoid corresponds to the diameter of the particle, while its longer diameter relates to the sum of particle diameters (19 nm) and DNA linker (12 nm). DLS measurement probes an average hydrodynamic diameter, determined by the diffusion of an ellipsoid with dimensions corresponding to those of the dimer.[71] Upon addition of DNA_T we observed a gradual decrease in D_h from 33 nm to 19 nm, which is associated with a disassembly of the dimers into single particles. The disassembly reactions took place at 33^{o}C. Control experiments show that in the absence of target DNA, the dimers were stable at this temperature for several days.

The resulting disassembly kinetics for the dimer with DNA_T were found to be influenced by a number of conditions, including the concentration of dimer probes and target molecules, and the number of mismatches in DNA_T, as discussed below in the detail. The detection limit of the DLS instrument used in our studies is about 0.05 nM of AuNP, which is 40 times less than the minimum concentration of AuNP used in this study. A typical standard deviation of D_h is about ±1 nm as measured in multiple measurements (3-5 times) for static samples, whereas the larger error observed for the reaction process, is due to the changing solution properties during the measurement time. We quantified this error by conducting triple reaction measurements, and it was used to estimate uncertainty of our kinetic analysis (a characteristic disassembly time).

To examine the details of the disassembly based detection, we investigated the dimer disassembly kinetics for a range of DNA_T: 5 nM, 10 nM, 20 nM, 40 nM, 50 nM and 105 nM of target with 2 nM dimer (Fig. 5.2a). For these concentration regimes, there is an excess of DNA_T relative to the dimer, while at the same time maintaining a minimal dimer concentration

that is reliably measured by DLS ([dimer]=2 nM). For DNA_T at a concentration of 105 nM (about 50 times the dimer concentration), dimer disassembly was completed within approximately 20 min. In contrast, full disassembly was not reached within 120 min at 5 nM of DNA_T. This indicates that the concentration of DNA_T has a significant effect on disassembly kinetics.

In order to better understand and quantify this disassembly based detection, we applied a simple kinetic model (Fig. 5.2b), that treats dimer disassembly as a two-step recognition reaction. During the first step, DNA_T first undergoes attachment to DNA_L, which results in the formation of an intermediate dimer-target complex. This reaction is reversible with reaction rate constants, k_1 and k_2 for hybridization and dehybridization of the target DNA_T, respectively. During the second step, the DNA_T replaces the Au_1 linkages at DNA_L, and the dimer-target complex disassembles into two single particles with reaction rate constant k_3.[119, 134-136] Here, $[Au2NP], [DNA\_T]$ and $[Au2NP - T]$ correspond to the concentrations of dimers, targets, and intermediate complexes, respectively.

To simplify the model, we assume that (i) $[DNA\_T] \gg [Au2NP]$, which means the concentration of target DNA can be considered constant during the reaction; (ii) the reaction is first order to the dimer concentration. In this steady-state approximation, the following equations can be obtained:

$$\frac{d[Au2NP]}{dt} = -k_1[Au2NP][DNA\_T] + k_2[Au2NP - T] \quad (5.1)$$

$$\frac{d[Au2NP-T]}{dt} = k_1[Au2NP][DNA\_T] - k_2[Au2NP - T] - k_3[Au2NP - T] = 0 \quad (5.2)$$

Combining equation 5.1 and 5.2, the time-dependent percentage of dimer left in solution can

be obtained as:

$$\varphi\ (t) = \frac{[Au2NP]}{[Au2NP]_{t=0}} = e^{-\frac{t}{\tau}} \quad (5.3)$$

where the characteristic disassembly time τ is given by

$$\frac{1}{\tau} = \frac{k_1 k_3}{k_3 + k_2}[DNA\_T] \equiv K[DNA\_T], \quad (5.4)$$

$[Au2NP]_{t=0}$ is the initial dimer concentration, and K is a kinetic constant of the disassembly reaction, and □ is a characteristic disassembly time.

When dimers are fully consumed, they separate into two types of single particles. Given the relatively small differences (for DLS) in the sizes of dimer and single particles, we approximate the number average of the diameter as

$$D(t) = D_{single} + \Delta D \times \frac{\varphi\ (t)}{2 - \varphi(t)} \quad (5.5)$$

$D(t)$ is the real-time measured number averaged hydrodynamic diameters of a mixture of dimers and single particles. D_{single} is the number averaged hydrodynamic diameters of single particles correspondingly, and ΔD is the difference between diameters a single particle and a dimer.

Figure 5.2. DLS based measurements of dimer disassembly. a) DLS based time-dependent dimer dissociation profiles for 2 nM of dimer at target concentrations 5 nM, 20 nM and 105 nM. b) The measured dependence of τ on target concentrations (points). The fit using the shown kinetic model for the disassembly (line) yields $K=1.38\times10^{4}$ $M^{-1}s^{-1}$. Measurements were performed in triplicate for each target concentration.

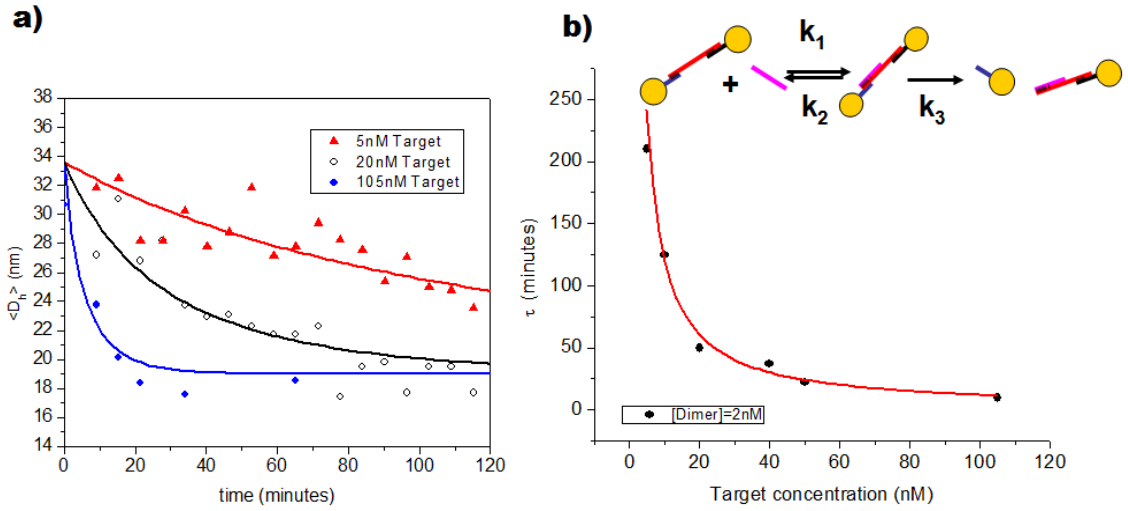

We applied this model to the time-dependent disassembly profiles, as shown in Fig. 5.2a, by equation 5.5, for all the curves obtained for the concentrations listed above with a fixed D_{single}=19.0 nm that is measured for individual particles before assembly. This assumes that all samples from the same batch contain similar amounts of single particle impurities in the initial solution and a core size of the gold particles is the same. The assumption is reasonably justified, since all dimers were fabricated from AuNPs of the same synthetic batch. Moreover, DLS confirmed similar magnitudes of D_h of single particles and fabricated dimers for all batches of dimers used in disassembly studies. We found that each disassembly profile can be described by a characteristic disassembly time τ obtained by fitting with the kinetic model discussed above. For the target DNA_T, rate constant K is assumed to be constant.

The model allows for extracting the kinetic parameters of the disassembly reaction from the DLS data set. Figure 5.2b summarizes the dependence of τ on DNA_T concentration in the range from 5 to 105 nM. The fit using equation 5.5 indicates a reasonable agreement with experimentally derived τ values and yields $K = 1.38\times10^4\ M^{-1}\ s^{-1}$. This also shows that in the concentration regime of DNA_T exceeding dimers by at least 5 times, an initial concentration of dimers does not affect the disassembly reaction rate. When the target concentration is decreased to 5 nM, and dimer and DNA_T concentrations become comparable, the model is no longer applicable and a discrepancy between the experimental data and calculated curve is observed.

We compared our results with reactions involving surface-immobilized DNA used in DNA microarrays, as both systems share similar features including steric limitations due to a molecularly crowded environment and surface immobilization of reacting DNA. Although the reaction kinetics depends on environmental parameters, geometry of hybridization and sequence details, our results show that the kinetics of DNA hybridization on surfaces and two-step hybridization/ dehybridization for microarrays and dimers respectively are comparable. Indeed, for microarrays, the hybridization rate is on the order of $10^4 \sim 10^5\ M^{-1}\ s^{-1}$ and dehybridization rate constants of $10^{-5}\ s^{-1}$. [119, 135] Since k_2 is rather small, we assume $k_3 >> k_2$, and, which yields K is on the order of $10^{4\sim5}\ M^{-1}\ s^{-1}$, which is consistent with our result of $K = 1.38\times10^4\ M^{-1}\ s^{-1}$. Moreover, this unique dimer probe has the advantage over microarrays because of its fairly easy analysis process and faster detection time.

To evaluate the sensitivity of the dimer sensor to mismatches within the target, we investigated the dimer dissociation kinetics as a function of modifications made to the target DNA_T sequence. Specifically, we introduced mismatches in various locations within DNA_T, as shown in Table 5.1, to reveal the influence of binding kinetics on hybridization and strand replacement,

discussed above. First, the chosen placement of mismatches probes the difference between mismatches on the T-side and R-side which are related to the initial binding of analyte strand to the linker and the following replacement of bound DNA respectively. We also vary the degree of mismatches on each side (T- or R-) to evaluate their effect on an analyte binding and reaction rate. For example, the R-3mid and T-3mid have three mismatches in the middle of the R-side and T-side, respectively. Secondly, we study the difference between the mismatches on the same side of the target DNA_T but at the middle or at the end, e.g. T-3mid and T-3end, since they affect the kinetics of initial attachment of strands. Moreover, considering that the hybridization efficiency is influenced by the GC content of target, the mismatched strands were designed by replacing the A with C, and T with G base and so on in order to minimize the uncertainty of the influence from the target's sequence.

We found that the number and location of the mismatches can significantly influence the disassembly process. Figure 5.3 shows the time-dependent disassembly profiles for targets with different mismatches when collected at the same target concentration (20 nM). For example, dimers in the presence of fully complementary DNA_T, a single mismatch (T-1mid) and triple mismatch (T-3mid) strands displayed different disassembly kinetics. A qualitative comparison of disassembly profiles (Figure 5.3a), shows that for the single-mismatched DNA sequence (T-1mid) the disassembly rate increased to at least 2 hours thereby indicating that dissociation of the dimer is significantly slower contrasted to the disassembly rate in the presence of a fully matched target.

Table 5.1. Single-stranded DNA sequences. The sequences of mismatched strands and comparison of their estimated kinetic parameters, as described in the text. Yellow labels indicate the mismatches compared to perfect matched strand. The error bars for τ are determined from the curve fitting, the error bars for K are not shown.

Mismatches (number)	Sequence	τ (minutes)	K ($M^{-1}s^{-1}$)
Target (perfect matched) (0)	GCT ATC CTT ATC AAT ATT CGA CCT ATC	48.2±5.24	1.73×10^{4}
T-1mid (1)	GCT ATC CTT ATC AAT ATT CGC CCT ATC	130.2±8.23	6.40×10^{3}
T-3end (3)	GCT ATC CTT ATC AAT ATT CGA CCT CGA	706.9±128.2	1.18×10^{3}
R-3mid (3)	GCT ATC AGG ATC AAT ATT CGA CCT ATC	797.9±103.8	1.04×10^{3}
T-3mid (3)	GCT ATC CTT ATC AAT ATT C TC ACT ATC	3328.3±1192	2.50×10^{2}
T-5end (5)	GCT ATC CTT ATC AAT ATT CGA CAG CGA	N/A	N/A

Figure 5.3: Investigation of the effect of mismatch position and number. a) DLS measurements display dimer dissociation in the presence of perfect matched strand, mismatched targets: T-1mid and T-3mid and b) the comparison of kinetic rate constant K for different mismatched targets list in Table 5.1 obtained from fitting curves. The inset graph shows corresponding τ values.

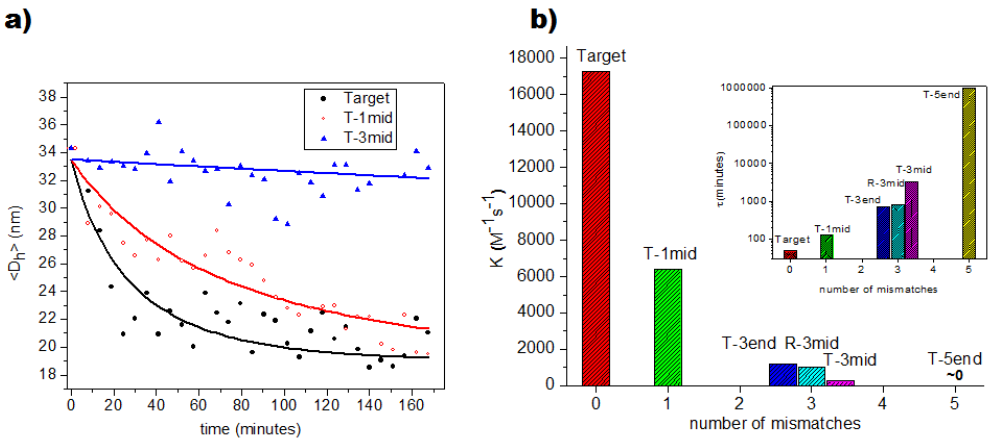

A similar data fitting procedure using equation (5.5) was used to quantify the disassembly rates of the mismatches. The values obtained for this fit for the various mismatched strands are shown in Table 5.1. For example, for DNA_T, τ is ~48.2 min, as found before, while a single mismatched T-1mid τ is ~130 min, corresponding to a longer disassembly time. The observed threefold difference between the τ of DNA_T and a target with a single mismatch, such as T-1mid, allows for the reliable detection of single-mismatches. For the targets containing 3 mismatched bases (T-3mid, T-3end and R-3mid), the value of τ varies from 706.9 to over 3000 min, depending on the location of mismatches. When the number of mismatches is increased to 5, practically no disassembly behavior is observed, i.e. τ is drastically increased to ~ 10000 min and its exact value cannot be determined reliably. When studied under identical conditions, the observed difference in τ indicates different reaction kinetic rate constants K, which can be estimated as $K = \frac{1}{[DNA\_T]\tau} \times \frac{1}{60} \times 10^9$ M^{-1} s^{-1}. The corresponding kinetic rate constants for the target strands with different number of mismatches are shown in Table 5.1 (and Fig. 5.3b). The observed reaction rates of the targets with different degrees of mismatches exhibited the following trend: K (perfectly matched target) > K(T-1mid) > K(T-3end) > K(R-3mid) > K(T-3mid) > K(R-5mid). In general, a larger number of mismatches in the target yielded a slower reaction, with each additional mismatches resulting in approximately a threefold decrease in K. The observed threefold difference between the kinetic constant of DNA_T target and a target with a single mismatch, such as T-1mid, allows for the reliable detection of single-mismatches.

These results show that the location of mismatch within DNA_T plays a significant role in dimer disassembly kinetics. This can be explained by accounting for the details of the hybridization process between DNA_T and DNA_L.[31, 137] The T-side of the linker DNA will participate in the initial hybridization process and form a stable target-dimer complex.

Subsequently, if energetically favorable, the R-side of the target DNA can replace the DNA strand attached to the particle and form a new double-stranded helix with the linker DNA_L, resulting in dimer disassembly. This dependence provides further insights into the binding and disassembly mechanism. For instance, the hybridization of the T-side of the target DNA_T with that of the ssDNA spacer region of the linker DNA_L can thus be considered as the rate limiting step. If the T-side is not able to hybridize with the single-stranded spacer region of the linker, or the hybridization efficiency is low at the given temperature for a given number of mismatches, then there is a significant barrier or insufficient energetic gain for the target strand to hybridize with the linker, even if the R-side provides a perfect complement, as for example in the case of T-3mid. Moreover, when three mismatches are located in the middle of the target (T-3mid), disassembly shows the least propensity.

Figure 5.4. Dimer disassembly in the presence of interfering ssDNA a) τ values from interference experiments at different ratios between interference T-3mid strands and perfect matched strand as indicated at the constant target concentration (20 nM) ; b) the dependence of measured (points) τ on the same total concentration of target and T-3mid strands (50 nM) with different concentration of target, Fit (line) yields $K=1.48\times10^{4}\ M^{-1}s^{-1}$, the result is consistent with the magnitude of K obtained without T-3mid mismatched single-stranded DNA.

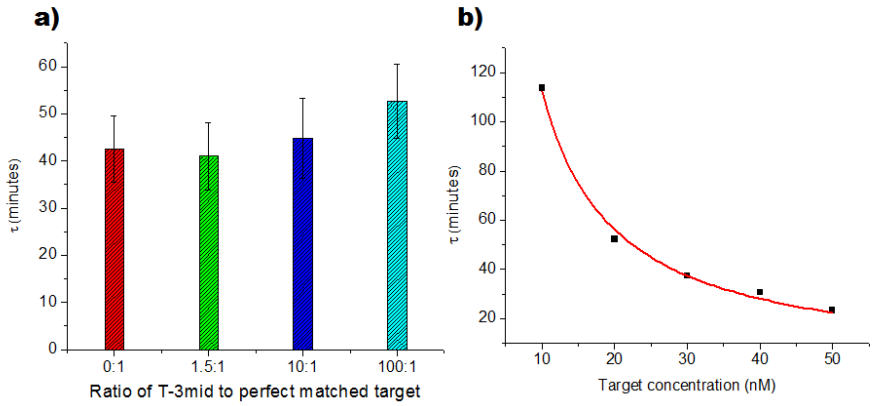

A critical aspect to all sensor designs is the potential for interference and false positives. In DNA sensor systems, interference is often due to the presence of other DNAs in the system. Although not fully complementary to the dimer probe, these DNA sequences may be able to bind to the recognition domain and compete with the target DNA sequence. The presence of competing DNA sequences is a particular concern for a complex biological sample. To examine the stability and specificity of the dimers to molecular interferences by competing DNA oligonucleotides, we used T-3mid as an interfering DNA strand. Two sets of interference data are shown in Figure 5.4. Here, the same DNA_T concentration (20 nM) was used in the presence of different ratios of T-3mid. First, we measured the disassembly profiles for different interference ratios (from 1.5 to 100) between T-3mid and DNA_T, and then obtained τ for each ratio using equation 5.5. As described above, in the absence of mismatched strands, DNA_T exhibits a τ equal to 42 min. When T-3mid strands were added in ratios of 1.5, 10, and 100, the τ slightly increased to 52, which is within the range of experimental error. This result indicates that detection of DNA_T is not affected by the presence of interfering T-3mid, despite its high excess, and 3 mismatches. In a second experiment, the total concentration of oligonucleotides (DNA_T and T-3mid) was held constant in the solution for a total combined concentration of 50 nM. The concentration of T-3mid strands was varied between 0 nM to 40 nM, and the concentration of target DNA from 50 nM to 10 nM, respectively. The measured size decay rate for dimer dissociation was found to be dependent on the target DNA_T concentration. By fitting the size-decay curve as described above, we obtained $K = 1.48\times10^{4}\ M^{-1}s^{-1}$, in which the magnitude is consistent with the kinetic behavior of dimers reacting only with the fully complementary DNA_T. Thus, both results confirm that the dimer probe is insensitive to interference caused by single-stranded DNA with a sequence very similar to the target.

In order to prove the ability to detect target nucleic acid on a single-molecule level based on an approach of nanocluster disassembly, we performed single-molecule level measurements on the gold and quantum dot (QD) nanoclusters in the presence of target DNA strands on a homebuilt single-molecule microscope. A Au~QD nanocluster is composed of a 50nm Au nanoparticle and several 10nm quantum dots (with 5nm core and 5nm shell) with emission wavelength at 605nm. The size of the Au nanoparticle is intentionally selected to match the excitation wavelength of the laser by its surface Plasmon band. Moreover, this size of the gold nanoparticles allows for a large quenching. The nanocluster was fabricated in a step-wise bio-encoded method according to literature (as shown in Figure 1.4). In particular, the magnetic beads were first coated with DNA_1N, which is complementary to the DNA_1 on the 50 nm Au nanoparticles by 15 base pairs on the end of DNA shells. In the first step, Au_1 was attached to the surface of the magnetic beads. In the second step, × 300 of DNA_L was connected to Au_1. Because of the blocking of the magnetic particles, the DNA_L only attached the upper hemisphere of the Au_1. The unreacted DNA_L was removed. In the third step, about × 100 of quantum dots coated with DNA_2 was attached to the 50nmAu nanoparticles. The size of the quantum dot coated with the DNA shell is about 10nm, which is much smaller than the Au_1 nanoparticles. Therefore, an Au_1 nanoparticle was connected with tens of quantum dots, which only cover the upper hemisphere of the Au nanoparticle surface. The unreacted quantum dots can be efficiently removed by separating the supernatant, followed by rinsing the magnetic particles several times. The assembled Janus nanoclusters were then released from the surface of the magnetic particles by adding DNA_F.

We first investigated the disassembly of Au-QD Janus nanoclusters in the presence of target strand DNA_T by DLS. After incubating with DNA_T, the hydrodynamic diameter of the

nanocluster decreases to the diameter of the gold nanoparticle, as shown in Figure 5.5. The result confirms the successful disassembly of the Au-QD nanoclusters in the presence of DNA_T.

Figure 5.5. DLS-measured number averaged hydrodynamic radius of Au nanoparticles (green), and Au-QD Janus cluster before (black) and after (red) adding DNA_T.

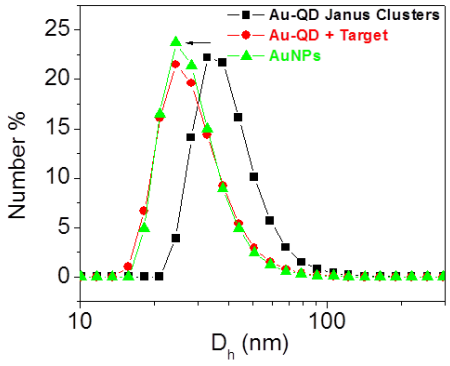

We further measured PL intensity and lifetime on a home-built single-molecule microscope, illustrated in Figure 5.6. We placed a droplet of the Au-QD nanoclusters with concentrations down to 10^{-15}M on the mica glass surface. The nanocluster was excited by a 532nm laser, which corresponds to the surface-plasmon band of the 50 nm Au nanoparticles. Then, we added the target strand to the droplet. The quantum dot was then released from the surface of the gold nanoparticle, and diffused to the solution, which eventually disappeared from the observation focus plane on the surface. The lifetime of the quantum dot on the gold nanoparticle surface and intensity of the nanocluster were measured in a time manner.

Figure 5.6. Schematic design of experiments for the disassembly of Au~QD Janus clusters.

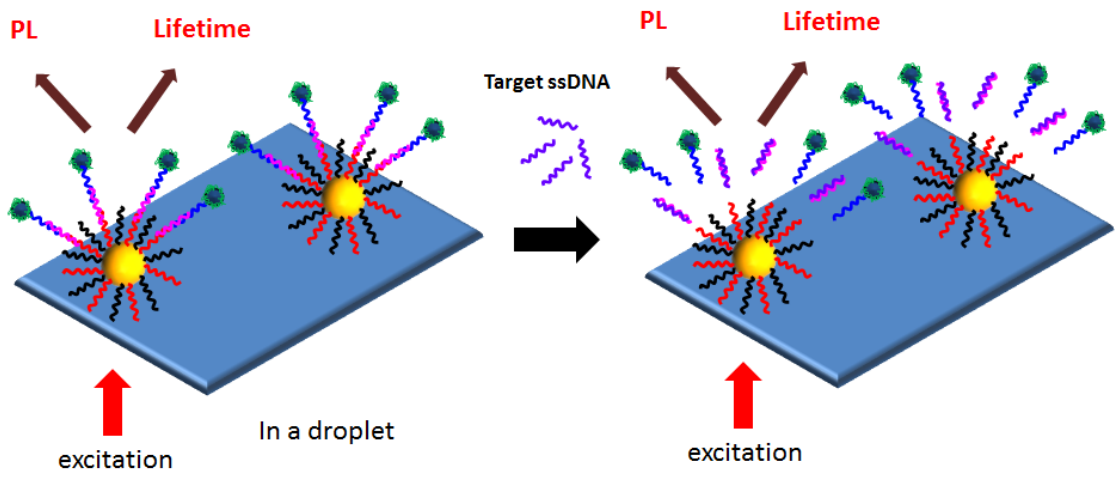

Figure 5.7 shows the measured result of PL intensity of the nanocluster and lifetime of the quantum dots attached on the Au nanoparticle in a time manner. The intensity of the Au-QD gradually decreased from approximately 200 to 20 in half an hour (shown in red dot Figure 5.7a). This result indicates the release of the quantum dot from the Au nanoparticle surface. Moreover, decreasing intensity corresponds to the release of each single quantum dot in a distinguishable time-interval. Figure 5.7b exhibits the quantum dot's releasing process. Instead of releasing all at once from the surface, quantum dots were disassembled from the surface of a Au nanoparticle step by step. Each single quantum dot release can be captured by single-molecule microscopy.

Correspondingly, the variation of lifetime of one particular quantum dot is shown in black in Figure 5.7a. The lifetime of a free QD is about 20ns. The lifetime of this quantum dot connected to the Au nanoparticle was stabilized at 12ns in the first 25 minutes, which indicates the quenching effect of gold nanoparticles to the quantum dots. The lifetime of the quantum dot then significantly increased from 12ns to 16ns in the next 10 minutes, until it disappeared from the observation plane. This result suggests that this particular quantum dot was sitting on the

surface of the Au nanoparticle in the first 20 minutes, and began to release in the 25~35 minute range, which leads to an increased interparticle distance between the Quantum dot and gold nanoparticle, and eventually leads to a shorter lifetime. These preliminary results confirm the potential of using nanocluster disassembly as an ideal platform to detect nucleic acid in the single-molecular level.

Figure 5.7. Measured PL intensity and lifetime of Au~QD Janus cluster disassembly (a) and proposed disassembly mechanism (b).

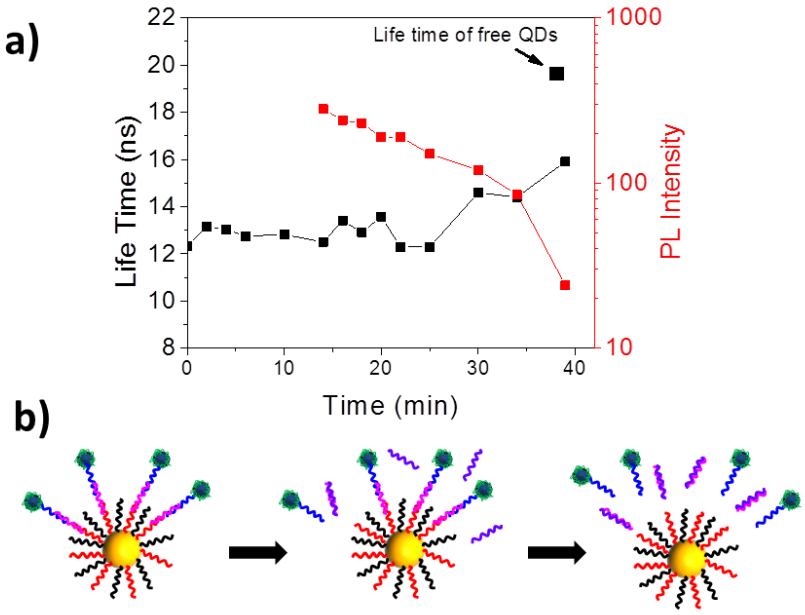

5.3 Conclusion

Dimer nanoclusters, assembled from DNA coated nanoparticles and connected by linker DNA, provide a promising platform for sensing single-stranded DNA. In the presence of target DNA, the dimers undergo disassembly, which is monitored by DLS. We further used DLS to investigate the operation of the sensor, kinetics of the disassembly process and factors influencing its

detection sensitivity. A two-step kinetic model was applied to quantify a reaction of dimer with target DNA strands. The dimer sensor demonstrated high target specificity, allowing for discrimination on the level of a single-base mismatch, at the same time, it maintained selectivity in the presence of interference DNA. The single-molecule level measurement indicates the potential to use this platform detect biomolecules in a single-molecule level.

5.4 Methods

DNA functionalized dimer was fabricated followed the method presented in the previous chapter.

DLS based real time measurement of disassembly of dimer DLS measurements were performed on a Malvern Zetasizer ZS instrument. The instrument is equipped with a 633 nm laser source and a backscattering detector at 173^{o}. Measurements were recorded at 33^{o}C. The dimers were dispersed in a 0.1M PBS solution and measured. Then, analyte strands were mixed with the dimer solution in the cuvette. In typical reaction, 2nM of dimers reacted with 20nM analyte strands. The change of hydrodynamic diameter over time was monitored in 6 minutes increments.

Single molecule measurement of the PL intensity and lifetime Ensemble PL lifetimes, FLIM, and single-particle fluorescence microscopy measurements were performed on a home-built confocal scanning stage microscope based on an inverted microscope (Olympus IX81, 1.4 NA 100_ oil objective) equipped with a piezo scanning stage (Physik Instrumente, Germany) and coupled to a diode-pumped solid-state laser system delivering 590 nm pulses of 250 fs width, at 8 MHz repetition rate (Spectra Physics, Newport). The average power at the sample was kept at about 100 nW. The fluorescence was collected in epiillumination format, spectrally separated from the excitation laser light by a dichroic (Semrock, DiO-594) and by a band-pass filter

(Semrock FF01-628/40), and detected by a single photon counting avalanche photodiode (APD,MPD Picoquant) and a time-analyzer (PicoHarp 300, PicoQuant). For single-particle spectroscopy, fluorescence was split (50/50) by a nonpolarizing beam spliter cube and detected by two APDs to allow for antibunching measurements Data acquisition and data analysis were performed with the Symphotime analysis software (Picoquant). Dynamic light scattering experiments were performed on a commercial Malvern Zetasizer NS.[138, 139]

Chapter 6

Diffusion of Nanoclusters in Polymer Solutions

6.1 Introduction

6.1.1 Basics of Diffusion

The efforts contributed to study the diffusion of a meso-scale object can be traced back to more than a hundred years ago. The fast and erratic motion of small particles was first directly observed from a microscope by Robert Brown in 1827. This motion is general, and occurred with any particles as long as they are small enough. These phenomena were explained based on a kinetic-molecular model: the small particle was being pushed around by the collision of surrounding molecules in the environment. This idea was further put into quantitative terms in the early 1900s by Einstein and von Smolchowski. Later, Jean Perrin did the experiment to follow the movement of a nature colloid (gamboge) directly, recording their distance moved as a function of time. With the help of Einstein and von Smolchiwski's theory, they provided the first direct evidence of the existence of molecules and first estimated Avogadro's Number.

In a normal diffusion, a meso-scale object is diffused in a continuous hydrodynamic fluid in the absence of any external field. The driving force of this diffusion process is the gradient of chemical potential μi, because the substance will tend to migrate to equalize the values through the phase.

Therefore, for a one-dimensional diffusion, the diffusion driving force is the function of chemical potential (μ_i) and displacement of the particle x.

$$F_d = -d\mu_i/dx \qquad (6.1)$$

The diffusion force per molecule can be written as

$$f_d = -\frac{\left(\frac{kT}{c_i}\right)dc_i}{dx}, \qquad (6.2)$$

in which c_i is the concentration.

The opposing force to slow down the diffusion is the viscous force, which is proportional to the velocity of the particles, as described as

$$f_v = Bu \qquad (6.3)$$

where B is called the friction coefficient. This factor measures how strongly the surrounding fluid resist the motion of the particle, which is determined partly by viscosity η and particle shape. As the particle increase its speed to achieve this terminal speed, $f_d = f_v = Bu_d$. u_d is the terminal speed and is related the flux of material per unit area. In the mean time, the flux of materials is given by Fick's first law of diffusion

$$J_i = u_d c_i = -D\frac{dc}{dx} \qquad (6.4)$$

D is diffusion coefficient. Combined with equations (6.2) and (6.4), we can obtain

$$D = \frac{kT}{B} \qquad (6.5)$$

for spherical particle of radius r: $B = 6\pi\eta r$.

Experimentally, the diffusion of the particles exhibits a typical random walk. In order to measure the diffusion coefficient D, one can record the distance of one particle observed as a function of

time. Mean square displacement $\langle x^2 \rangle$ was applied to average the displacement of particle diffusion in diffusion time t, as the average displacement $\langle x \rangle = 0$. The root mean squared displacement $\langle x^2 \rangle^{1/2}$ can be described as follows:

$$\langle x^2 \rangle^{1/2} = \left[\frac{\int_{-\infty}^{\infty} x^2 c(x,t) dx}{\int_{-\infty}^{\infty} c(x,t) dx} \right]^{1/2} = \left[\frac{1}{c_0} \int_{-\infty}^{\infty} x^2 c(x,t) dx \right]^{1/2} \quad (6.6)$$

The mean squared displacement can be related to diffusion coefficient

$$\langle x^2 \rangle^{1/2} = (2Dt)^{1/2} \quad (6.7)$$

For diffusion in the 2D and 3D, the equation can be rewritten as

$$\langle r^2 \rangle^{\frac{1}{2}} = (q_i D t)^{\frac{1}{2}} \quad (6.8)$$

q_i is numerical constant which depends on dimensionality, which equals to 2, 4 and 6 for one, two and three dimenstions.

The central assumption in describing normal solute diffusion is that the solute diffuses in a continuous hydrodynamic flow. However, this assumption cannot be fulfilled in most cases when solute transportation occurs in a crowded environment, which contains many different solutes with a large distribution of sizes. In this case, not all the diffusion can be described by Einstein's equation for Brownian motion. Therefore, the non-Brownian motion behavior is usually described by the following semiempirical equations:

$$\langle r^2 \rangle = q_i D t^{\alpha} \quad (6.9)$$

If $\alpha < 1$, the diffusion of the system is called sub-diffusion. This phenomenon is common in particle diffusion in an entangled polymer environment. When $\alpha > 1$, the particle exhibits a super-

diffusion. This diffusion usually occurs in the presence of external forces. It has also been reported that the super-diffusion was observed in the self-propelled system.

It is important to notice that, on different time intervals, the system may exhibit different diffusion behavior. Even if a particle diffuses normally, it is also possible that the particle exhibits different diffusion in a shorter or longer characteristic time. For example, for the self-propelled system, at a short time interval, the system demonstrates a ballistic motion (super-diffusion), while at a long time interval, it comes back to the normal diffusion. For the particles diffused in a confined space, the particle first diffuses normally with a linear $\langle r^2 \rangle \sim \tau$ curve; after it encounters the boundary, $\langle r^2 \rangle$ will achieve a plateau and won't increase with time.

6.1.2 Diffusion in Polymer Solutions

The effect of molecular crowding on solute diffusion in solution, cellular aqueous compartments, and membranes, has attracted a lot of attention. [140-142] A biological medium usually contains a high total concentration of soluble macromolecules. More commonly, a medium may contain a variety of macromolecular species, none of which individually may be present at high concentrations, but which collectively occupy a substantial fraction of the total volume of the medium.[142] The biological medium is also likely to be structured at the molecular level by the presence of a network of extended structures, such as F-actin, micro tubules, intermediate filaments, and membranous boundaries. Molecular crowding has a significant effect on transport of the solute, which consequently leads to a great impact on the related biochemical reactions. A lot of efforts have been put forth to investigate the behavior of solute transport in a crowded environment, and to engineer the structure of the probes in order to achieve an efficient diffusion.

The diffusion of a probe in a crowded environment has been investigated in detail by a single-particle tracking method combined with a time-dependent correlation spectrum using various sizes of the small molecules. [140, 141] The diffusion of the solutes exhibits either a normal Brownian motion or anomalous diffusion, depending on the environment and the size of the probes. The study also revealed that crowding can slow down the diffusion of probes in aqueous-phase compartments and in membranes without leading to anomalous diffusion. Deviation from the Stokes-Einstein prediction for the diffusion coefficient might emerge when the size of the solutes are comparable to the size of other species in the environment.

Compared to biomolecular solutes, colloidal particles exhibit more structural simplicity , thereby reducing the complexity of their configuration change and interaction with the solvent, as occurs in the biomolecule's case.[143-145] As a good model system, micro-sized colloidal particles have been used to study the diffusion behavior in macromolecular environments, such as actin or micro-tubules. [143, 144]Asymmetric modified colloidal particles also allow for engineering their diffusion in a short time interval. For example, an artificial micro-scale swimmer that uses a chemical reaction catalyzed on its own surface to achieve autonomous propulsion has been developed experimentally. [146-152] Strings of colloidal particles connected by soft-matter linkages were reported to achieve a directional movement with the beating of the elastic filaments. [153]

The diffusion of the designed nanostructures, such as nanoparticles and nanoclusters, down to tens of nanometers has been rarely studied by a single-particle tracking method due to their fast diffusion speed and small sizes, which is beyond the resolution limits of the instrument. However, this fast diffusion can be slowed down in the solution with crowded polymer molecules. The effect on the diffusion properties of the nano-scale objects could be very interesting, since their

sizes are comparable to the solvent macromolecule. [154-156] Here, the diffusion of designed nano-objects in a crowded environment has been explored by the single-particle tracking method, in which the instrument tracks the moving trajectories of scattered light from the metallic gold nanoparticles. The question we try to address here is how the symmetry of the nano-object influences its diffusive behavior in a crowded environment.

6.2 Experimental Design

The diffusive motion of the object we studied here is the symmetric gold nanoparticles hard-core covered with symmetric/asymmetric DNA soft-matter shells (See Figure 6.1). In particular, three types of dimers with slightly different structural features were applied: a symmetric dimer (Figure 6.1a), fabricated by a step-wise surface-encoded method, is served as a symmetric control sample. This dimer is composed of two 10 nm particles with DNA shells which are linked by 3~6 strands of 30-base DNA linker strands connecting DNA shells on the particles by 15 complementary base-pairs on each end. The asymmetric dimer (as shown in Figure 6.1b) is a dimer with DNA tails grafted onto one of the particles. It is also fabricated by the surface-encoded method, in which the one of particles was grafted with 10 times the amount of 75 bases of single-stranded DNA "tail strand," containing 15 complementary bases on the DNA of the second layer particles and the other 60 bases of the overhanging part. A dimer sample with DNA tails on both particles is introduced as the second type of control sample (Figure 6.1c). The length and number of the tails on both ends is the same as the tails on the asymmetric dimer. The asymmetric property of the object is coming from the asymmetric soft-matter shells, other than the asymmetric metallic core. These three types of dimers were put in an environment of a

dense polymer solution. The system allows for a broad adjustment of design. The design has been shown in Figure 6.1D. For example, the structure of the nanoclusters can be adjusted by changing the number, length, and rigidity of tails. The diffusion environment can be varied by tuning the number of parameters, such as the molecular weight, types of the polymers and their corresponding concentrations. In a typical model system, different mass percentages of the polyethylene glycol (PEG) 35K water solution has been chosen as a diffusion environment. Diffusion properties of these three types of dimers were studied by dispersing them into various PEG35K solutions with various mass concentrations.

Figure 6.1. Schematic illustration of the studied systems: a) control dimer b) dimer with DNA tails grafted on one of the particles and c) dimer with DNA tails grafted on both particles. d) These three structures were dispersed in the various polymer solutions respectively, and their diffusion behavior was observed by particle-tracking and DLS.

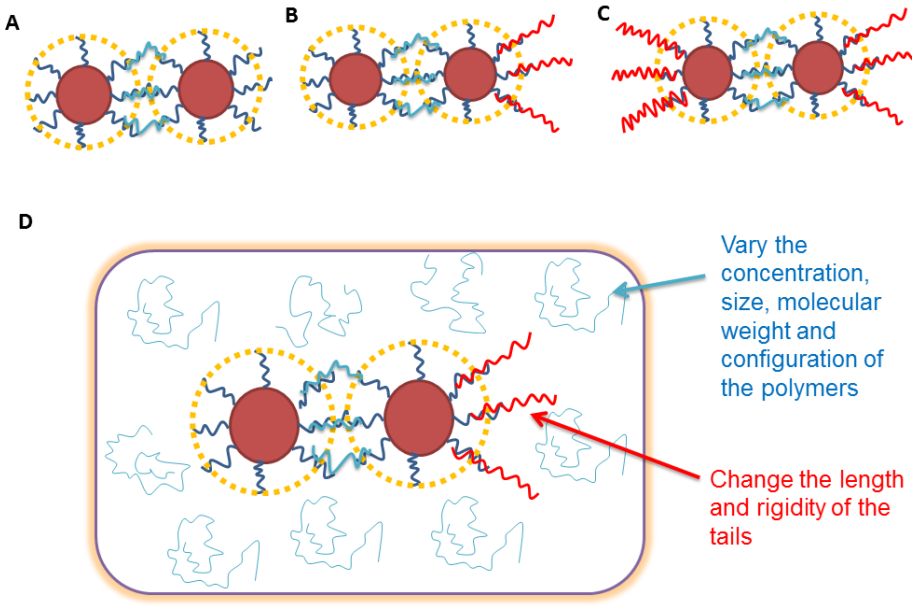

The diffusion of the nanoparticles in the viscous solution can be characterized by a particle-tracking method using Nanosight LM-10HS, the photos of which are shown in Figure 6.2A. Based on the conventional optical microscope, this instrument uses a laser light source to illuminate nano-scale particles within a 0.3 ml sample introduced to the viewing unit with a disposable syringe. Enhanced by a near-perfect black background, particles appear individually as point-scatterers moving under Brownian motion. Because gold nanoparticles scatter a lot of light, one can easily visualize the gold nanoparticle and their formed clusters from the microscope, even if they are small. The resolution of this microscope is half of the laser wavelength, which is approximately ×200~300nm. This is not high enough to visualize each single particle in the clusters, which is only about tens of nanometers. Therefore, each nanocluster can be tracked as a single bright spot, no matter how many particles are contained in the cluster.

The instruments record the projection of particle movement in a 2D plane by video. The Nanoparticle Tracking Analysis software automatically locates and follows the centre of each and every particle, and measures the average distance it moves per frame, which corresponds to 0.03 s. After tracking over hundreds of particles, all the trajectories will be extracted by the software (Figure 6.2B and C). The mean-square displacement and the displacement probability histogram of each clusters is calculated by the computer program we developed, described in the methods part (Figure 6.2D and E). The diffusion coefficient can be estimated by the equation $\langle r^2 \rangle = 4Dt$. The hydrodynamic radius of diffusing nano-object can be estimated by Einstein equation $r = \frac{kT}{6\pi D\eta}$.

One of the fundamental concerns of this diffusion study is if the system is ergodic or not. An ergodic diffusion means the time-average of a function along the trajectories exists almost everywhere, and is related to the space average. This can be checked by comparing the time-dependent MSD~τ curve at different time windows and different space. In the particular system we studied, the MSD~ τ curve is independent of the measured time window and space, which confirmed that the system is ergodic.

Figure 6.2 A) Photos of the instrument used in this study. B) A snapshot of 50 nm gold nanoparticle movement captured by microscope. C) Trajectories of each particle extracted by Nanoparticle Tracking software. D, E) MSD~τ curve based on Displacement Probility distributions obtained by analyzing all of the trajectories shown in image C. (The photos were obtained from company's website)

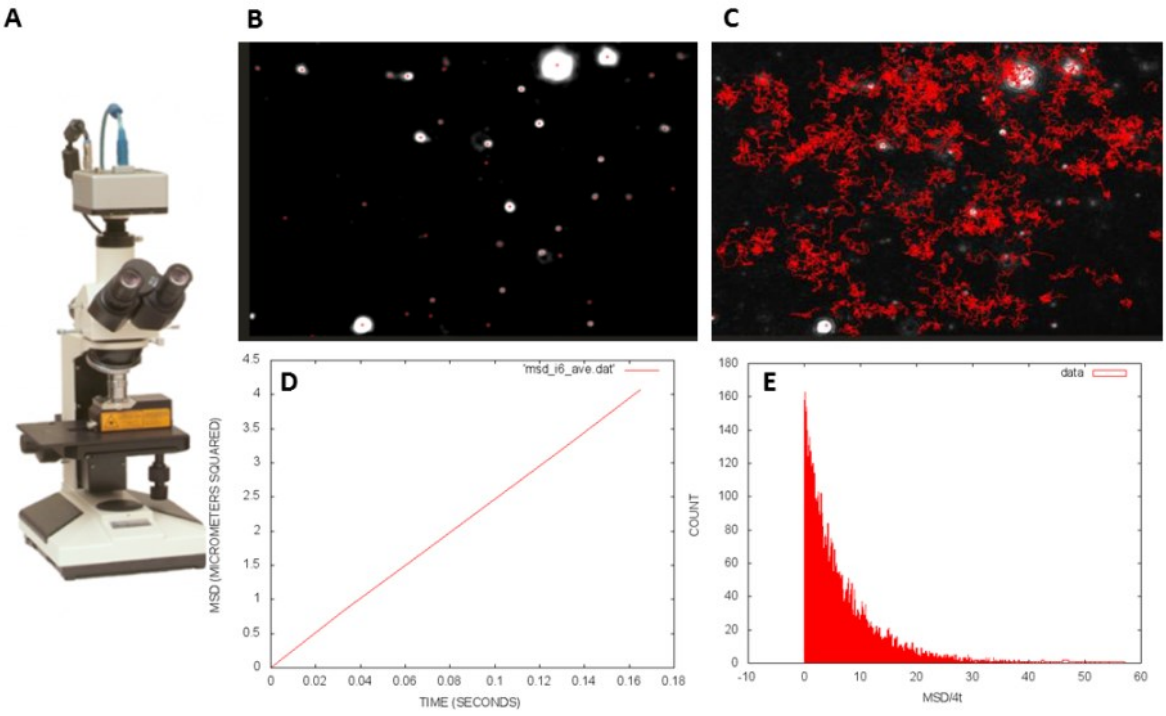

6.3 Experimental Results and Discussion

We first characterized the diffusion of the nanoclusters using a particle-tracking method by looking at thousands of trajectories from hundreds of clusters. The mean-squared displacement and the displacement probability distribution of the cluster diffusion were obtained through analyzing all of the trajectories without bias. As shown in Figure 6.3a, the representative trajectories for both asymmetric and symmetric dimers exhibit a typical random walk. In the same observation time interval (12s), the asymmetric dimer (shown in blue) diffused a significantly longer distance than it did for the symmetric control sample a (red).

Based on the statistical analysis of five hundred non-overlapping trajectories with the time interval over 1.6s , we obtained the mean squared displacement (MSD) as a function of time (Figure 6.3b). For both asymmetric and symmetric dimers, the MSD curve exhibits a linear dependence on the time interval (τ), which indicates normal Brownian motion. By looking at the correlation of their direction of motion using the approach represented in the methods part, we reveal that each particle is moving independently in a random direction (Table 6.1), therefore we exclude the possibility that the motion of the particle is drifting in a certain direction, which is typical in the presence of an external field. In order to further confirm that the faster movement of an asymmetric particle is not coming from any artificial effects coming associate with laser's local heating. We switched two lasers with similar power at different wavelengths (638nm and 533nm). The absorption of the Surface Plasmon Band to the gold nanoparticles increases about 7-fold when the wavelength of the laser switched from 638nm to 533nm. Correspondingly, the observed diffusion curves of MSD ~ τ slightly changed for both the asymmetric sample and symmetric control sample. However, the change is not significant and it is in the range of the error bar, which indicates that the laser's heating did not play an important role here.

Estimating the slope of those MSD curves allows one to get the diffusion coefficient. For example, in a two-dimension projection: Mean Squared Displacement $< \Delta r^2(t) >= 4D\tau$

The fitting yields the diffusion coefficient of the dimer control sample, **a,** equal to 0.37 $\mu m^2/s$. For the asymmetric dimer sample, the diffusion speed is two times as fast as it is for the symmetric control sample, with D = 0.75 $\mu m^2/s$.

Figure 6.3. Characterization of the typical diffusion in 9% mass percentage of PEG 35,000 : a)Two-dimensional projection of typical 12 s trajectories (with 0.03s between frames) of asymmetric (shown in blue) and symmetric dimer control sample a (shown in red). b) Linear plots of the mean squared displacement (MSD) as a function of τ for both asymmetric (blue) and symmetric (red) dimers, calculated from more than 500 non-overlapping trajectories. c) Displacement probability distribution with time interval τ =0.6s. d) Logarithmic plot of MSD of three different studied systems as shown below. The black dashed curve is the reference line, estimated by Brownian motion using the macro-viscosity of the solution obtained from viscosity measurements.

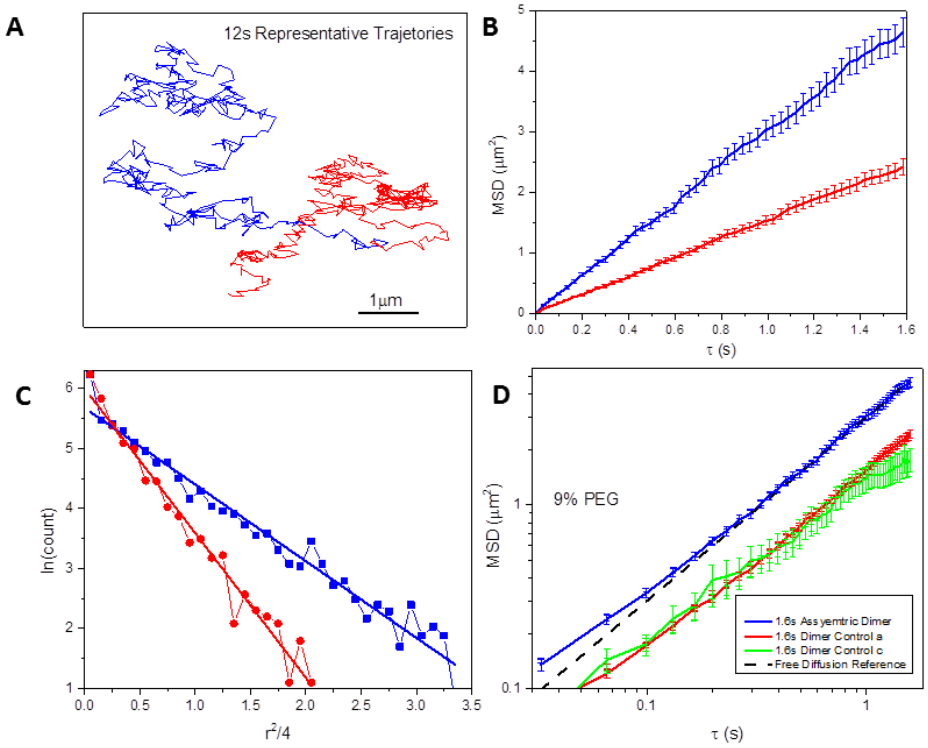

The corresponding displacement probability distribution is shown in Figure 6.3c, where $\Delta r^2(\tau)$ denotes the 2-dimensional projection of displacement at time τ. The ln(G(r,t)) shows a linear dependence on $\Delta r^2(\tau)$, which is consistent with a typical Gaussian decay expected from normal Brownian motion. The diffusion coefficient can also be estimated from fitting the decay slope of this histogram, which yields a D= 0.78 $\mu m^2/s$ for asymmetric dimers and D=0.41 $\mu m^2/s$ for the symmetric case. The result is consistent with what we obtained from the slope of MSD.

In order to confirm that the enhancement of the diffusion is indeed coming from the asymmetric soft matter shell rather than the squeezing effect from the soft-matter shell, we compared our result with the other type of the symmetric control sample **c**: a dimer with both ends grafted with DNA tails (as shown in green). In the logarithmic plot of MSD curve as shown in Figure 2d, for both symmetric designs, we obtained a similar diffusion coefficient of D=0.34 $\mu m^2/s$.

Tables 6.1. PEG mass concentration and their corresponding non-over lapping trajectories which count to the statistics at time interval τ=1.6s. $Cos^2\vartheta$-0.5 is the directionality factors which characterize the correlation of the moving directions for all of the trajectories. $Cos^2\vartheta$-0.5 =0 indicates that the moving directions of these trajectories are random.

PEG mass Concentration (%)	$Cos^2\vartheta$-0.5 (Control)	Statistics Number (Control)	$Cos^2\vartheta$-0.5 (Asymmetric)	Statistics Number (Asymmetric)
3	0.007	336	0.027	596
6	-0.028	468	0.007	300
7.5	0.003	256	0.0038	287
9	0.007	553	0.011	525
12	0.06	176	0.014	176

Moreover, we compared this result with the Brownian diffusion estimated the macro-viscosity of Spherical particle with the same hydrodynamic radius. Both two symmetric structures diffuse significantly slower than the reference curve. In contrast, the asymmetric structures almost diffused as fast as the reference curves.

We further explored the diffusion behavior of the asymmetric/symmetric dimer in various PEG mass concentrations. The diffusion behavior of the symmetric dimer and asymmetric dimer is very similar in water, with slightly different measured hydrodynamic diameters in DLS: 34 nm for symmetric dimer and 37 nm for asymmetric ones. When PEG35k's mass concentration reaches C*, which is around 3% , we see both asymmetric dimers and symmetric dimers diffused slower than the reference curve estimated from Brownian motion based on the macro-viscosity (Figure 6.4a). However, the asymmetric dimer moves slightly faster than the two symmetric samples with D =2.0 $\mu m^2/s$, compared with D=1.54 $\mu m^2/s$ and D=1.63 $\mu m^2/s$ for control dimers and dimers with two ends grafted with DNA, respectively.

Figure 6.4. MSD as a function of τ in various PEG 35K concentrations with the mass percentage equals to 3% (a) 7.5% (b) and 12%(c), the macro-viscosity of which changed to up 30 folds and (d) their diffusion enhancement factor, R, as a function of PEG mass percentage.

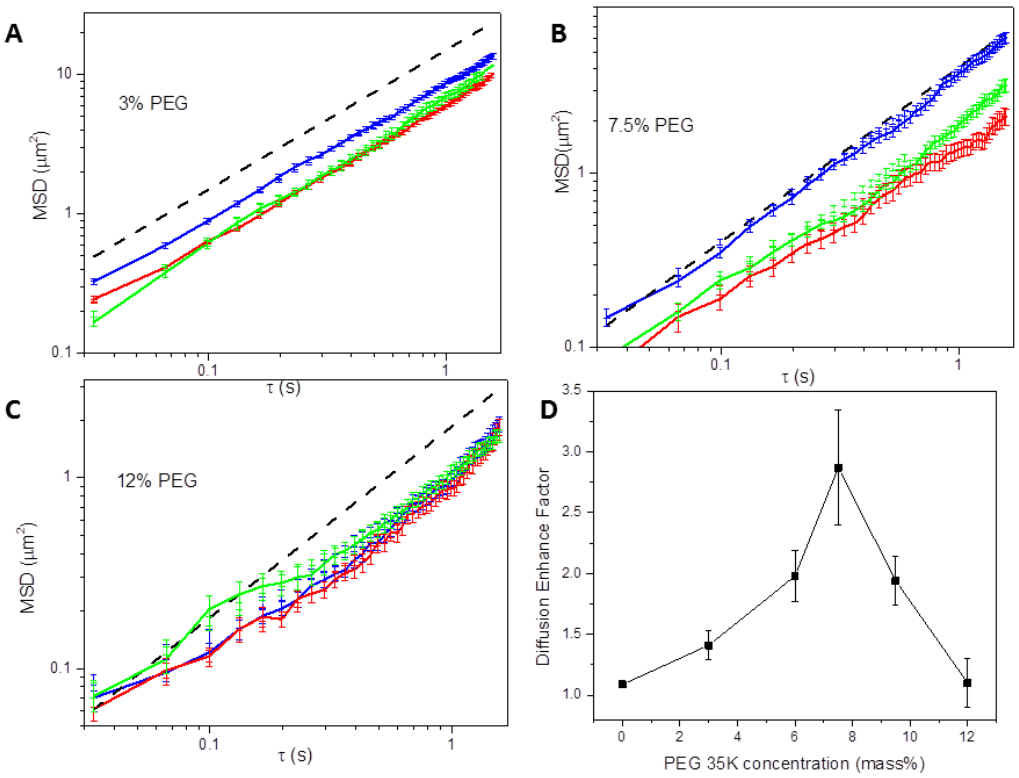

When the concentration of PEG 35K increased to 7.5%, (shown in Figure 6.4b), the difference between asymmetric dimers and symmetric dimers becomes more significant, with D= 0.95 $\mu m^2/s$ for the swimmer sample and D=0.40 $\mu m^2/s$ for the control sample. Similar with the case we observed in 9% PEG mass concentration, the asymmetric structure diffused as fast as the reference curve, while the control samples still moved slower than the reference curve. The deviation of the asymmetric dimers and symmetric dimers collapses at 12% PEG concentration, where both structures exhibit a slower diffusion than the reference curve. The diffusion in a time interval longer than 0.2s exhibits Brownian motion, with D=0.2 $\mu m^2/s$. However, we observe a deviation from the normal Brownian motion at the first 0.2s time interval, which can explained

by an artifact related to the comparatively slow diffusion to the space resolution of the particle tracking. The space resolution of particle tracking is half of the wavelength of emitted laser light, which is $267nm \times 267nm$. In a short time interval, if the diffusion of the particle is not fast enough to diffuse outside of this resolution square, the determination of the particle position will not be accurate and will yields a large error bar.

Table 6.2. Diffusion Coefficient of asymmetric dimer and the symmetric control dimers and their corresponding diffusion enhancement factor, R in various PEG concentration. The data was obtained from particle tracking at τ=1.6s.

PEG Mass Concentration (%)	*D*, Asymmetric Dimers ($\mu m^2/s$)	*D*, Symmetric Dimers ($\mu m^2/s$)	$R=D_{as}/D_s$
3	2.084	1.54	1.4
6	1.4175	0.7265	2.0
7.5	0.95	0.405	2.4
9	0.74	0.3725	2.1
12	0.2575	0.22	1.2

Displacement probability distribution with time interval τ =0.6s for all the PEG concentrations has been shown in Figure 6.5, with all the systems exhibiting a Gaussian function and yielding the same diffusion coefficients obtained as that obtained from MSD~τ functions.

Figure 6.3.d demonstrates the diffusion enhancement factor as a function of the PEG mass concentration. The details of the diffusion coefficient can be found in Table 6.2. The enhanced diffusion appears in a broad regime of PEG concentrations from 3% to 9%, which is 1 to 3 times that of the C*. The enhancement factor achieved its maximum at 7.5% PEG concentration. The error bar of this enhancement factor is estimated from the error bar of MSDs, as shown in Figure 6.2b. We also checked the enhancement factor in a shorter time window (0.6s), the result exhibiting a consistent enhancement factor, regardless of the length of the time interval (Figure 6.6).

Figure 6.5. Measured displacement probability distribution with time interval (τ) =0.6s at various PEG condition shows that the distribution of both symmetric (shown as red and green) and asymmetric (shown as blue) objects is Gaussian.

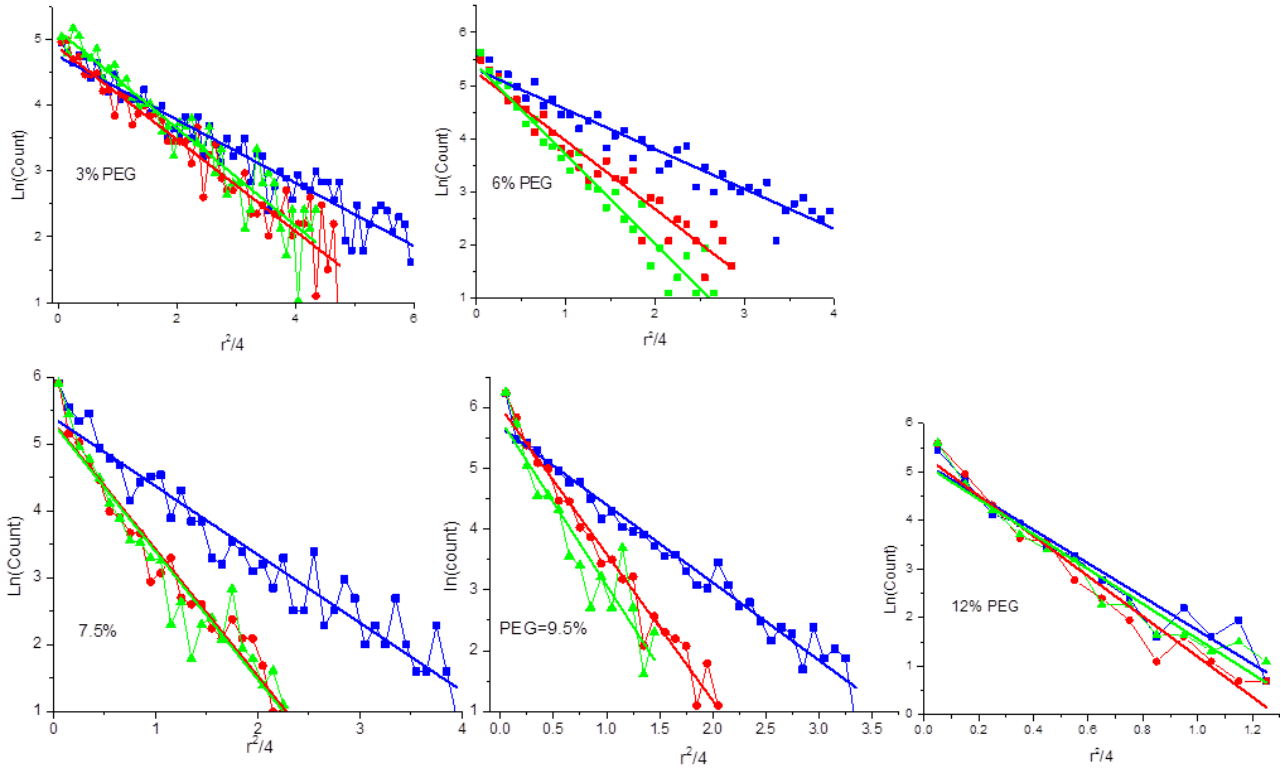

Figure 6.6. The diffusion enhancement factor as a function of time interval (τ) for various PEG concentrations as shown. The results indicate that the enhancement factor is independent of observation time interval.

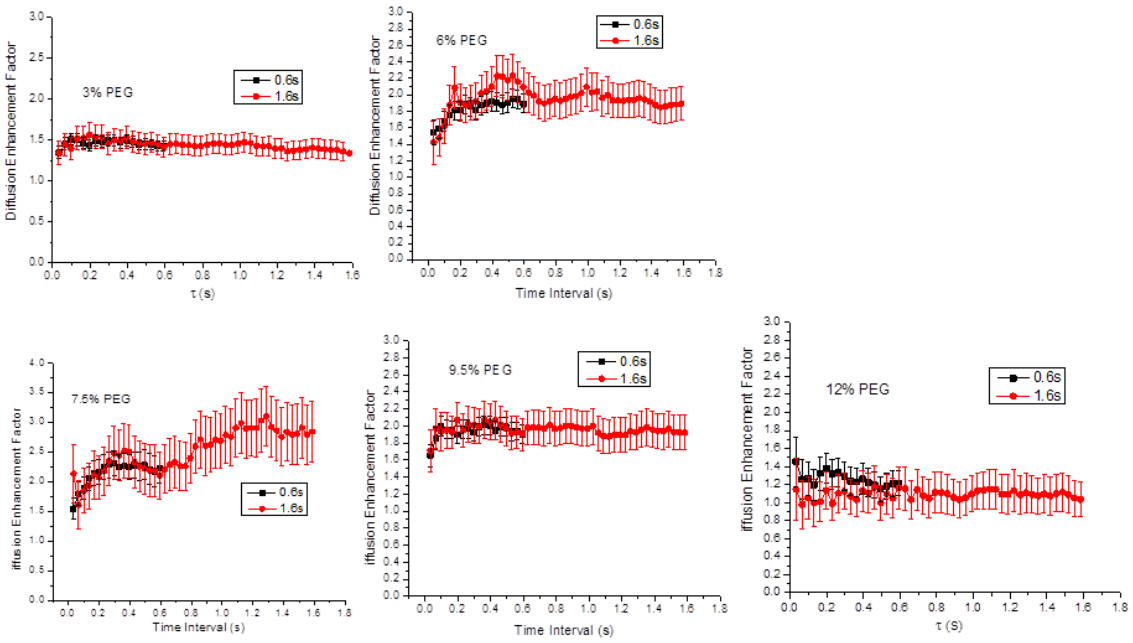

The difference of diffusion coefficients between asymmetric dimers and symmetric dimers has been further examined by Dynamic Light Scattering (as shown in table 6.3), which estimated the diffusion coefficient of the particles by a time-correlation function. DLS measures the diffusion effect in different time windows with a particle-tracking method .In particular, DLS measures the particle diffusion on a time scale less than 0.01s, while particle-tracking measures the diffusion for more than 0.03s. Therefore, DLS provides important supplementary information on the diffusion behavior in a smaller time window. The measured DLS data confirmed that both the particle-tracking method and dynamic light scattering gives comparable diffusion coefficients with an error bar less than ± 10%. [157]

Table 6.3. Comparison of diffusion coefficients for the symmetric dimer control sample and asymmetric dimer samples, obtained from Dynamic Light Scattering and Particle-Tracking method at various PEG concentrations.

PEG concentration	*D*, from DLS for symmetric control dimer ($\mu m^2/s$)	*D*, from particle tracking method for symmetric control dimer ($\mu m^2/s$)	*D*, from DLS for asymmetric dimer ($\mu m^2/s$)	*D*, from particle tracking method for asymmetric dimer ($\mu m^2/s$)
0%	12.84		11.79	
1.5%	6.71		8.7	
3%	1.28	1.54	3.24	2.0
6%	0.53	0.72	1.16	1.4
7.5%	0.48	0.40	0.90	0.95
9%	0.33	0.37	0.84	0.74
12%	0.20	0.22	0.33	0.25

To investigate if this phenomenon can be universally observed in various structures, we studied the diffusion behavior between asymmetric Janus particles and symmetric spherical particles. In the typical study, 50nm spherical particles with 30 bases DNA shells were applied as a control sample. The asymmetric particle is a 50nm Janus particle fabricated from the step-wised method with a tail of 180 bases pair length on one side of the particle surface. As shown in Figure 6.7a,

Janus particles exhibit faster diffusion compared with the control sample: 50nm gold particle with thin DNA shells with an enhanced diffusion factor of around 1.3.The lower diffusion enhancement factor of the Janus Particle compared with the asymmetric dimer might be due to the `anisotropic properties of dimers.

Figure 6.7. Similar behavior has been ob served for different geometries of the diffusion objects, and in various polymer solutions. a) MSD~τ for a 50nm Janus Particle with 180-base double stranded DNA and corresponding 50nm gold nanoparticle control at 9% PEG. b) Comparison of symmetric dimers (shown in red) and asymmetric dimer (shown in blue) in the 15% 32k Dextran.

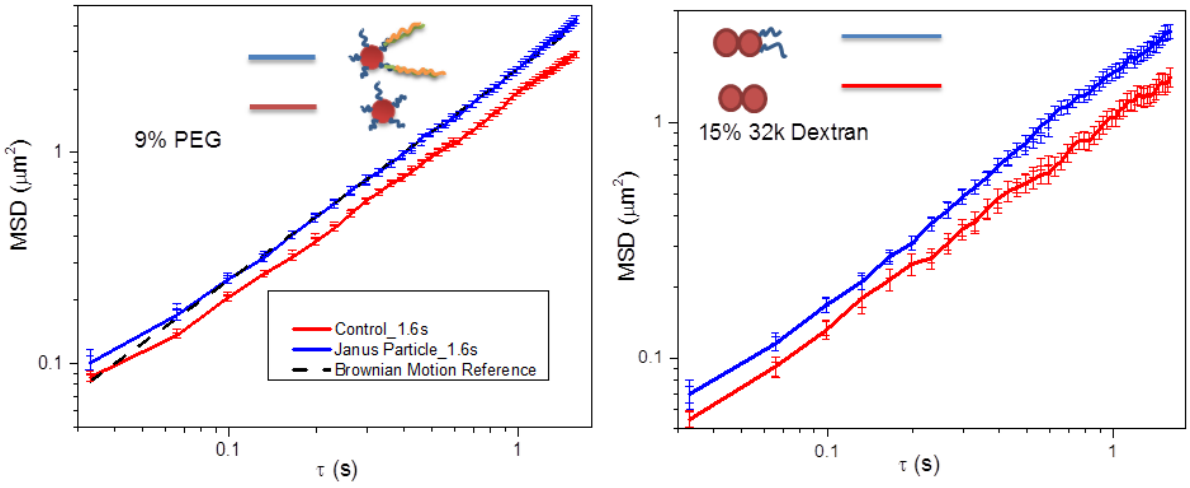

The same effect has been observed in other polymer solutions. As an example, Figure 6.7b demonstrates the MSD~τ curve for asymmetric and symmetric dimers in a 15% (mass percentage) Dextran solution with a molecular weight equal to 32k. Consistent with previous cases reported in PEG solutions, both objects exhibit a normal Brownian motion, with the diffusion enhancement factor about 1.5 for the asymmetric object. For Dextran **32K**, the maximum diffusion enhancement appears at 15% mass percentage. The details of the

experimental data for Dextran is shown in Figure 6.8, which presents the MSD~τ curve in the presence of various dextran concentrations, varied from 10~20%. We observed that at a Dextran concentration of 10%, the diffusion of the symmetric dimer is faster than it is for the asymmetric dimer, due to the smaller hydrodynamic radius. When the Dextran concentration was at 15%, a 1.5x diffusion enhancement was observed. When the Dextran concentration increased to 20%, the difference of asymmetric and symmetric dimers is much less significant and almost in the range of the error bars. Compared with the PEG system with a similar molecule weight, the maximum enhancement factor of Dextran is smaller, which might be due to the different molecular configurations.

Figure 6.8. (a,b,c) MSD~τ dependence for asymmetric dimers (shown in blue) and control dimers (shown in red) at various concentrations of Dextran 32K, as shown below. d) Diffusion enhancement factor as a function of Dextran percentage.

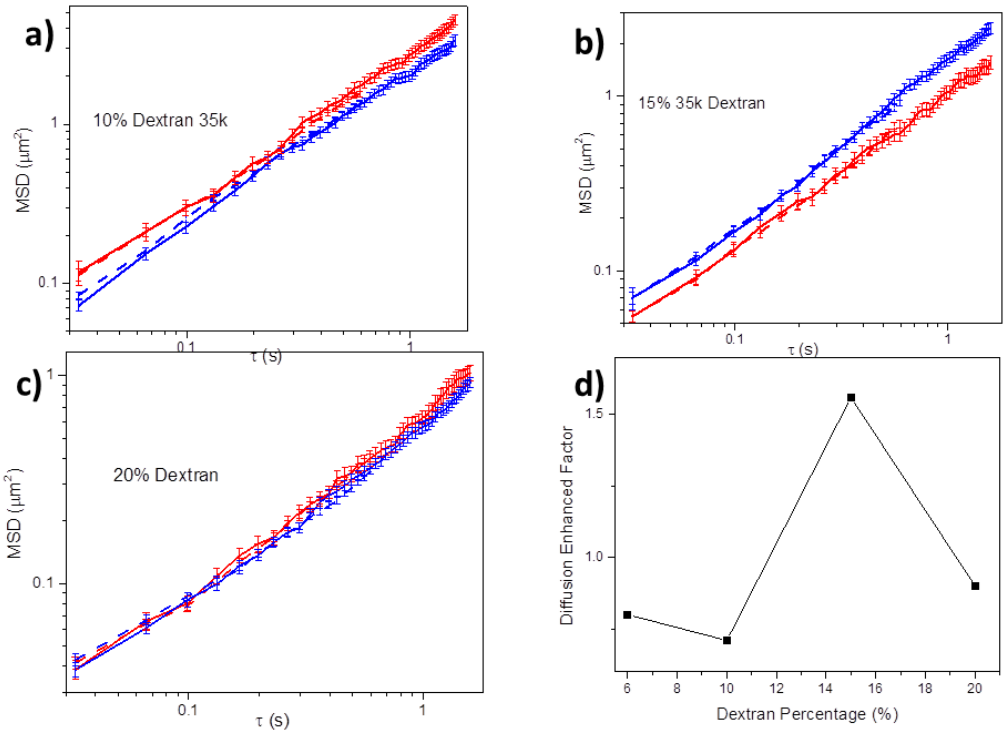

It is also interesting to notice that the diffusion enhancement also depends on the molecular weight . When PEG with a molecular weight equal to 8K was applied as the macromolecule in the environment, the diffusion enhancement effect has not been observed. (Figure6.9). The diffusion of the symmetric and asymmetric dimers is still slower than one would expect from macroscopic theory, as shown in the dashed curve.

Figure 6.9. MSD~τ dependence for asymmetric dimer (blue) and control dimers (red) at various concentration of PEG 8000, as shown below.

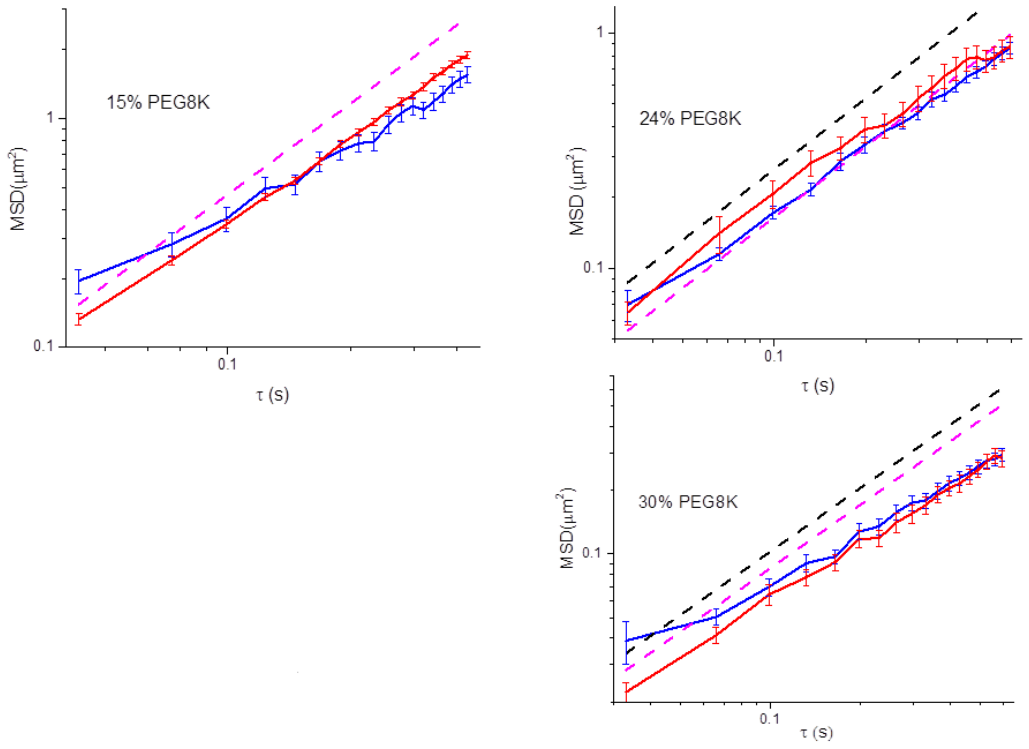

Enhanced diffusion of asymmetric object might appear an intuitive result. In particular, there are multiple examples of active microscopic swimmers whose self-propulsion in one direction, coupled with rotational diffusion may leads to much faster apparent diffusion. However, the system under investigation is in thermal equilibrium. Due to the second law of thermodynamics,

any swimmer-like preferential motion in one direction is impossible. Instead, we are dealing with regular thermal diffusion, which according to Einstein relationship is simply proportional to the particle mobility. Since symmetric addition of DNA tails to both sides of a dimer does not result in any significant change in the diffusion coefficient, we may conclude that translational mobility is not strongly affected by the tails. However, the asymmetric particles are different in that their symmetry allows for non-zero coupling between their translational and rotational mobility. The strength of this coupling depends on the microscopic physics, and cannot be easily evaluated. However, if such coupling exists, it means that the observed translational mobility is higher than in symmetric case, which in turn leads to enhanced diffusion. The details of theoretical study to review the mechanism of observed phenomenon are now under investigation with Professor Erik Luijten (Northwestern University) and Dr. Alexei Tkachenko (BNL).

6.4 Conclusion

Gold nanoparticle dimers with symmetric/asymmetric soft-matter shells diffusing in various concentrations of PEG solutions has been applied as a model system to study the diffusion behavior of nano-objects in a crowded environment. In certain concentration regions (1~3 times of amount of C*), the asymmetric nano-objects diffuse significantly faster than the corresponding symmetric structure, with the diffusion enhancement factor as high as 3-fold. This phenomenon can be observed in various macromolecular environments with different structures of nano-sized diffusion objects. This studied system provides important insight into the diffusion mechanism of biophysical systems, and opens up a lot of possibilities for delivery applications of small molecules.

6.5 Methods

Fabrication of symmetric dimer control samples and asymmetric dimer samples The symmetric control dimer was fabricated by a step-wise method based on a previously reported method from literature. [71] The asymmetric dimer sample was also fabricated following the same step-wise method used for the symmetric control dimers. However, at the last step on the surface, a 75-base DNA was added upon the second layer particle, with 15 bases complementary to the DNA grafted on the surface of the particle. Then, the asymmetric dimer sample was released from the surface using the same fuel strand that was used for the control dimer case. The symmetric sample with DNA tails grafted on two ends was obtained by adding the other DNA strands which are complementary to the DNA on the other particles to the asymmetric samples. We also obtained this type of the symmetric dimer by adding more linker strands to the dimer control samples **a**. The experimental result for both types of the structure is similar.

Particle tracking measurement Particle tracking measurements were performed on the Nanosight LM10-HS, with laser wavelength at 533nm and 638nm. In this measurement, the fabricated particles were first dispersed into various solutions containing different mass concentrations of macromolecules (such as 35000 PEG or Dextrans). The typical measurement temperature is 22 ^{o}C. The concentration of the measurement sample is on the order of 0.001nM, in order to achieve the best measurement resolution. The particle movement was tracked by the scattering of the particles. The video of the particles moving was captured, and the moving trajectory of the diffusion-object was extracted by the NTA2.0 software. Their Mean Squared Displacement (MSD) and the corresponding histogram were calculated by a statistics method, which will be described in detail below.

Dynamic light scattering measurement DLS measurements were performed on a Malvern Zetasizer ZS instrument. The instrument is equipped with a 633 nm laser source and a backscattering detector at 173°. Measurements were recorded at 22°C. The samples were dispersed in various concentrations of the macromolecule solutions and measured.

Data analysis The particle-tracking instrument provides 2-dimensional trajectory data. In computing the average mean-square displacement for a given system, trajectories with fewer than M steps were ignored. This was done because these short trajectories correspond to the artifact related to focus in different 3D surface. . Each trajectory with greater than M steps was divided into non-overlapping sub-trajectories, each with N steps. The sub-trajectories were then averaged over all particles to produce a single curve. Error bars were computed in the standard way by dividing the variance in the mean-square displacement at each time by the square root of the total number of sub-trajectories. Histograms were computed from the mean-square displacement of the sub-trajectories at a given time value using a bin size of 0.1 μm^2. We computed $\langle\cos^2\vartheta\rangle$ - 0.5, where $cos^2\vartheta = \left\{\frac{\overrightarrow{r_{n+1}}\bullet\overrightarrow{r_n}}{\left|\overrightarrow{r_{n+1}}\right|\left|\overrightarrow{r_n}\right|}\right\}^2$, for each system and found values approximately equal to zero (see Table 6.1), indicating that successive steps are independent of each other. This is expected from the single-particle self-diffusion time of a 5 nm particle of $\tau = \frac{3\pi ma^3}{2kT}$approx 140 ns . This time is roughly five orders of magnitude smaller than the time resolution of the particle-tracking instrument of 0.033 seconds.

Chapter 7

Conclusions and Future Work

The work presented in this thesis mainly focuses on the systems of finite-sized nanoclusters. The simplest finite-size nanocluster, a dimer composed of two nanoparticles connected by DNA linkages, was applied as the model system.

In chapter 2 and chapter 3, I demonstrated two methods to fabricate dimers in a high-throughput way. The internal structures of the assembled dimers were studied in detail by scattering experiments and molecular simulation:

In the first method, dimer assembly can be achieved by the step-wise surface-encoding method. The interparticle distance of the dimers is dependent on the number, length, and flexibility of the DNA linkers. When multiple linkers were applied, the interparticle distance is constrained by the shortest linkage between particles (Chapter 2), which yield to a deviation from the worm-like chain model.

In the second method, dimers were obtained by simply mixing two nanoparticles grafted with evenly-distributed ssDNA linkers. As discussed in Chapter 3, when a longer linker was applied, we observed a significantly shortened interparticle distance of the dimers, corresponding to the DNA shell thickness between two nanoparticles. The result indicates a self-limited structure of the dimers, in which the linkers connect to the opposing hemispheres of the particles and inhibit the growth of the dimers.

More complicated small clusters with different structures, such as trimers or tetrahedral structures, can be fabricated by using these two strategies. However, two challenges for these strategies are the following: First, for both methods, the yield of nanoclusters will decrease to 60% when the target structure contains more than three particles. Second, when more than one particle is attached to the core particle, it is difficult to control the orientation of each particle in the cluster. The first challenge can be solved by separating nanoclusters with different numbers of particles using a recognizable surface, as demonstrated in Chapter 4. The second challenge can be potentially solved by using rigid DNA scaffolds as linkers to connect various DNA-functionalized particles.

In Chapter 4, I demonstrated our attempts to use dimers for further assembly. We began with the recognition behavior of various geometries of the nano-objects to the DNA-functionalized surface. We found that the interaction process can be tuned by the DNA density on the recognizable surface and by the salt concentration. More importantly, kinetics and thermodynamics of this recognizing process is determined by the geometry of the nanoclusters: Dimers with the small "cross-section" exhibit significantly slower interaction kinetics to the surface, compared with Janus particles and spherical controlled particles. When dimers were applied as a building block to do further assembly in bulk solution, this geometry effect leads to an inefficient reaction.

DNA-functionalized nano-structures can be applied as biosensors to detect RNA/DNA and related small molecules. Compared with other DNA sensors based on aggregation of DNA-functionalized nanoparticles, the simplicity of dimers allows for efficient target detection in minutes, with the detection sensitivity down to the single-molecule level. Chapter 5 demonstrated a nucleic acid detector based on the disassembly of dimer nanoclusters. The

nucleic acid sensor allows detecting target DNA in the single-molecule level with a single base-pair mismatch, even in the presence of 100 times the amount of interference strand. More future work will be attributed to *in vivo* detection and developing more mature detecting platforms to detect multiple targets on a single-molecule level.

Finally, in chapter 6, I explored the diffusion properties of nanoclusters in polymer solutions. I observed a significant enhancement of the diffusion for an asymmetric structure, dimer with DNA tails grafted on one side, compared with the other two symmetric dimer nano-constructs (dimers without tails, and dimers with tails grafted on both ends). The enhancement can be universally observed for various shapes of the diffusion-objects and different polymer solutions. The finding provides an important insight to the diffusion mechanism of biophysical systems and opens up various possibilities for delivery applications of small molecules. More efforts will be attributed to study their diffusion mechanism. The investigation of more complicated structures is also currently in progress.

REFERENCES

1. Whitesides, G.M. and B. Grzybowski, *Self-assembly at all scales.* Science, 2002. **295**(5564): p. 2418-2421.
2. Lal, S., S. Link, and N.J. Halas, *Nano-optics from sensing to waveguiding.* Nature Photonics, 2007. **1**(11): p. 641-648.
3. Stadler, A., et al., *DNA-incorporating nanomaterials in biotechnological applications.* Nanomedicine, 2010. **5**(2): p. 319-334.
4. Moghimi, S.M., A.C. Hunter, and J.C. Murray, *Nanomedicine: current status and future prospects.* Faseb Journal, 2005. **19**(3): p. 311-330.
5. Grzelczak, M., et al., *Directed Self-Assembly of Nanoparticles.* Acs Nano, 2010. **4**(7): p. 3591-3605.
6. Gang, O. and Y.G. Zhang, *Shaping Phases by Phasing Shapes.* Acs Nano, 2011. **5**(11): p. 8459-8465.
7. Torquato, S., T.M. Truskett, and P.G. Debenedetti, *Is random close packing of spheres well defined?* Physical Review Letters, 2000. **84**(10): p. 2064-2067.
8. Eldridge, M.D., P.A. Madden, and D. Frenkel, *Entropy-Driven Formation of a Superlattice in a Hard-Sphere Binary Mixture.* Nature, 1993. **365**(6441): p. 35-37.
9. Damasceno, P.F., M. Engel, and S.C. Glotzer, *Predictive Self-Assembly of Polyhedra into Complex Structures.* Science, 2012. **337**(6093): p. 453-457.
10. Dong, A.G., et al., *Binary nanocrystal superlattice membranes self-assembled at the liquid-air interface.* Nature, 2010. **466**(7305): p. 474-477.
11. Shevchenko, E.V., et al., *Structural diversity in binary nanoparticle superlattices.* Nature, 2006. **439**(7072): p. 55-59.
12. Talapin, D.V., *LEGO materials.* Acs Nano, 2008. **2**(6): p. 1097-1100.
13. McDonald, J.-P.H.a.I.R., *Theory of Simple Liquids*. 1986: 2nd Edition,

Academic Press.

14. Egelstaff, P.A., *An Introduction to the Liquid State*. 1992: 2nd Edition, Clarendon

Press, Oxford,.

15. Phalakornkul, J.K., et al., *Structure and short-time dynamics of polydisperse charge-stabilized suspensions.* Physical Review E, 1996. **54**(1): p. 661-675.
16. Seeman, N.C. and N.R. Kallenbach, *Optimal-Design of Immobile and Semi-Mobile Nucleic-Acid Junctions.* Biophysical Journal, 1982. **37**(2): p. A93-A93.
17. Seeman, N.C., *DNA in a material world.* Nature, 2003. **421**(6921): p. 427-431.
18. Chen, J.H. and N.C. Seeman, *Synthesis from DNA of a Molecule with the Connectivity of a Cube.* Nature, 1991. **350**(6319): p. 631-633.
19. Zhang, Y.W. and N.C. Seeman, *Construction of a DNA-Truncated Octahedron.* Journal of the American Chemical Society, 1994. **116**(5): p. 1661-1669.
20. Goodman, R.P., et al., *Rapid chiral assembly of rigid DNA building blocks for molecular nanofabrication.* Science, 2005. **310**(5754): p. 1661-1665.
21. Shih, W.M., J.D. Quispe, and G.F. Joyce, *A 1.7-kilobase single-stranded DNA that folds into a nanoscale octahedron.* Nature, 2004. **427**(6975): p. 618-621.
22. McLaughlin, C.K., G.D. Hamblin, and H.F. Sleiman, *Supramolecular DNA assembly.* Chemical Society Reviews, 2011. **40**(12): p. 5647-5656.
23. He, Y., et al., *Hierarchical self-assembly of DNA into symmetric supramolecular polyhedra.* Nature, 2008. **452**(7184): p. 198-U41.

24. Winfree, E., *Algorithmic self-assembly of DNA: Theoretical motivations and 2D assembly experiments.* Journal of Biomolecular Structure & Dynamics, 2000: p. 263-270.
25. Rothemund, P.W.K., *Folding DNA to create nanoscale shapes and patterns.* Nature, 2006. **440**(7082): p. 297-302.
26. Han, D.R., et al., *DNA Gridiron Nanostructures Based on Four-Arm Junctions.* Science, 2013. **339**(6126): p. 1412-1415.
27. Feldkamp, U. and C.M. Niemeyer, *Rational design of DNA nanoarchitectures.* Angewandte Chemie-International Edition, 2006. **45**(12): p. 1856-1876.
28. Yang, X.P., et al., *Torsional control of double-stranded DNA branch migration.* Biopolymers, 1998. **45**(1): p. 69-83.
29. Fahlman, R.P., et al., *Duplex pinching: A structural switch suitable for contractile DNA nanoconstructions.* Nano Letters, 2003. **3**(8): p. 1073-1078.
30. Liu, D.S. and S. Balasubramanian, *A proton-fuelled DNA nanomachine.* Angewandte Chemie-International Edition, 2003. **42**(46): p. 5734-5736.
31. Yurke, B., et al., *A DNA-fuelled molecular machine made of DNA.* Nature, 2000. **406**(6796): p. 605-608.
32. Mirkin, C.A., et al., *A DNA-based method for rationally assembling nanoparticles into macroscopic materials.* Nature, 1996. **382**(6592): p. 607-609.
33. Alivisatos, A.P., et al., *Organization of 'nanocrystal molecules' using DNA.* Nature, 1996. **382**(6592): p. 609-611.
34. Zanchet, D., et al., *Electrophoretic isolation of discrete Au nanocrystal/DNA conjugates.* Nano Letters, 2001. **1**(1): p. 32-35.
35. Zanchet, D., et al., *Electrophoretic and structural studies of DNA-directed Au nanoparticle groupings.* Journal of Physical Chemistry B, 2002. **106**(45): p. 11758-11763.
36. Zheng, J.W., et al., *Metallic nanoparticles used to estimate the structural integrity of DNA motifs.* Biophysical Journal, 2008. **95**(7): p. 3340-3348.
37. Jin, R.C., et al., *What controls the melting properties of DNA-linked gold nanoparticle assemblies?* Journal of the American Chemical Society, 2003. **125**(6): p. 1643-1654.
38. Hill, H.D., et al., *The Role Radius of Curvature Plays in Thiolated Oligonucleotide Loading on Gold Nanoparticles.* Acs Nano, 2009. **3**(2): p. 418-424.
39. Medintz, I.L., et al., *Quantum dot bioconjugates for imaging, labelling and sensing.* Nature Materials, 2005. **4**(6): p. 435-446.
40. Algar, W.R., M. Massey, and U.J. Krull, *The application of quantum dots, gold nanoparticles and molecular switches to optical nucleic-acid diagnostics.* Trac-Trends in Analytical Chemistry, 2009. **28**(3): p. 292-306.
41. Di Michele, L. and E. Eiser, *Developments in understanding and controlling self assembly of DNA-functionalized colloids.* Physical Chemistry Chemical Physics, 2013. **15**(9): p. 3115-3129.
42. Licata, N.A. and A.V. Tkachenko, *Statistical mechanics of DNA-mediated colloidal aggregation.* Physical Review E, 2006. **74**(4).
43. Knorowski, C. and A. Travesset, *Dynamics of DNA-programmable nanoparticle crystallization: gelation, nucleation and topological defects.* Soft Matter, 2012. **8**(48): p. 12053-12059.
44. Hsu, C.W., F. Sciortino, and F.W. Starr, *Theoretical Description of a DNA-Linked Nanoparticle Self-Assembly.* Physical Review Letters, 2010. **105**(5).
45. Padovan-Merhar, O., F.V. Lara, and F.W. Starr, *Stability of DNA-linked nanoparticle crystals: Effect of number of strands, core size, and rigidity of strand attachment.* Journal of Chemical Physics, 2011. **134**(24).
46. Angioletti-Uberti, S., B.M. Mognetti, and D. Frenkel, *Re-entrant melting as a design principle for DNA-coated colloids.* Nature Materials, 2012. **11**(6): p. 518-522.

47. Knorowski, C., S. Burleigh, and A. Travesset, *Dynamics and Statics of DNA-Programmable Nanoparticle Self-Assembly and Crystallization.* Physical Review Letters, 2011. **106**(21).
48. Mladek, B.M., et al., *Quantitative Prediction of the Phase Diagram of DNA-Functionalized Nanosized Colloids.* Physical Review Letters, 2012. **108**(26).
49. Tkachenko, A.V., *Morphological diversity of DNA-colloidal self-assembly.* Physical Review Letters, 2002. **89**(14).
50. Maye, M.M., et al., *DNA-Regulated micro- and nanoparticle assembly.* Small, 2007. **3**(10): p. 1678-1682.
51. Nykypanchuk, D., et al., *DNA-guided crystallization of colloidal nanoparticles.* Nature, 2008. **451**(7178): p. 549-552.
52. Nykypanchuk, D., et al., *DNA-based approach for interparticle interaction control.* Langmuir, 2007. **23**(11): p. 6305-6314.
53. Hill, H.D., et al., *Controlling the lattice parameters of gold nanoparticle FCC crystals with duplex DNA linkers.* Nano Letters, 2008. **8**(8): p. 2341-2344.
54. Park, S.Y., et al., *DNA-programmable nanoparticle crystallization.* Nature, 2008. **451**(7178): p. 553-556.
55. Xiong, H.M., D. van der Lelie, and O. Gang, *Phase Behavior of Nanoparticles Assembled by DNA Linkers.* Physical Review Letters, 2009. **102**(1).
56. Xiong, H.M., D. van der Lelie, and O. Gang, *DNA linker-mediated crystallization of nanocolloids.* Journal of the American Chemical Society, 2008. **130**(8): p. 2442-2443.
57. Chi, C., et al., *Internal Structure of Nanoparticle Dimers Linked by DNA.* Acs Nano, 2012. **6**(8): p. 6793-6802.
58. Macfarlane, R.J., et al., *Assembly and organization processes in DNA-directed colloidal crystallization.* Proceedings of the National Academy of Sciences of the United States of America, 2009. **106**(26): p. 10493-10498.
59. Macfarlane, R.J., et al., *Establishing the Design Rules for DNA-Mediated Colloidal Crystallization.* Angewandte Chemie-International Edition, 2010. **49**(27): p. 4589-4592.
60. Macfarlane, R.J., et al., *Nanoparticle Superlattice Engineering with DNA.* Science, 2011. **334**(6053): p. 204-208.
61. Jones, M.R., et al., *DNA-nanoparticle superlattices formed from anisotropic building blocks.* Nature Materials, 2010. **9**(11): p. 913-917.
62. Fu, A.H., et al., *Discrete nanostructures of quantum dots/Au with DNA.* Journal of the American Chemical Society, 2004. **126**(35): p. 10832-10833.
63. Maye, M.M., O. Gang, and M. Cotlet, *Photoluminescence enhancement in CdSe/ZnS-DNA linked-Au nanoparticle heterodimers probed by single molecule spectroscopy.* Chemical Communications, 2010. **46**(33): p. 6111-6113.
64. Fan, J.A., et al., *DNA-Enabled Self-Assembly of Plasmonic Nanoclusters.* Nano Letters, 2011. **11**(11): p. 4859-4864.
65. Yan, W.J., et al., *Self-Assembly of Chiral Nanoparticle Pyramids with Strong R/S Optical Activity.* Journal of the American Chemical Society, 2012. **134**(36): p. 15114-15121.
66. Lan, X., et al., *Bifacial DNA Origami-Directed Discrete, Three-Dimensional, Anisotropic Plasmonic Nanoarchitectures with Tailored Optical Chirality.* Journal of the American Chemical Society, 2013. **135**(31): p. 11441-11444.
67. Wang, R.S., C. Nuckolls, and S.J. Wind, *Assembly of Heterogeneous Functional Nanomaterials on DNA Origami Scaffolds.* Angewandte Chemie-International Edition, 2012. **51**(45): p. 11325-11327.
68. Wang, Y.F., et al., *Colloids with valence and specific directional bonding.* Nature, 2012. **491**(7422): p. 51-U61.

69. Halverson, J.D. and A.V. Tkachenko, *DNA-programmed mesoscopic architecture.* Physical Review E, 2013. **87**(6).
70. Suzuki, K., K. Hosokawa, and M. Maeda, *Controlling the Number and Positions of Oligonucleotides on Gold Nanoparticle Surfaces.* Journal of the American Chemical Society, 2009. **131**(22): p. 7518-+.
71. Maye, M.M., et al., *Stepwise surface encoding for high-throughput assembly of nanoclusters.* Nature Materials, 2009. **8**(5): p. 388-391.
72. Roe, R.-J., *Methods of X-ray and Neutron Scattering in Polymer Science*. Topics IN POLYMER SCIENCE, ed. J. E.MARK. 2000, New York: OXFORD UNIVERSITY PRESS.
73. Pecora, B.J.B.a.R., *Dynamic Light Scattering*. 2000: Dover publications.
74. Geerts, N. and E. Eiser, *Flying colloidal carpets.* Soft Matter, 2010. **6**: p. 664-669.
75. Geerts, N., T. Schmatko, and E. Eiser, *Clustering versus Percolation in the Assembly of Colloids Coated with Long DNA.* Langmuir, 2008. **24**: p. 5118-5123.
76. Geerts, N. and E. Eiser, *DNA-functionalized colloids: Physical properties and applications.* Soft Matter, 2010. **6**: p. 4647-4660.
77. Seeman, N.C., *DNA in a material world.* Nature, 2003. **421**: p. 427-431.
78. Niemeyer, C.M., *Self-assembled nanostructures based on DNA: towards the development of nanobiotechnology.* Current Opinion in Chemical Biology, 2000. **4**: p. 609-618.
79. Condon, A., *Designed DNA molecules: principles and applications.* Nat. Rev. Genet., 2006(7): p. 565-575.
80. Maye, M.M., et al., *A simple method for kinetic control of DNA-induced nanoparticle assembly.* Journal of the American Chemical Society, 2006. **128**(43): p. 14020-14021.
81. Park, S.Y., et al., *DNA-programmable nanoparticle crystallization* Nature, 2008. **451**: p. 553-556.
82. Hurst, S.J., A.K.R. Lytton-Jean, and C.A. Mirkin, *Maximizing DNA loading on a range of gold nanoparticle sizes.* Analytical Chemistry, 2006. **78**(24): p. 8313-8318.
83. Xiong, H.M., D. van der Lelie, and O. Gang, *Phase Behavior of Nanoparticles Assembled by DNA Linkers.* Physical Review Letters, 2009. **102**(1): p. 015504.
84. Hsu, C.W., et al., *Hierarchies of networked phases induced by multiple liquid-liquid critical points.* Proceedings of the National Academy of Sciences of the United States of America, 2008. **105**(37): p. 13711-13715.
85. Dai, W., et al., *Valency Dependence of Polymorphism and Polyamorphism in DNA-Functionalized Nanoparticles.* Langmuir, 2009. **26**: p. 3601-3608.
86. Dai, W., S.K. Kumar, and F.W. Starr, *Universal two-step crystallization of DNA-functionalized nanoparticles.* Soft Matter, 2010. **6**(24): p. 6130-6135.
87. Vargas-Lara, F. and F.W. Starr, *Stability of DNA-linked nanoparticle crystals I: Effect of linker sequence and length.* Soft Matter, 2011. **7**(5): p. 2085-2093.
88. Sonnichsen, C., et al., *A molecular ruler based on plasmon coupling of single gold and silver nanoparticles.* Nature Biotechnology, 2005. **23**(6): p. 741-745.
89. Maye, M.M., et al., *Switching binary states of nanoparticle superlattices and dimer clusters by DNA strands.* Nature Nanotechnology, 2010. **5**(2): p. 116-120.
90. Xiong, H.M., M.Y. Sfeir, and O. Gang, *Assembly, Structure and Optical Response of Three-Dimensional Dynamically Tunable Multicomponent Superlattices.* Nano Letters, 2010. **10**(11): p. 4456-4462.
91. Crocker, J., *Nanomaterials: Golden handshake.* Nature, 2008. **451**: p. 528-529.
92. Ritchie, R.O., M.J. Buehler, and P. Hansma, *Plasticity and toughness in bone.* Physics Today, 2009. **62**(6): p. 41-47.
93. Milner, S.T., *Polymer Brushes.* Science, 1991. **251**(4996): p. 905-914.

94. Bustamante, C., Z. Bryant, and S.B. Smith, *Ten years of tension: single-molecule DNA mechanics.* Nature, 2003. **421**(6921): p. 423-427.
95. Murphy, M.C., et al., *Probing single-stranded DNA conformational flexibility using fluorescence spectroscopy.* Biophysical Journal, 2004. **86**(4): p. 2530-2537.
96. Rivetti, C., C. Walker, and C. Bustamante, *Polymer chain statistics and conformational analysis of DNA molecules with bends or sections of different flexibility.* Journal of Molecular Biology, 1998. **280**(1): p. 41-59.
97. Mastroianni, A.J., et al., *Probing the Conformational Distributions of Subpersistence Length DNA.* Biophysical Journal, 2009. **97**(5): p. 1408-1417.
98. Mathew-Fenn, R.S., R. Das, and P.A.B. Harbury, *Remeasuring the double helix.* Science, 2008. **322**(5900): p. 446-449.
99. Chi, C., et al., *Sensing Nucleic Acids with Dimer Nanoclusters.* Advanced Functional Materials, 2011. **21**(6): p. 1051-1057.
100. Largo, J., F.W. Starr, and F. Sciortino, *Self-assembling DNA dendrimers: A numerical study.* Langmuir, 2007. **23**(11): p. 5896-5905.
101. Starr, F.W. and F. Sciortino, *Model for assembly and gelation of four-armed DNA dendrimers.* Journal of Physics-Condensed Matter, 2006. **18**(26): p. L347-L353.
102. Kaya, H., *Scattering from cylinders with globular end-caps.* Journal of Applied Crystallography, 2004. **37**: p. 223-230.
103. Bustamante, C., et al., *Single-molecule studies of DNA mechanics.* Current Opinion in Structural Biology, 2000. **10**(3): p. 279-285.
104. Doi, M. and S. Edwards, *The Theory of Polymer Dynamics*. 1998: Oxford University Press, USA 408.
105. Smith, B.D., et al., *Assembly of DNA-Functionalized Gold Nanoparticles with Gaps and Overhangs in Linker DNA.* Journal of Physical Chemistry C, 2011. **115**(16): p. 7851-7857.
106. Walther, A. and A.H.E. Muller, *Janus Particles: Synthesis, Self-Assembly, Physical Properties, and Applications.* Chemical Reviews, 2013. **113**(7): p. 5194-5261.
107. Ye, S.R. and R.L. Carroll, *Design and Fabrication of Bimetallic Colloidal "Janus" Particles.* Acs Applied Materials & Interfaces, 2010. **2**(3): p. 616-620.
108. Jiang, S., et al., *Solvent-free synthesis of janus colloidal particles.* Langmuir, 2008. **24**(18): p. 10073-10077.
109. Jiang, S. and S. Granick, *Controlling the geometry (Janus balance) of amphiphilic colloidal particles.* Langmuir, 2008. **24**(6): p. 2438-2445.
110. Sciortino, F., A. Giacometti, and G. Pastore, *Phase Diagram of Janus Particles.* Physical Review Letters, 2009. **103**(23).
111. Swiston, A.J., et al., *Surface Functionalization of Living Cells with Multilayer Patches.* Nano Letters, 2008. **8**(12): p. 4446-4453.
112. Sardar, R., T.B. Heap, and J.S. Shumaker-Parry, *Versatile solid phase synthesis of gold nanoparticle dimers using an asymmetric functionalization approach.* Journal of the American Chemical Society, 2007. **129**(17): p. 5356-+.
113. Xu, X.Y., et al., *Asymmetric functionalization of gold nanoparticles with oligonucleotides.* Journal of the American Chemical Society, 2006. **128**(29): p. 9286-9287.
114. Li, Z.W., et al., *Model, self-assembly structures, and phase diagram of soft Janus particles.* Soft Matter, 2012. **8**(25): p. 6693-6697.
115. Chen, Q., et al., *Janus and Multiblock Colloidal Particles.* Langmuir, 2012. **28**(38): p. 13555-13561.
116. Chen, Q., S.C. Bae, and S. Granick, *Directed self-assembly of a colloidal kagome lattice.* Nature, 2011. **469**(7330): p. 381-384.

117. Liu, K., N.N. Zhao, and E. Kumacheva, *Self-assembly of inorganic nanorods.* Chemical Society Reviews, 2011. **40**(2): p. 656-671.
118. Lu, F., et al., *Discrete Nanocubes as Plasmonic Reporters of Molecular Chirality.* Nano Letters, 2013. **13**(7): p. 3145-3151.
119. Levicky, R. and A. Horgan, *Physicochemical perspectives on DNA microarray and biosensor technologies.* Trends in Biotechnology, 2005. **23**(3): p. 143-149.
120. Wang, H., et al., *Nucleic Acid Conjugated Nanomaterials for Enhanced Molecular Recognition.* Acs Nano, 2009. **3**(9): p. 2451-2460.
121. Liu, J.W. and Y. Lu, *Accelerated color change of gold nanoparticles assembled by DNAzymes for simple and fast colorimetric Pb2+ detection.* Journal of the American Chemical Society, 2004. **126**(39): p. 12298-12305.
122. Wang, Z.D. and Y. Lu, *Functional DNA directed assembly of nanomaterials for biosensing.* Journal of Materials Chemistry, 2009. **19**(13): p. 1788-1798.
123. Rosi, N.L. and C.A. Mirkin, *Nanostructures in biodiagnostics.* Chemical Reviews, 2005. **105**(4): p. 1547-1562.
124. He, L., et al., *Colloidal Au-enhanced surface plasmon resonance for ultrasensitive detection of DNA hybridization.* Journal of the American Chemical Society, 2000. **122**(38): p. 9071-9077.
125. Qian, X.M., X. Zhou, and S.M. Nie, *Surface-Enhanced Raman Nanoparticle Beacons Based on Bioconjugated Gold Nanocrystals and Long Range Plasmonic Coupling.* Journal of the American Chemical Society, 2008. **130**(45): p. 14934-+.
126. Elghanian, R., et al., *Selective colorimetric detection of polynucleotides based on the distance-dependent optical properties of gold nanoparticles.* Science, 1997. **277**(5329): p. 1078-1081.
127. Xu, X.Y., M.S. Han, and C.A. Mirkin, *A gold-nanoparticle-based real-time colorimetric screening method for endonuclease activity and inhibition.* Angewandte Chemie-International Edition, 2007. **46**(19): p. 3468-3470.
128. Liu, J.W. and Y. Lu, *Smart nanomaterials responsive to multiple chemical stimuli with controllable cooperativity.* Advanced Materials, 2006. **18**(13): p. 1667-+.
129. Il Park, J., et al., *Microfluidic Synthesis of Polymer and Inorganic Particulate Materials.* Annual Review of Materials Research, Vol 40, 2010. **40**: p. 415-443.
130. Zhang, C.Y., et al., *Single-quantum-dot-based DNA nanosensor.* Nature Materials, 2005. **4**(11): p. 826-831.
131. Chen, J.I.L., Y. Chen, and D.S. Ginger, *Plasmonic Nanoparticle Dimers for Optical Sensing of DNA in Complex Media.* Journal of the American Chemical Society, 2010. **132**(28): p. 9600-9601.
132. Lim, D.K., et al., *Nanogap-engineerable Raman-active nanodumbbells for single-molecule detection.* Nature Materials, 2010. **9**(1): p. 60-67.
133. Dai, Q., et al., *A One-Step Highly Sensitive Method for DNA Detection Using Dynamic Light Scattering.* Journal of the American Chemical Society, 2008. **130**(26): p. 8138.
134. Taton, T.A., C.A. Mirkin, and R.L. Letsinger, *Scanometric DNA array detection with nanoparticle probes.* Science, 2000. **289**(5485): p. 1757-1760.
135. Tawa, K. and W. Knoll, *Mismatching base-pair dependence of the kinetics of DNA-DNA hybridization studied by surface plasmon fluorescence spectroscopy.* Nucleic Acids Research, 2004. **32**(8): p. 2372-2377.
136. Lee, H.J., A.W. Wark, and R.M. Corn, *Creating advanced multifunctional biosensors with surface enzymatic transformations.* Langmuir, 2006. **22**(12): p. 5241-5250.
137. Reynaldo, L.P., et al., *The kinetics of oligonucleotide replacements.* Journal of Molecular Biology, 2000. **297**(2): p. 511-520.

138. Xu, Z.H., et al., *Shell Thickness Dependent Photoinduced Hole Transfer in Hybrid Conjugated Polymer/Quantum Dot Nanocomposites: From Ensemble to Single Hybrid Level.* Acs Nano, 2012. **6**(6): p. 4984-4992.
139. Xu, Z.H. and M. Cotlet, *Photoluminenscence Blinking Dynamics of Colloidal Quantum Dots in the Presence of Controlled External Electron Traps.* Small, 2012. **8**(2): p. 253-258.
140. Dix, J.A. and A.S. Verkman, *Crowding effects on diffusion in solutions and cells.* Annual Review of Biophysics, 2008. **37**: p. 247-263.
141. Verkman, A.S., *Solute and macromolecule diffusion in cellular aqueous compartments.* Trends in Biochemical Sciences, 2002. **27**(1): p. 27-33.
142. Zimmerman, S.B. and A.P. Minton, *Macromolecular Crowding - Biochemical, Biophysical, and Physiological Consequences.* Annual Review of Biophysics and Biomolecular Structure, 1993. **22**: p. 27-65.
143. Wang, B., et al., *Anomalous yet Brownian.* Proceedings of the National Academy of Sciences of the United States of America, 2009. **106**(36): p. 15160-15164.
144. Wang, B., et al., *When Brownian diffusion is not Gaussian.* Nature Materials, 2012. **11**(6): p. 481-485.
145. Wong, I.Y., et al., *Anomalous diffusion probes microstructure dynamics of entangled F-actin networks.* Physical Review Letters, 2004. **92**(17).
146. Ebbens, S.J. and J.R. Howse, *In pursuit of propulsion at the nanoscale.* Soft Matter, 2010. **6**(4): p. 726-738.
147. Golestanian, R., *Anomalous Diffusion of Symmetric and Asymmetric Active Colloids.* Physical Review Letters, 2009. **102**(18).
148. Golestanian, R., T.B. Liverpool, and A. Ajdari, *Designing phoretic micro- and nano-swimmers.* New Journal of Physics, 2007. **9**.
149. Howse, J.R., et al., *Self-motile colloidal particles: From directed propulsion to random walk.* Physical Review Letters, 2007. **99**(4).
150. Cordova-Figueroa, U.M. and J.F. Brady, *Osmotic propulsion: The osmotic motor.* Physical Review Letters, 2008. **100**(15).
151. Tao, Y.G. and R. Kapral, *Swimming upstream: self-propelled nanodimer motors in a flow.* Soft Matter, 2010. **6**(4): p. 756-761.
152. Rings, D., et al., *Hot Brownian Motion.* Physical Review Letters, 2010. **105**(9).
153. Dreyfus, R., et al., *Microscopic artificial swimmers.* Nature, 2005. **437**(7060): p. 862-865.
154. Holyst, R., et al., *Nanoscale transport of energy and mass flux during evaporation of liquid droplets into inert gas: computer simulations and experiments.* Soft Matter, 2013. **9**(32): p. 7766-7774.
155. Hou, S., et al., *Influence of nano-viscosity and depletion interactions on cleavage of DNA by enzymes in glycerol and poly(ethylene glycol) solutions: qualitative analysis.* Soft Matter, 2011. **7**(7): p. 3092-3099.
156. Ziebacz, N., et al., *Crossover regime for the diffusion of nanoparticles in polyethylene glycol solutions: influence of the depletion layer.* Soft Matter, 2011. **7**(16): p. 7181-7186.
157. Kalwarczyk, T., et al., *Comparative Analysis of Viscosity of Complex Liquids and Cytoplasm of Mammalian Cells at the Nanoscale.* Nano Letters, 2011. **11**(5): p. 2157-2163.